U.PORTO
FEUP FACULDADE DE ENGENHARIA
UNIVERSIDADE DO PORTO

M 2023

FATIGUE PERFORMANCE OF A S690QL STEEL WELDED CONNECTION UNDER ROTATING BENDING FATIGUE TEST

MÁRIO JORGE MOUTINHO MONTEIRO
MASTER'S DEGREE DISSERTATION IN MATERIALS ENGINEERING PRESENTED TO THE FACULTY OF ENGINEERING OF THE UNIVERSITY OF PORTO

MANUEL FERNANDO GONÇALVES VIEIRA
SUPERVISOR FEUP
FULL PROFESSOR AT THE DEPARTMENT OF METALLURGICAL AND MATERIALS ENGINEERING

PAULO JORGE SOEIMA CARMONA MENDES
CO-SUPERVISOR FEUP
PHD CANDIDATE AT THE DEPARTMENT OF CIVIL ENGINEERING

Abstract

High-strength steels, such as S690QL, are increasingly used in structural applications due to their improved mechanical properties. These materials are often used in offshore applications, where welded joints are critical. However, the characterization of welded joints in these materials is challenging due to changes in microstructure and mechanical properties. This study investigated the fatigue behaviour of welded joints made of S690QL using rotational bending fatigue testing. Specimens were taken from the weld material (WM), heat-affected zone (HAZ), and base material (BM) of two plates with different thicknesses (30 mm and 60 mm). Vickers hardness testing, microstructural composition analysis, and fractographic evaluation were also conducted.

The results showed that the HAZ is made up of several subzones with different morphologies and grain sizes. The grain size decreases with increasing distance from the fusion line. The hardness profiles showed that the heat input from subsequent welding steps can temper the microstructure of the first steps, leading to a decrease in hardness values. The HAZ had the highest hardness values, followed by the weld material and the base material.

The fatigue results showed that the weld material had the greatest fatigue resistance, followed by the base material and the HAZ in all regimes. The HAZ had a shorter fatigue life when compared with the base material due to its heterogeneous nature. The fatigue resistance of the 60 mm thickness plate was significantly lower than the 30 mm plate for the HAZ and base material in terms of cycles.

The fractographic analysis showed that the fatigue cracks initiated at the material´s surface and propagated in a stable manner. The overload area was composed of dimples and shallow voids, indicating a ductile fracture.

The results of this study provide valuable insights into the fatigue behaviour of welded S690QL joints. The findings suggest that the HAZ is the most critical region in terms of fatigue resistance and that the fatigue life of the welded joint can be significantly improved by optimizing the welding procedures.

Keywords

Fatigue; High-cycle Fatigue; Low-cycle Fatigue; Metal Active Gas; S690QL; S-N Curve; Welded Joint; Vickers hardness.

Resumo

Os aços de alta resistência, como o S690QL, são cada vez mais utilizados em aplicações estruturais devido às suas excelentes propriedades mecânicas. Estes materiais são frequentemente utilizados em aplicações offshore, onde as juntas soldadas são críticas. No entanto, a caraterização de juntas soldadas nestes materiais é um desafio devido a alterações na microestrutura e nas propriedades mecânicas. Este estudo baseou-se no comportamento à fadiga de juntas soldadas feitas de aço S690QL pelo processo MAG, utilizando ensaios de fadiga por flexão rotativa como meio experimental. As amostras foram retiradas do cordão de soldadura (CS), da zona termicamente afetada (ZTA) e do material de base (MB) de duas placas com espessuras diferentes (30 mm e 60 mm). Foram também realizados ensaios de dureza Vickers, análise da composição química e microestrutural e análise da superfície de fratura.

Os resultados mostraram que a ZTA é composta por várias subzonas com diferentes morfologias e tamanhos de grão. O tamanho do grão diminui com o aumento da distância à linha de fusão. Os perfis de dureza mostraram que a entrega térmica dos passos de soldadura subsequentes têm a capacidade de revenir a microestrutura dos primeiros passos, levando a uma diminuição dos valores de dureza. A ZTA apresentou os valores de dureza mais elevados, seguida do cordão de soldadura e do material de base.

Os resultados de fadiga mostraram que o cordão de soldadura apresenta a maior resistência à fadiga, seguido do material de base e da ZTA em todos os regimes. A ZTA teve uma vida à fadiga mais curta quando comparada com o material de base devido à sua natureza heterogénea. A resistência à fadiga da placa M60 foi significativamente mais baixa do que a da placa de 30 mm para a ZTA e o material de base em termos de número de ciclos de fadiga.

A análise fractográfica mostrou que as fissuras de fadiga se iniciaram na superfície do material e se propagaram de forma estável. A área de fratura catastrófica era composta por dimples e vazios pouco profundos, indicando que o material descreveu um tipo de fratura dúctil.

Os resultados deste estudo fornecem informações valiosas sobre o comportamento à fadiga de juntas soldadas de S690QL. Os resultados sugerem que a ZTA é a região mais crítica em termos de resistência à fadiga e que a vida à fadiga da junta soldada pode ser significativamente melhorada através da otimização dos procedimentos de soldadura.

Palavras-chave

Dureza Vickers; Curva S-N; Fadiga; Fadiga em Altos Ciclos; Fadiga em Baixos Ciclos; Junta Soldada; Metal Active Gas; S690QL.

Acknowledgements

Gostaria de agradecer em primeiro lugar ao meu orientador, Professor Manuel Vieira, por não só me ter ensinado todos os conceitos fundamentais desta engenharia ao longo do meu percurso académico, como também pela orientação, dedicação e suporte para o desenvolvimento deste trabalho. O mesmo é refletido ao leque de professores e colaboradores do nosso departamento que me permitiram crescer como pessoa e profissional.

Ao Eng.º Paulo Mendes, por me ter acompanhado desde o início, acreditar nas minhas capacidades e por exigir sempre o melhor de mim. Por todas as discussões profissionais e académicas, mas também de Fórmula 1 e futebol, apesar de saber quem levou a melhor. Pelo companheirismo e tudo o resto, um obrigado não chega Paulo.

Uma palavra de apreço à empresa Martifer Group por investirem na inovação e apoiarem o desenvolvimento académico. Por proporcionarem a elaboração deste projeto: Aços de Alta Resistência na Metalomecânica 4.0, através do Fundo Europeu de Desenvolvimento Regional e do COMPETE 2020. Um agradecimento também a toda a equipa envolvida neste projeto, em especial ao Eng.º Rui Silva, com quem tive a oportunidade de trabalhar e partilhar conhecimentos.

Um profundo obrigado à minha família, Mãe e Pai, por serem um modelo a seguir todos os dias da minha vida e por me proporcionarem e ensinarem o foco, ganas e vontade necessários para alcançar todos os meus objetivos. À minha irmã, Inês, um obrigado por dar vida e hiperatividade a esta família, mas também por ser a minha melhor amiga. Ao Bernardo, por ser o meu big brother no meio de muita confusão. À minha querida Avó Lila, por todas as velas que acendeu e nunca deixou apagar.

À Mariana, por ter feito parte de mais uma etapa e pelo permanente incentivo, preocupação e amor que me proporcinaram suporte.

Um agradecimento, do fundo do coração, aos grandes amigos que levo daqui por todos os momentos, com e sem cerveja na mão. Um obrigado, sem vocês a faculdade não teria o mesmo significado. Não poderiam faltar os meus amigos de Esposende, que me viram a entrar como um menino e a sair como meio engenheiro (jokes on you). Um obrigado àqueles que me abriram os olhos ao mundo e que fazem parte da história de um livro que ainda vamos escrever.

Um obrigado.

Cofinanciado por:

COMPETE 2020 PORTUGAL 2020 UNIÃO EUROPEIA Fundo Europeu de Desenvolvimento Regional

Contents

Abstract i

Resumo ii

Acknowledgements iii

1 Introduction 1

1.1 Motivation of the MSc Thesis 1

1.2 Organization and Objectives 2

1.3 Martifer Group 3

2 Literature Review 4

2.1 Overview of High-Strength Low-Alloy Steel and its Properties 4

2.2 Fatigue Behaviour of Steels 5

2.2.1 Fatigue crack initiation 5

2.2.2 Fracture mechanics 6

2.2.3 Fatigue statistical planning and analysis of data 9

2.3 Welding Techniques - Electric Arc Welding 11

2.3.1 Gas Metal Arc Welding 12

2.3.2 Shielding gases 13

2.3.3 Transfer modes 14

2.4 HSLA Steels Weldability 14

3 Methodology 16

3.1 Materials 16

3.2 Experimental Procedure 18

3.2.1 Rotating bending fatigue test 18

3.2.2 Hardness test 22
3.2.3 Optical and scanning electron microscopy 23

4 Results and Discussion **24**
4.1 Optical microscopy analysis 24
4.2 SEM/EDS analysis 28
4.3 Hardness test analysis 30
4.3.1 High force Vickers hardness test 30
4.3.2 Low force Vickers hardness test 35
4.4 Rotating bending fatigue results 37
4.4.1 S690QL M30 welded plate 37
4.4.2 S690QL M60 welded plate 40
4.5 Fractographic analysis 45

5 Conclusions **51**

6 Future Works **53**

Appendixes **60**

A M30 Technical Plan **60**

B M60 Technical Plan **61**
B.1 M60 Technical Plan - Section C 61
B.2 M60 Technical Plan - Section D 62
B.3 M60 Technical Plan - Section E 63

C Rotating bending fatigue results for M30 plate **64**
C.1 M30 - Section A fatigue results 64
C.2 M30 - Section B fatigue results 65

D Rotating bending fatigue results for M60 plate **66**

D.1 M60 - Section C fatigue results 66

D.2 M60 - Section D fatigue results 67

D.3 M60 - Section E fatigue results 67

E Compounds' Stability - Ellingham Diagram **68**

List of Figures

1 Main framework for the MSc thesis. 2

2 Martifer Group's logo 3

3 Various stages of the fatigue life and pertinent variables 5

4 Crack nucleation as a result of cyclic slip 6

5 a) Fatigue crack propagation cross-section; b) Grain boundary acting as a threshold of crack growth 7

6 da/dN-ΔK curve diagram describing crack propagation in three different regions 8

7 S-N curve graphical representation 9

8 Scheme of the most common welding processes. 11

9 Work principle of GMAW process. 12

10 Characteristic Volt-Ampere curve. 13

11 S690QL longitudinal and transversal sections of a) M30 and b) M60 plates. . . . 18

12 Geometry and dimensions of the fatigue test specimens, in millimeters. 18

13 a) System´s schematic representation; b) Principle of rotating bending test. . . 19

14 Dimensions to carry on in the fatigue test. 20

15 Numerical analysis model for the 3-E-A specimen. 21

16 Geometry of the evaluated samples: a) M30 plate with root steps; b) M30 plate fully welded; c) M60 plate with root steps; d) M60 plate fully welded. 22

17 Overview of the microstructure highlighting the three different regions. 24

18 Columnar growth of WM grains in the fusion zone. 24

19 Microstructure of a MAG welded joint of S690QL steel with its characteristics areas: a) base material; b-e) heat-affected zone with respectively grain coarsening. 25

20 CCT diagram for S690QL steel 25

21 HAZ close to the fusion zone. 26

22 Intermediate HAZ. 26

23 HAZ farther of the FZ. 26
24 Base material. 26
25 Microstructure of the weld material at 50x magnification. 27
26 Microstructure of the weld material at 100x magnification. 27
27 Chemical profile of transition between base and weld material. 28
28 Vickers hardness profile for M30 plate with root steps. 30
29 Vickers hardness profile for M30 plate fully welded. 31
30 Vickers hardness profile for M60 plate with root steps. 32
31 Vickers hardness profile for M60 plate fully welded. 32
32 Affiliation B comparison between the two procedures for the M30 plate. 33
33 Affiliation B comparison between the two procedures for the M60 plate. 34
34 Schematic representation of welding process HAZ regions of an HSLA steel. . . 35
35 Hardness distribution across each HAZ sub-zone. 36
36 S-N curves of S690QL steel base material for sections A and B of the M30 plate. 37
37 S-N curves of S690QL steel welded joint for section A of the M30 plate. 38
38 S-N curves of S690QL steel welded joint for section B of the M30 plate. 39
39 S-N curves of the S690QL steel welded joint for section C of the M60 plate. . . 40
40 S-N curves of the M60 welded joint for sections C, D, and E from all zones. . . 41
41 S-N curves of M30 and M60 S690QL steel welded joint for all sections. 42
42 Stress distribution for (a) tensile and (b) rotating bending fatigue test. 43
43 Specimens' fracture surface analysis by SEM: a) base material; b) heat-affected zone; c) weld material; d) close-up of crack nucleation site of a). 45
44 Fracture surface analysis of WM specimens with a) single and b) multiple crack initiation sites. 46
45 Fracture surface analysis a) WM specimen b) initial propagation fracture surface c) striations d) region immediately prior to the overloaded area. 47

46 Dimples EDS analysis and corresponding inclusions' spectrum for a,b) weld material; c) base material; and d,e,f) heat-affected zone. 48

47 Dimples size and distribution in a) base material and b) weld material. 50

48 Technical plan of Section A and B for the 30 mm thickness plate. 60

49 Technical plan of Section C for the 60 mm thickness plate. 61

50 Technical plan of Section D for the 60 mm thickness plate. 62

51 Technical plan of Section E for the 60 mm thickness plate. 63

52 Compounds' stability according to the Ellingham Diagram. 68

List of Tables

1 Chemical composition of the base and filler material used in the welded joint. 16
2 Process parameters and technical planning. 17
3 Mechanical properties of the base and filler material used in the welding process. 17
4 Dimensions for the 3-E-A specimen. 21
5 Chemical composition of each zone by EDS analysis. 29
6 Variation between the M30 and the M60 plate specimens of the fatigue test. . . 44
7 Chemical composition of the inclusions using EDS analysis. 49
8 Rotating bending fatigue results for M30 section A. 64
9 Rotating bending fatigue results for M30 section B. 65
10 Rotating bending fatigue results for M60 section C. 66
11 Rotating bending fatigue results for M60 section D. 67
12 Rotating bending fatigue results for M60 section E. 67

List of Abbreviations

BM - Base Material

CCT Diagram - Continuous Cooling Transformation Diagram

CEV - Carbon Equivalent Value

CTWD - Contact Tip to Work Distance

CV - Constant Voltage

DCEN - Direct-Current Electrode Negative

DCEP - Direct-Current Electrode Positive

EDS - Energy-Dispersive X-ray Spectroscopy

GMAW - Gas Metal Arc Welding

HAZ - Heat-affected Zone

HCF - High-cycle Fatigue

HSLA - High-Strength Low-Alloy Steel

HSS - High-Strength Steel

LCF - Low-cycle Fatigue

MAG - Metal Active Gas

MIG - Metal Inert Gas

OM - Optical Microscope

SEM - Scanning Electron Microscope

S-N Curve - Stress-Number of cycles Curve

SIF - Stress Intensity Factor

VHSS - Very High-Strength Steel

WM - Weld Material

1 Introduction

1.1 Motivation of the MSc Thesis

Offshore renewable energies have been receiving a lot of attention and application in recent years, as they are a key part of the global transition to a more sustainable and resilient energy system. Steel plates, pipes, profiles, and tubular parts are used to construct offshore installations, which are joined together via welded connections [1].

Offshore wind energy generation is particularly promising, as offshore sites provide vast and clear expanses with strong and steady wind resources. These areas frequently receive higher wind speeds than onshore sites, leading to improved energy production potential. Furthermore, the offshore environment allows for the deployment of a higher number of wind turbines, allowing for the establishment of large-scale wind farms capable of delivering huge amounts of clean and sustainable power [1]. However, these structures are subjected to cyclic environmental loadings such as waves and wind loads throughout their lifespans, creating cyclic stress variations in their structural components. As a result, it is critical to undertake a thorough fatigue resistance investigation for these parts, particularly in welded connections, which are prone to cracking formation due to damage accumulation [2].

This thesis was developed under the project *AARM 4.0: Aços de Alta Resistência na Metalomecânica 4.0*, in order to achieve the Materials Engineering master's degree at the Faculty of Engineering of the University of Porto (FEUP).

This project is a collaborative venture between the company Martifer and the non-entrepreneurial entity, Faculty of Engineering of the University of Porto (FEUP). Nowadays, the market demands the efficiency of high-strength steel, combining its mechanical properties with the construction of lighter and more adaptable steel structures, for different industries.

During the course of this campaign, the rotational bending fatigue performance of the structural steel S690QL was compared with the metallographic characterization of its microstructure and structural integrity. Welding joints were developed at the Martifer facilities using gas metal arc welding (GMAW) with its subsequent process, metal active gas welding (MAG), with different specifications and standards.

1.2 Organization and Objectives

The primary objective of this project is to develop cutting and welding techniques for high-strength steels, which are difficult to process but offer advantages in terms of cost reduction and sustainability. The present work, entitled *Fatigue performance of a S690QL steel welded connection under a rotating bending fatigue test* can be summarized into the following three main parts:

- Literature review: A review of the relevant literature was conducted to identify the current state of knowledge on the fatigue, welding and high-strength steels
- Methodology: The methodology used in the study is described in detail. This includes the materials and methods used, as well as the experimental procedures. The experimental procedures included a rotating bending fatigue test, a hardness test, and a microstructure analysis.
- Conclusions: The conclusions of the study are presented. The conclusions summarize the main findings of the study and discuss the implications of the findings.

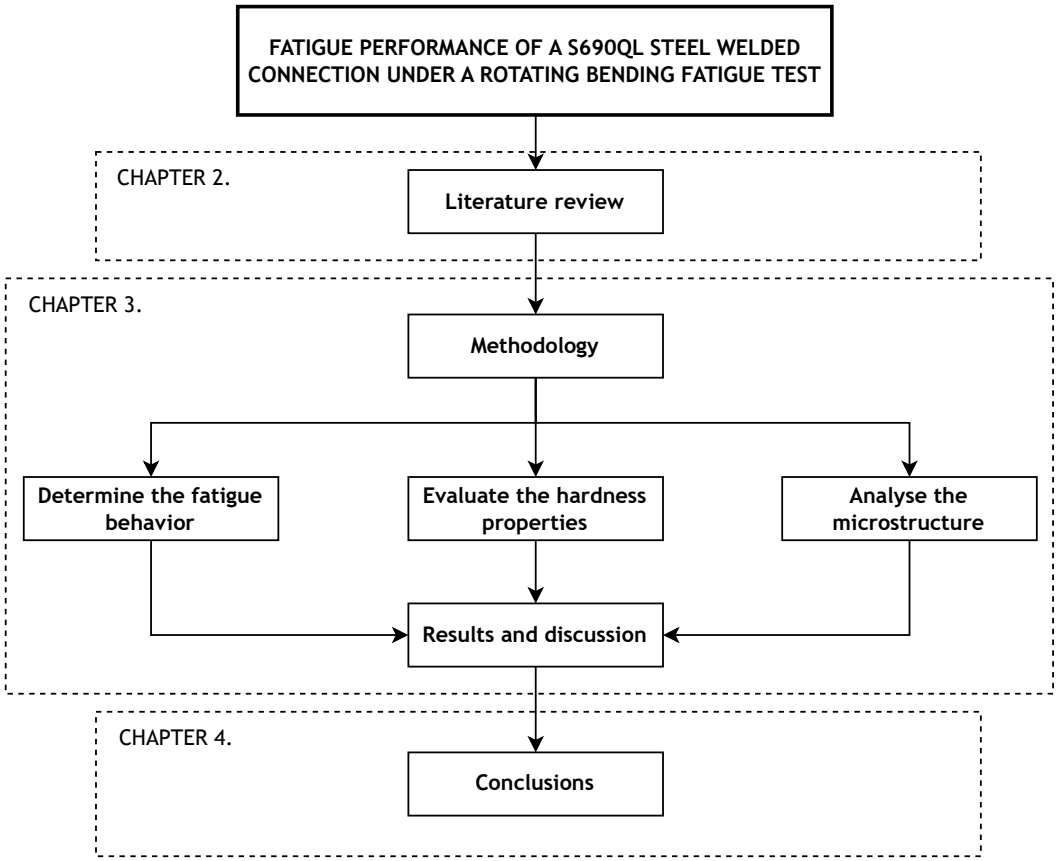


Figure 1: Main framework for the MSc thesis.

1.3 Martifer Group

Martifer is a leading company with over 30 years of experience in the metallic structures sector, specializing in large and complex projects. The company offers innovative, global engineering solutions in the fields of steel construction, aluminum and glass facades, and the oil and gas industries. Since 2008, the shipbuilding industry is a reality at the core of the company, with two shipyards located in Portugal, with the capacity to repair and construct medium and large-sized vessels. Martifer Renewables is a sector focused on the development of wind power and photovoltaic systems, addressing the present global need, for a more sustainable industry.

Figure 2: Martifer Group's logo, [3].

2 Literature Review

2.1 Overview of High-Strength Low-Alloy Steel and its Properties

The use of high-strength steels (HSS) and very high-strength steels (VHSS) is becoming more prevalent in civil engineering projects, particularly in high-rise buildings, mobile cranes, off-shore structures, and long-span bridges. These materials offer benefits such as weight reduction, longer life spans, reduced lifting and transport costs, and greater load-carrying capacities. Moreover, HSS and VHSS have higher strength and maintain consistent properties over time, can be easily connected, are suitable for prefabrication, and can be shaped into a wide variety of forms [4]. Mass reduction can be achieved by the reduced cross-section that these types of steels can provide, due to their excellent mechanical properties. The use of heat treatments such as quenching provides strength to these materials, however, it also raises concerns about the brittleness induced by these treatments [5]. To address this issue, these grades of steel are submitted to a post-treatment of tempering, which increases ductility and toughness, inhibiting most of the failures associated with brittleness [6].

The presence of certain alloying elements in the chemical composition of these steels also gives them certain relevant properties. In addition to having a low carbon content, high-strength low-alloy (HSLA) steels are micro-alloyed with titanium, vanadium, niobium, and aluminum. Additionally to some steel strengthening techniques, such as grain size refinement, these elements form carbides and nitrites that enhance strength and toughness [7]. Molybdenum and chromium are used to enable the formation of bainite, as the lower carbon content inhibits the existence of inter lath cementite, improving the fracture toughness of the bainitic phase [7]. On the other hand, metal hardenability is conferred by the consequence of manganese and nickel content allowing the formation of acicular ferrite, while Ni enhances the strengthening mechanism of solid solution. Due to the fine grain size of this structure, maximum resistance to crack propagation is obtained. The volume fraction of each possible occurring phase highly depends on the proportion of alloying elements in the composition and on the established parameters, such as cooling rates, that are one of the main steps that conduct the final microstructure [7].

S690QL is a high-strength quenched and tempered structural steel that is commonly used in construction and engineering applications where high strength and low weight are required, as discussed before. Its designation refers to a minimum of 690 MPa yield strength. The low carbon content of this steel leads to a decrease in the martensite hardness and also raises the M_s level, so martensite can be more easily formed during cooling, leading to a good junction between high strength and high toughness of this steel grade [8]. The ability of such alloys to be hardened is also ensured by alloying with Mn, Cr, Ni, and Mo. These alloys' toughness and ductile-brittle transition temperature are both markedly improved by the addition of Ni [8].

2.2 Fatigue Behaviour of Steels

Fatigue is a primary phenomenon that leads to catastrophic failure in industrial structures, making it essential to evaluate and study this complex phenomenon influenced by numerous parameters. It is defined as the modification of the material's properties due to the application of cyclic stresses, which can cause fractures below its mechanical strength or even yield strength when repeated. Many accidents have occurred due to fatigue failures, prompting engineers like A. Wöhler to study this phenomenon and its occurrence in materials [9].

Fatigue life is known to be affected by a wide variety of factors, including cyclic and residual stresses, material properties, internal discontinuities, surface roughness, corrosion, and much more, leading to a high degree of results' scatter, demanding a statistical analysis to be conducted [9, 10].

The damage mechanism of a fatigue failure is divided into different steps, where the crack nucleation starts on a micro-scale, followed by its growth to a macroscopic size and catastrophic failure in the last cycle. Each stage of fatigue life has an associated stress state used to predict and measure it, as seen in Figure 3.

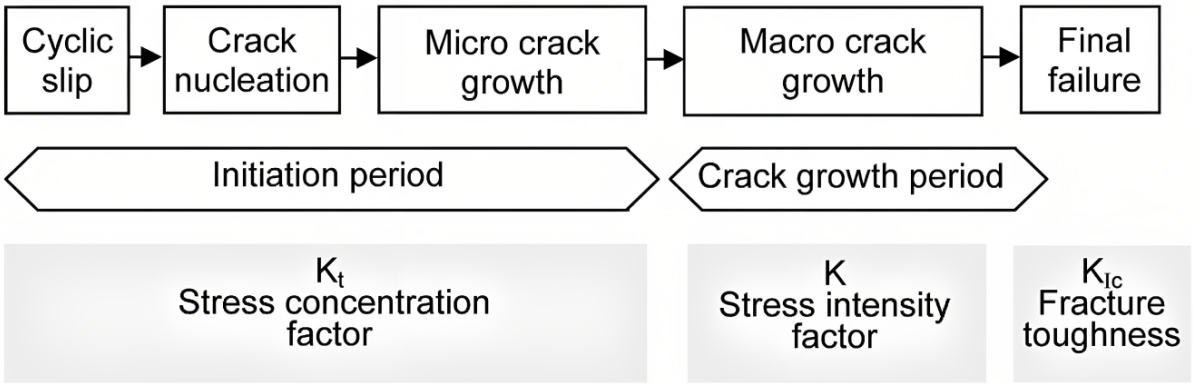


Figure 3: Various stages of the fatigue life and pertinent variables, adapted from [11].

2.2.1 Fatigue crack initiation

The first stage of fatigue crack nucleation is a consequence of cyclic slip due to dislocation activities. At the surface of a specimen subjected to fatigue loads, it is observed that localized deformation bands appear, known as persistent slip, that requires cyclic shear stress. Nucleation sites tend to be located in the free surfaces of the materials, as they are less constrained by neighboring grains. Since surface grains are more likely to undergo plastic deformation than subsurface ones, crack initiation at lower stress levels is possible. It should also be noted that the crack initiation period covers the largest part of the total fatigue life [11].

Depending on each grain's size, shape, crystallographic orientation, and elastic anisotropy, shear stress is heterogeneously distributed across the material´s surface on a micro-scale. As a result, some grains are more likely than others to experience a cyclic slip, although it can occur simultaneously in several locations [11, 12]. Figure 4 schematically demonstrates the mechanics behind the formation of a slip step and how this increases the tendency for crack nucleation.

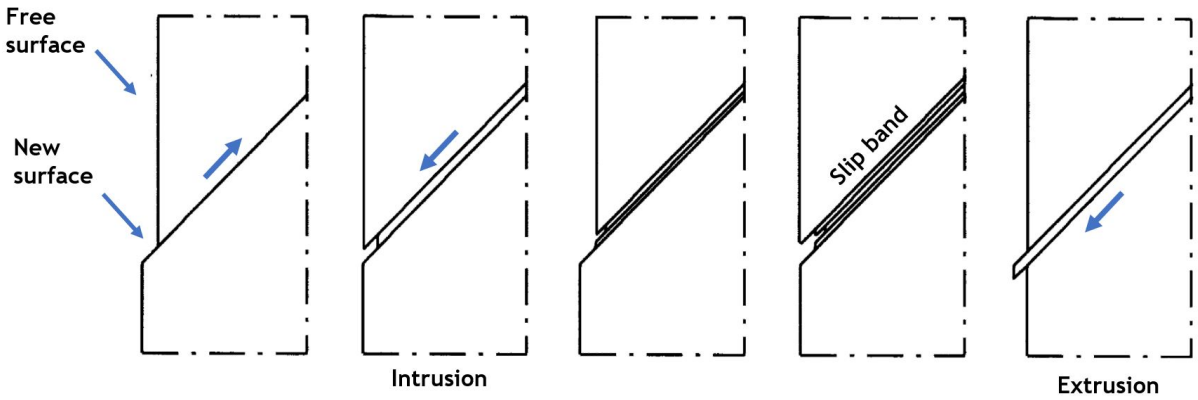


Figure 4: Crack nucleation as a result of a cyclic slip, adapted from [11].

Slip bands form inside a crystalline structure due to the movement of dislocations. Dislocations are line defects that occur within a crystal lattice when one plane of atoms slips across another plane. When a material is subjected to cyclic shear stress, the dislocations move in response to the stress, causing a deformation of the structure. As the dislocations move, they create regions of localized deformation called slip bands. These act as stress concentrators, causing further deformation and promoting the formation of microcracks within the material [12].

According to some authors [11, 12], as the stress amplitude increases, more microcracks have the potential to grow to larger sizes because thresholds are more easily overcome at higher stress levels, leading to more crack nucleation sites.

Although the crack initiation period is mainly a material surface-related phenomenon, other metallurgical factors have a direct impact on this stage. For instance, the service conditions, hydrogen content, inclusion percentage, incorrect processing parameters, and surface damage on the component can all have a negative impact on fatigue life [13].

2.2.2 Fracture mechanics

Given the high concentration of stress at the tip of the crack, the nucleation of a microcrack contributes to a heterogeneous distribution of stress on a microlevel. This phenomenon can result in multi-slip system activation. As the crack progressively increases, it tends to grow perpendicularly to the loading direction, deviating from the first slip band orientation of 45º, as can be observed in Figure 5.a) [11].

Since crack growth is directly dependent on the material bulk properties, some metallurgical elements act as thresholds for its consistent propagation. Grain boundaries presented in the material microstructure are one example of this. As seen in Figure 5.b), when the crack tip approached the first grain boundary, the crack growth rate, measured as a crack length increment per cycle, decreased. After passing through the barrier, the crack growth rate increased during the growth into the next grain but once more decreased as it approached the second grain boundary. After passing through the grain boundary, the microcrack continued to grow at a steady rate [11, 12].

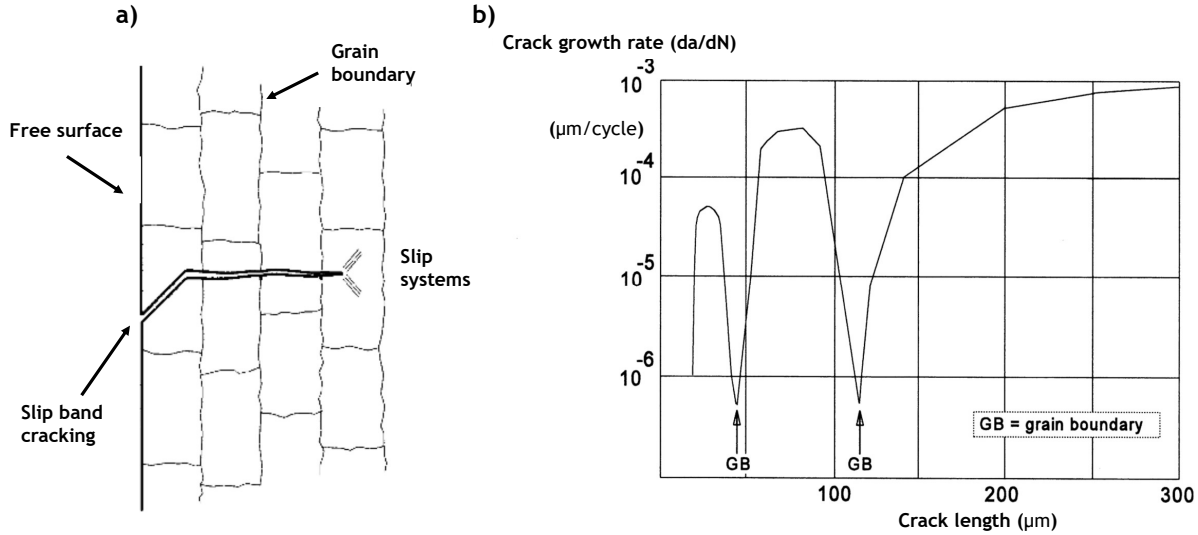


Figure 5: a) Fatigue crack propagation cross-section; b) Grain boundary acting as a threshold of crack growth, adapted from [11].

The stress intensity factor (SIF), K, is a parameter for describing the stress state at the tip of the crack in linear elastic fracture mechanics. This theoretical concept is helpful in defining failure criteria for metallic materials that commonly experience fatigue crack growth challenges. The stress intensity factors are determined by a geometry factor, Y, nominal stress, σ_g, and crack length, a, as shown in equation 1 [14, 15].

$$K = Y\sigma_g\sqrt{\pi a} \tag{1}$$

To determine and correlate the fatigue crack propagation rate, Paris Erdogan [16] related da/dN with ΔK ($K_{max} - K_{min}$), where a stands for the crack length, N is the number of cycles and K is the intensity factor coefficient, in proportion to the nominal stress. This function empirically accounts for the influence of various parameters. As a result, the C and m parameters of the Paris equation are affected not only by the material properties but also by the test conditions, such as the R ratio and environment [17]. Equation 2 represents the basic equation for Paris' law.

$$\frac{da}{dN} = C(\Delta K)^m \tag{2}$$

The stress intensity factor is used to discuss the crack tip's physical characteristics. In contrast to the initiation phase, where reversed shear stress act as a mechanism, the propagation stage is driven by negative to positive tension loading mechanisms, with negative tensions responsible for crack closure and positive tensions for crack propagation. From this macrocrack behaviour phase, three main regions can be distinguished, as displayed in Figure 6.

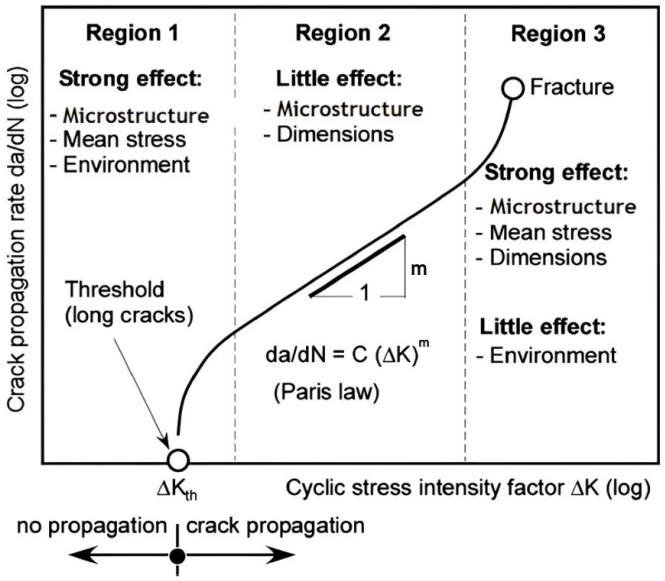


Figure 6: *da/dN-ΔK* curve of crack propagation in three different regions, adapted from [18].

Region I

In this initial stage, as discussed before, the crack propagates along the crystalline planes, where the shear stress is the highest at 45°. Since the plastic zone is so small and contained within the material's grains, the crack spreads until it is slowed down by grain boundaries, inclusions, or other microstructure barriers. This is why the crack growth is extremely influenced by the microstructure and stress level [19]. Also, in this regime, there is a stress level at the crack tip that must be exceeded in order for the crack to continue, called the threshold level, ΔK_{th}. For values of K lower than this level, the fatigue crack growth is considered to be nonexistent or its evolution is happening at non-detectable rates [12].

Region II

In this region, the crack moves perpendicular to the loading direction rather than following the maximum shear direction. Its behaviour can now be explained by Paris' law and is con-

sistent with the linear section of the curve [12, 18]. Then, crack growth occurs as the crack tip is repeatedly compressed and blunted during each loading cycle. The process produces striations, also known as ripples, which create wave patterns at the fractured grains [12].

Region III

In the final region, when the K_{max} comes closer to K_{IC} (fracture toughness), the fatigue crack growth turns unstable as it rapidly increases. In this regime, the final failure occurs, being highly dependent on the microstructure, stress amplitude, and dimensions of the component [19, 18]. The striations now are much larger, compared to the last stage, produced in the very last percentage of cycles prior to failure [12].

2.2.3 Fatigue statistical planning and analysis of data

The Wöhler's curve, also known as the S-N curve (Stress-Number of cycles curve) is the result of a series of fatigue tests at various stress amplitudes. This curve represents the relationship between the applied stress (*S*) and the number of cycles until failure (*N*), with each axis being normally in the logarithmic form [11]. Figure 7 represents a common S-N curve and, as expected, the number of cycles until fracture increases for lower stress levels. Also, it is important to notice that there appears to be a stress level beneath which no fracture occurs, which is significantly lower than the yield stress. This level is considered as the fatigue or endurance limit, s_e [12].

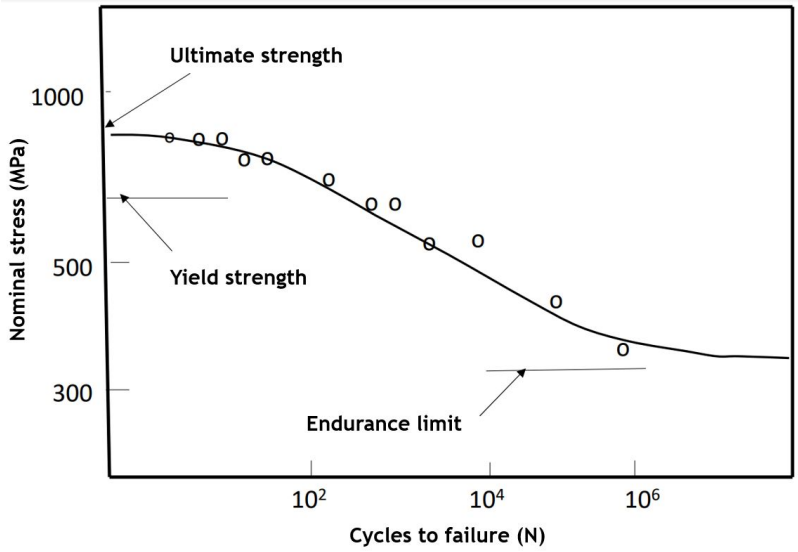


Figure 7: S-N curve graphical representation, adapted from [12].

It is critical to understand that the scatter in these tests is regarded as an inherent physical aspect of the fatigue phenomenon. Therefore, the fatigue phenomenon's characteristics must

be determined experimentally using statistical methods [20]. It is possible to logically split the scatter observed in this test into three main parts: internal to the material; concerning the processing of the component; and external to the specimen. The most common external causes are related to the uncertainty within the test machine settings, while inclusions and other structure heterogeneities are known to be associated with internal material mechanisms [20].

As referred before, the S-N curve is a global fatigue approach that relates the stress range with the fatigue life. However, local and fracture mechanics fatigue approaches can be used as alternatives for fatigue analysis and design, requiring an essential understanding of the base material's fundamental fatigue characteristics [21]. Recognizing the confined character of fatigue damage, the local methods suggest a link between a local damage parameter, such as strain or energy, and the number of cycles necessary to start a macroscopic fracture, for low-cycle and high-cycle fatigue tests [21].

As early as 1910, Basquin proposed that the logarithm of the number of cycles to failure and the logarithm of the stress amplitude have a linear relationship. The Basquin equation is a stress-based fatigue model and it can be expressed as in equation 3, where $\sigma_f^{'}$ and b are fatigue strength coefficients [22].

$$\frac{\Delta\sigma}{2} = \sigma_f^{'}(2N_f)^b \tag{3}$$

The fact that the Basquin equation can accurately predict fatigue life under a variety of loading conditions while being relatively simple to use is one of its main benefits. The Coffin-Manson is a strain-based fatigue model and it is commonly used for the design of metallic components subjected to low-cycle fatigue. Equation 4 represents mathematically this law, where $\Delta\varepsilon_\rho/2$ is the plastic strain amplitude, $\varepsilon_f^{'}$ the fatigue ductility coefficient, and c a fatigue ductility exponent determined experimentally [23, 24].

$$\frac{\Delta\varepsilon_p}{2} = \varepsilon_f' \left(2N_f\right)^c \tag{4}$$

While Basquin and Coffin-Manson describe a relationship between the number of cycles until fracture for two separated regimes, high and low-cycle fatigue life respectively, Morrow's equation combines the elastic and plastic strain domains into a single relationship, as presented in equation 5 [25].

$$\frac{\Delta\varepsilon}{2} = \frac{\sigma_f' - \sigma_m}{E}\left(2N_f\right)^b + \varepsilon_f' \left(2N_f\right)^c \tag{5}$$

2.3 Welding Techniques - Electric Arc Welding

Many metalwork industries constantly demand different types of methods to join separate components to produce a single final structure. For this purpose, some welding techniques are used to metallurgically bond different parts into a single entity by heating and or pressing the surfaces to their melting points, providing durability and quality to the welded joint. This process enables the union of a wide range of similar and dissimilar materials and thicknesses, allowing it to be used for welding large structures. It can be used with or without filler material, and the welded joint must have higher strength than the base material since is regarded as a critical point [26]. Some joints are considered a metallurgical bond due to the high temperatures used for the fusion of material, which involves the diffusion of atoms along the crystalline structure, forming primary atomic bonds, providing great resistance to the welded connection [27].

As mentioned before, there is a wide variety of welding processes available, that directly impact heat source, whether there is material fusion, and if they use or do not use filler materials. Each technology is associated with the best-suited application and range of materials that can be utilized. Figure 8 simplifies the array of processes available.

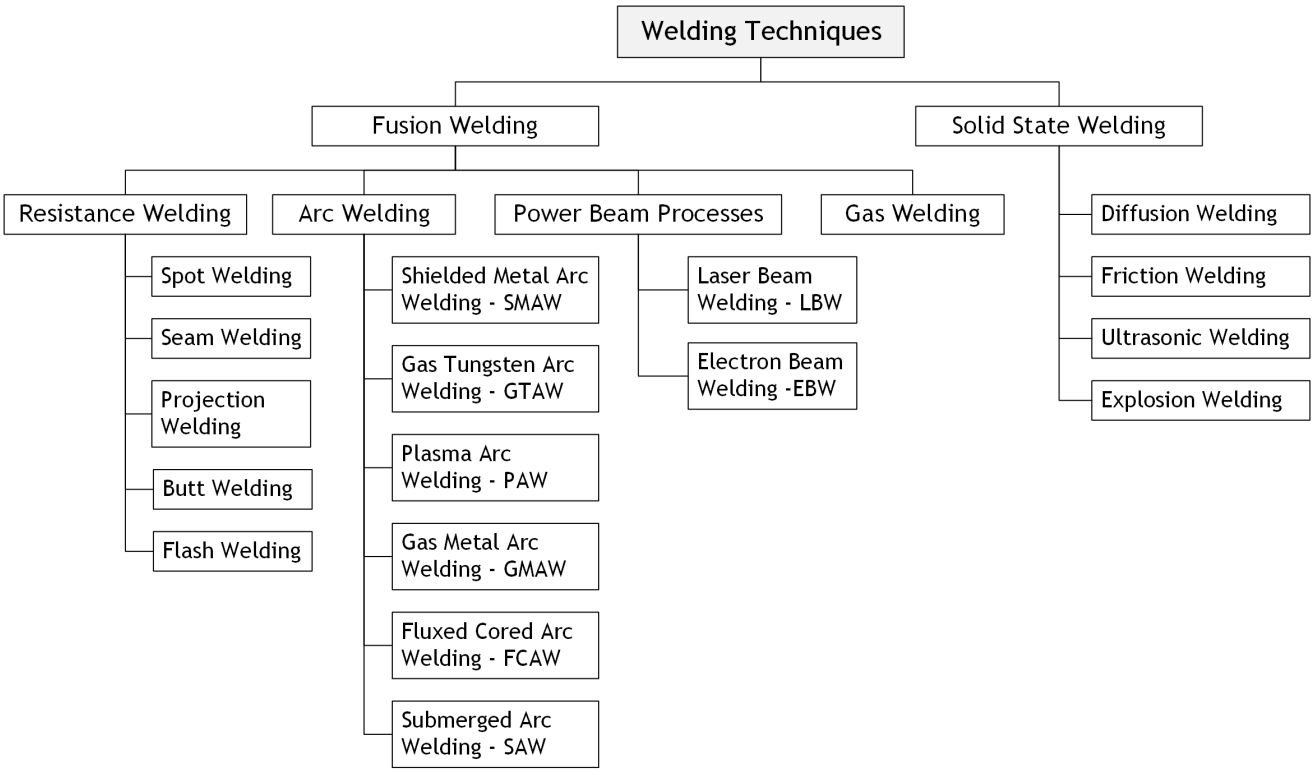


Figure 8: Schematic representation of the common welding processes, adapted from [28].

An electrical discharge between the electrode and the workpiece forms a welding arc. The

electric current is conducted between the two electrodes through a heated and ionized gas, creating a mixture of free electrons and ions, called plasma. The base and filler materials in arc welding are melted as a result of the arc's conversion of electrical energy into thermal energy. The arc stability will be directly influenced by the choice of shielding gas since the temperatures needed to maintain the gas ionized will vary. For example, helium provides a more unstable arc than argon due to its higher ionization energy. The instability of the process can lead to a decrease in productivity and a higher chance of defects [28].

2.3.1 Gas Metal Arc Welding

Gas Metal Arc Welding (GMAW), as defined by the American Welding Society (AWS), is a process where an arc is formed between a continuously fed filler metal and the workpiece, together with a separately applied shielding gas. The heat generated from this arc will heat and fuse both metals, creating a uniform welded joint. Since the filler material is automatically provided to the nozzle, it is considered to be a semi-automatic process [29, 30].

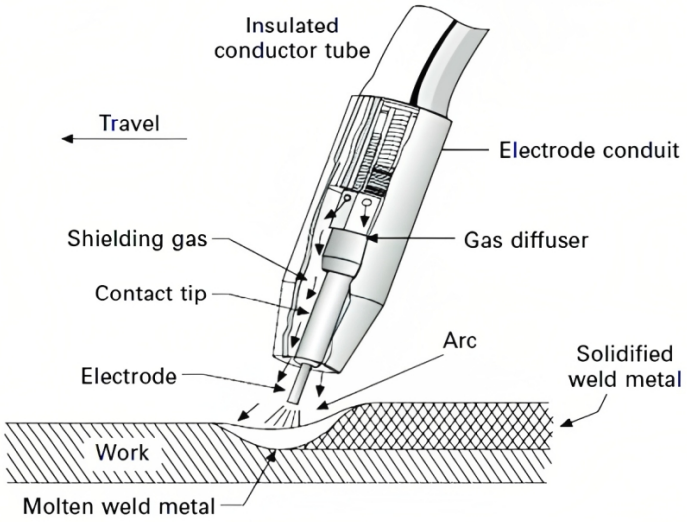


Figure 9: Work principle of GMAW process [31].

Direct current electrode positive (DCEP) polarity is used in the vast majority of GMAW applications, where the ground clamp is attached to the negative terminal [32]. With this condition, the stability of the arc, consistent metal transfer, low spatter levels, favorable weld bead characteristics, and deep weld penetration can be achieved across a range of welding currents. In DCEP mode, almost 70% of the heat is concentrated on the electrode, leading to higher deposition rates [33]. On the other hand, using direct current electrode negative (DCEN) results in larger droplets with an irregular transfer, leading to an increase of spatter grains [34].

For this technology, a constant voltage (CV) power source is used for self-regulating the electric arc. Since the torch position may vary along the welding joint, the depth of penetration will be influenced by the arc length, promoting discontinuities along the joint. According to National Electrical Manufacturers Association (NEMA), a CV power source has the capacity to adjust the load voltage and has a static volt-ampere curve that produces a constant load voltage tendency, as seen in Figure 10 [35]. For this type of power source, an increase in the electrode extension, arc length, or contact tip to work distance (CTWD) in general, leads to a decrease in the welding current [36].

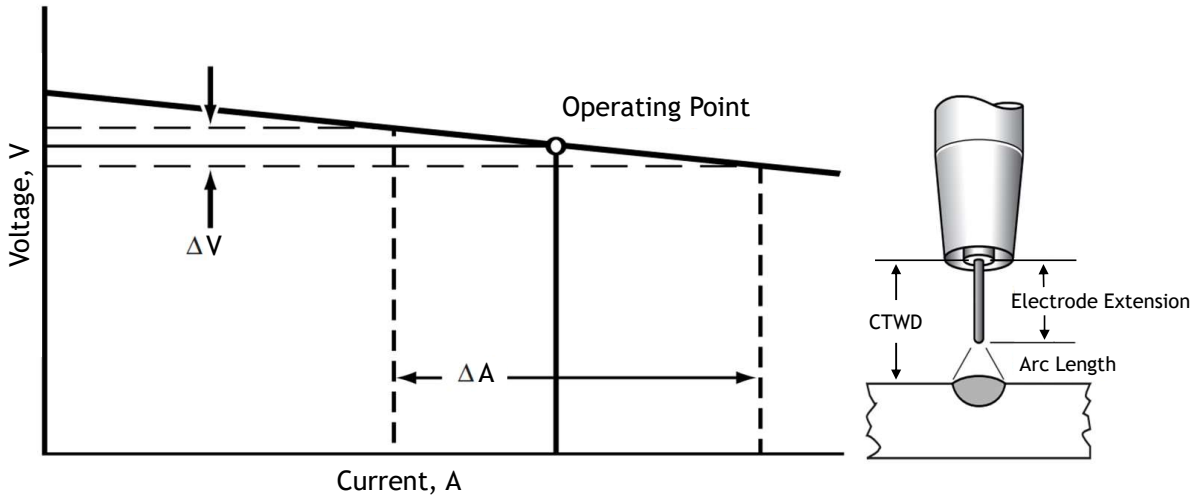


Figure 10: Characteristic Volt-Ampere curve, adapted from [36].

2.3.2 Shielding gases

As referred before, this process is assisted by the external introduction of a mixture of shielding gas. The main function of the shielding gases is to inhibit the interaction between the molten pool and the atmosphere, preventing the formation of metal oxides and other defects. Additionally, the protective gases' composition and flow impact the process characteristics, such as transfer mode, arc stability, penetration, etc [37]. The composition of the shielding gas will depend on the type of filler material and the base metal used.

There are two basic classifications for the shielding gases available: active and inert gases, which indicate the nomenclature for the GMAW process variant. The welding method is known as metal active gas welding (MAG) if the shielding gas combination contains active gases, such as carbon dioxide or oxygen. Alternatively, the process is known as metal inert gas welding (MIG) if the mixture contains inert gases like argon or helium [30, 32]. Nonferrous metals, stainless steel, and some alloy steels are frequently processed using inert gases and their combinations, whereas ferrous metals are processed using active ones. During the welding process of ferrous metals, a combination of inert and reactive gases may also be used [8]. For

instance, in the metal inert process, argon requires lower voltages for any amperage setting, due to its lower electric resistance when compared with helium, being better suited for thin metal welding. On the other hand, the arc stability of He occurs for higher voltages, leading to the increase in penetration depth and weld speeds [38].

2.3.3 Transfer modes

Depending on several types of variables, such as weld arc voltage and current, the composition of shielding gas, filler wire diameter, and wire feed rate, there are three main modes of transferring the filler metal across the welding arc.

Short-circuit transfer occurs at the lowest possible electrode diameters and welding currents. When the electrode tip short-circuits, in other words, when it meets the pool surface, the molten metal from the electrode tip is transferred to the weld pool. This transfer mode is suitable for positional welding and/or welding thin sheets where precise control over the weld metal pool is required [8, 39].

Globular transfer occurs when the welding parameters like wire feed speed, voltage, and amperage are greater than the short-circuiting standards, and it's more likely to happen for CO_2 and He shielding gasses. Due to the extremely high size of the droplet, the welding arc is more unstable leading to an increase in the spattering level and undesirable welding joint appearance. For this transfer mode, welding processes are limited to horizontal and flat positions [39, 40].

Spray transfer creates a stable and spatter-free axial small droplets transference across the arc due to the influence of a higher frequency and speed electromagnetic force. This transfer mode occurs only when the minimum transition current, which depends on the electrode diameter and wire feed speed, is exceeded. Also, argon-rich gases must be used for higher efficiency of the spray arc method [8, 39, 40].

2.4 HSLA Steels Weldability

The principal difference between HSLA steels and alloy steels is that HSLA steels have microalloying elements that provide the desired strength for a given application. As a consequence of the microalloying, the material's mechanical properties are greatly impacted during heating resulting from the welding process, leading to the development of a meticulous welding procedure [41].

Weldability is the capacity to weld a metal without introducing cracks or other detrimental flaws, hence obtaining the necessary mechanical and metallurgical properties [42]. It directly depends on three distinct factors, namely material, design, and production, according

to ISO/TR 581:2005 [43]. From a metallurgical point of view, the material's weldability is governed by the chemical composition, which translates the tendency for cracking and hardening, by physical properties, such as thermal conductivity and expansion behaviour, and by metallurgical properties like segregations, inclusions, and grain size, that directly influence the material's performance [43].

Since high-strength steels are more susceptible to cracking than mild steels, it is essential to maintain proper heat management both before and throughout the welding process. Preheating treatments help control the temperature gradient since fast temperature changes during heating and cooling in a cold piece can lead to the formation of cracks. Also, the use of pre-heating tends to minimize the hydrogen levels, reducing the tendency of hydrogen-induced cracking. The heat parameters directly depend on the exact grade of high-strength steel and its thickness [44].

Steel's hardenability will also translate to its weldability, as it represents the ease of forming unwanted hard phases, which is one of the requirements for cold-cracking. Since the hardenability property depends on the carbon and alloying elements content, the carbon equivalent equation (equation 6) will allow engineers to directly determine the susceptibility to the formation of undesirable phases [8, 45].

$$\text{CEV (\%)} = \%\text{C} + \frac{\%\text{Mn}}{6} + \frac{\%\text{Cr} + \%\text{Mo} + \%\text{V}}{5} + \frac{\%\text{Ni} + \%\text{Cu}}{15} \tag{6}$$

The heat input (Q) of the welding process will have an influence on the size of the heat-affected zone (HAZ) across the welding bead because translates the rate of cooling of the weld. The heat input is governed by the voltage (U), current (I), and welding speed (V, mm/min). Also, the heat input is influenced by the efficiency of the welding process (K). These parameters will provide the prediction of the amount of heat per length, and it can be calculated from the equation 7 [45].

$$\text{Heat Input } (Q) = \frac{V \times I \times 60}{S \times 1000} \times K \tag{7}$$

The material´s thickness is another aspect that influences the outcome of the process since it impacts the cooling rates for specific areas. In comparison to thinner materials, thicker ones have a reduced surface area-to-volume ratio. Since heat transmission takes place at the surface, a larger surface area to volume ratio enables more effective heat dissipation. Thinner materials cool rapidly because heat can be transmitted to the environment more easily due to their increased surface area in relation to volume. Different cooling rates across samples of the same material will result in differences in the microstructure and, as a result, mechanical properties.

3 Methodology

3.1 Materials

The S690QL steel was the material used in this experimental campaign. This class of steels is a subset of low alloy steels, and the EN10025-6 standard defines and regulates their chemical compositions [46]. The chemical and mechanical properties of this steel type have been previously discussed, however, understanding its nomenclature is crucial. Any structural steel is denoted by the letter ”S”, followed by the yield strength, which is approximately 690 MPa for this class of material. The letter ”Q” refers to the quenching and tempering heat treatment applied to this steel, while the letter ”L” refers to a low-notch toughness testing temperature [47]. Two distinct welded connections were performed for this experiment, one with two 30-millimeter thickness plates welded together and labeled M30, and the other with two 60-millimeter thickness plates designated M60.

The welded joints were produced using the MAG (Metal Active Gas) welding process, as designated by ISO 15609-1:2019 [48]. The filler material used for this process was the Coreweld 69 LT H4 from ESAB, as classified by ISO 18276:2017 [49]. This metal-cored electrode is suitable for welding thick high-strength steel sections (>690 MPa), featuring excellent subzero toughness down to -60 degrees Celsius. ”H4” represents the low diffusible hydrogen levels of 4 ml H/100g that this consumable provides, while being suitable for welding with Ar/CO_2 gas mixtures [50]. Table 1 shows the percentages in weight of the elements present in the chemical composition of each material used for the experimental campaign. The carbon equivalent value for filler material was directly calculated by Equation 6, while the supplier provided the values for the base material.

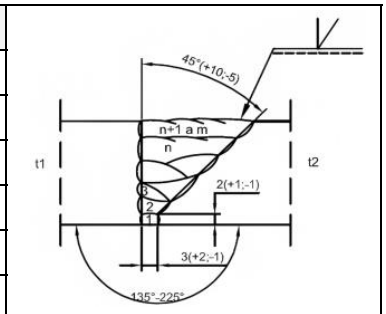
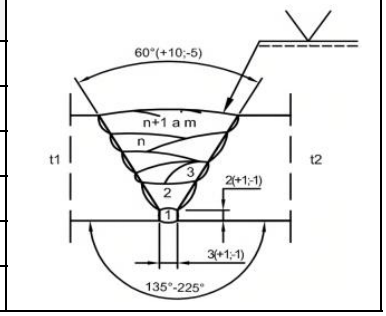
Table 1: Chemical composition of the base and filler material used in the welded joint.

	Chemical Composition (Wt. %)															
	C	Si	Mn	P	S	Cr	Mo	Ni	Al	V	Nb	Ti	Cu	N	B	CEV
S690QL (M30)	0.140	0.279	1.203	0.020	0.002	0.299	0.178	0.011	0.035	0.029	0.017	0.016	0.025	0.0029	0.0018	0.44
	Base Material: EN 10025-6 : S690QL															
S690QL (M60)	0.149	0.276	1.253	0.011	0.001	0.621	0.259	0.012	0.030	0.003	0.015	0.016	0.030	0.0030	0.0020	0.54
	Base Material: EN 10025-6 : S690QL															
Coreweld 69 LT H4	0.05	0.50	1.70	0.011	0.008	0.06	0.50	2.30	0.01	0.005	-	0.012	-	-	-	0.60
	Filler Material: EN ISO 18276-A : T 69 6 Mn2NiMo M M21 2 H5															

As previously stated, plates of two different thicknesses were welded using the MAG technique. A single-bevel butt joint was adopted on the 30-millimeter plate (M30) in the horizontal position, while a single-V joint was implemented by attending the 60-millimeter plate (M60) in the flat welding position. For both processes, the same filler material and gas mixture were

utilized, with a 20% CO_2 + 80% Ar composition as a shielding gas at a 15 to 18 l/min flow rate, belonging to the M21 - ArC - 20 group described in ISO 14175:2008 [51]. The cooling rates were gradually controlled by the application of pre-heating methods at 175ºC and 150ºC for M30 and M60, respectively. Table 2 provides a better understanding of the remaining parameters used in both processes as well as the technical planning of each butt joint.

Table 2: Process parameters and technical planning.

M30					
Welding Sequence	1	2 - n	n	n + 1 - m	
Welding Process	138 (PM)				
Polarity (-/+)	DCEP				
Welding Current (A)	100 - 150	220 - 300	230 - 320	220 - 300	
Voltage (V)	16.0 - 18.0	26.5 - 31.0	27.5 - 32.0	26.5 - 32.0	
Wire Feeding Speed (m/min)	2.5 - 3.5	7.0 - 10.0	8.0 - 11.0	7.0 - 10.0	
M60					
Welding Sequence	1	2 - n	n	n + 1 - m	
Welding Process	138 (PM)				
Polarity (-/+)	DCEP				
Welding Current (A)	100 - 150	220 - 300	230 - 320	200 - 300	
Voltage (V)	16.0 - 18.0	26.5 - 31.0	27.5 - 32.0	26.5 - 32.0	
Wire Feeding Speed (m/min)	2.5 - 3.5	7.0 - 10.0	8.0 - 11.0	7.0 - 10.0	

From Table 2 it can be inferred that the welding current fluctuated between 100 and 320 Amperes for samples M30 and M60 where MAG welding technology was used, while the voltage ranged from 16 to 32 Volts, and it is clear that these values vary depending on the welding sequence. The wire feeding speed was the same for both processes, varying between 2.5 and 11 m/min.

The main mechanical properties of materials used for this experimental campaign can be observed in Table 3. Since the fatigue resistance varies on a number of external mechanical aspects, this will aid in drawing stronger conclusions regarding the fatigue data acquired.

Table 3: Mechanical properties of the base and filler material used in the welding process.

	Mechanical Properties		
	Yield strength, $R_{p0.2}$ (Mpa)	Tensile strength, R_m (Mpa)	Elongation, A (%)
S690QL (M30)	814	857	17.0
S690QL (M60)	758	835	14.4
Coreweld 69 LT H4	755	790	20.0

3.2 Experimental Procedure

3.2.1 Rotating bending fatigue test

The water-jet cutting technique was used to cut each welded plate into longitudinal and transversal sections from which the test specimens will subsequently be machined for the rotating bending fatigue test, as it is shown in Figure 11.

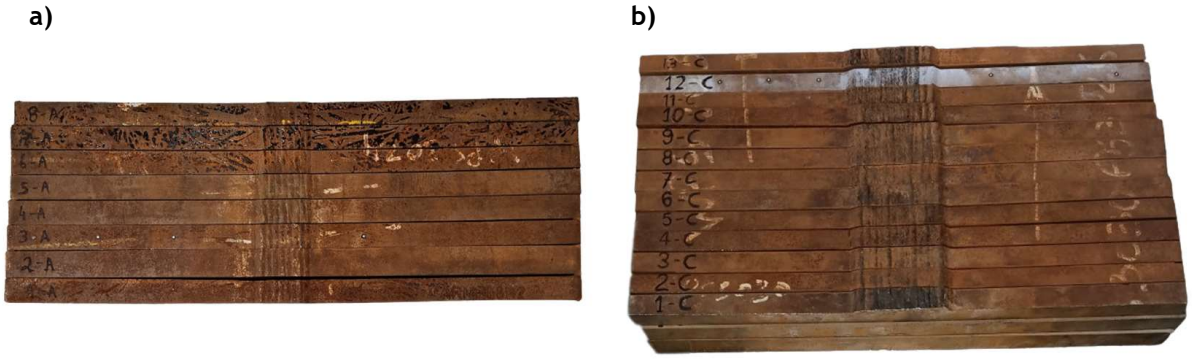


Figure 11: S690QL longitudinal and transversal sections of a) M30 and b) M60 plates.

The technical plan of the two main longitudinal sections, A and B, for the M30 plate are shown in Appendix A, while the longitudinal sections C, D, and E of the M60 plate are shown in Appendix B, where the heat-affected zone is marked in red. For the M30 plate, 24 specimens from each section (A and B) were extracted to test the base material (BM), heat-affected zone (HAZ), and weld material (WM). Specifically, 16 specimens were from the base material, 4 from the heat-affected zone, and 4 from the weld material, as indicated in the technical plan. For the M60 plate, 36 specimens were extracted for section C, more precisely, 24 from the base material, 12 from the heat-affected zone, and 12 for the weld material. Only the HAZ and WM for sections D and E were experimentally studied, with 12 samples being taken from each zone. The samples were machined and polished according to the dimensions presented in Figure 12 for each longitudinal cut, following ISO 1143:2010 [52].

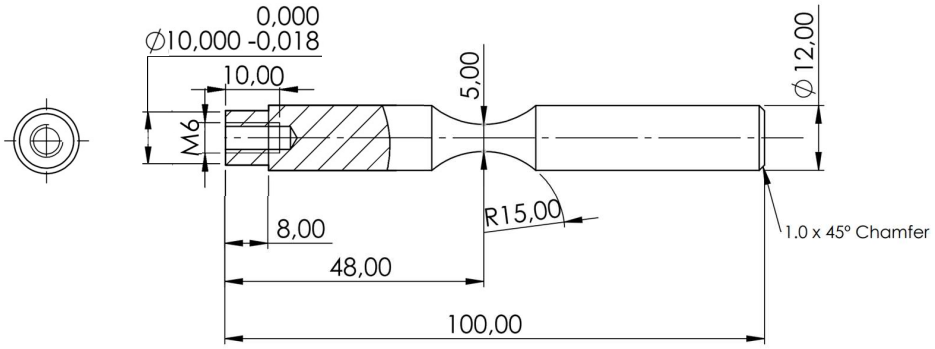


Figure 12: Geometry and dimensions of the fatigue test specimens, in millimeters.

Each specimen was polished in the shortest region with a P4000-Grit silicon carbide sandpaper and a mechanical lathe for 1 minute before the fatigue test. This ensured that all samples had the same surface roughness, thus reducing the scatter of the results for the final statistical analysis.

The specimens were tested as traction-compression tests, with a $R = -1$ and $f = 23Hz$, where R is the ratio between the minimum stress σ_{min} and the maximum stress σ_{max} [20]. This type of test allows for the observation of the effect of cyclic stress across the specimen's section. Figure 13(a) shows a schematic view of the specimen fixture system in the rotating motor, while Figure 13(b) illustrates the principle of the rotating bending fatigue test and the tension-compression stress profile over time.

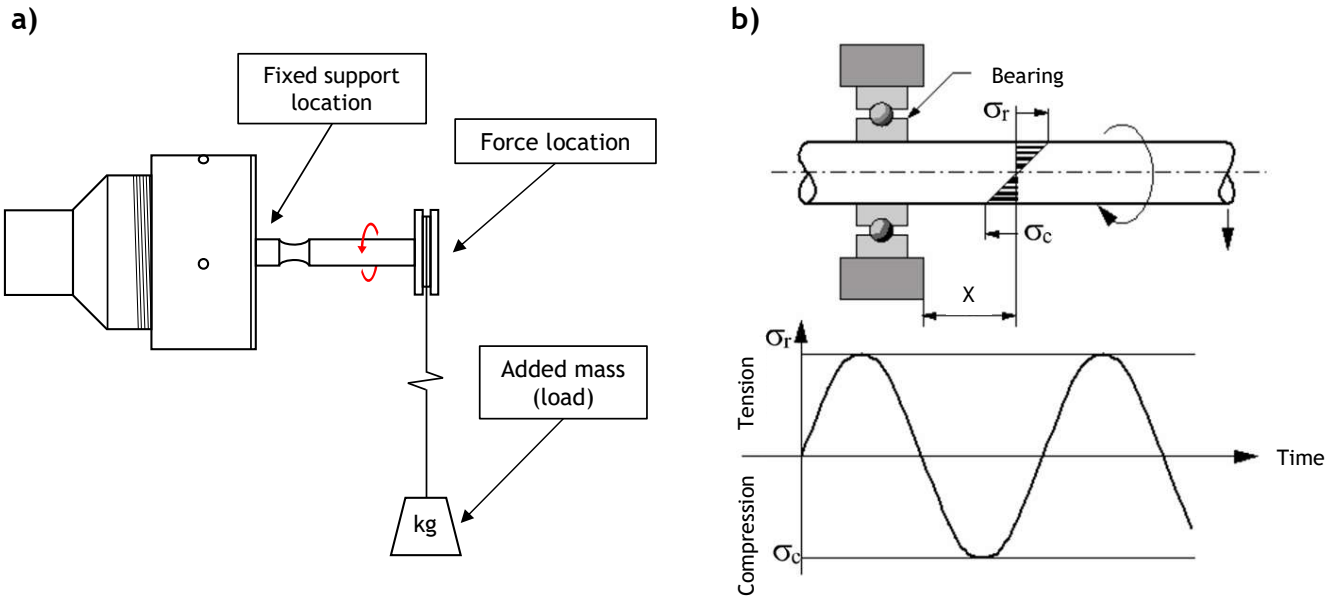


Figure 13: a) Schematic representation of the test system; b) Principle of rotating bending tests, adapted from [20].

One side of the specimen was held in place using a fixed support, and approximately 36.5 mm of the specimen length was positioned inside the clamping system. The minimum section, where the maximum stresses were applied, and the load region, where the external force was applied, are also important to note. The testing system consisted of a sheave, steel wire, hook, and bucket, in which a weight was added to create tension for the specimens. It is worth noting that the weight of each component of the system was taken into consideration. Each individual specimen was measured to record the precise measurements after machining, which would be used to calculate the exact weight required to bear the necessary stress. It is important to note that, in order to reduce the related error, some dimensions were the average of three readings. Figure 14 depicts the essential measurements taken from each sample in order to proceed with the rotating bending fatigue test.

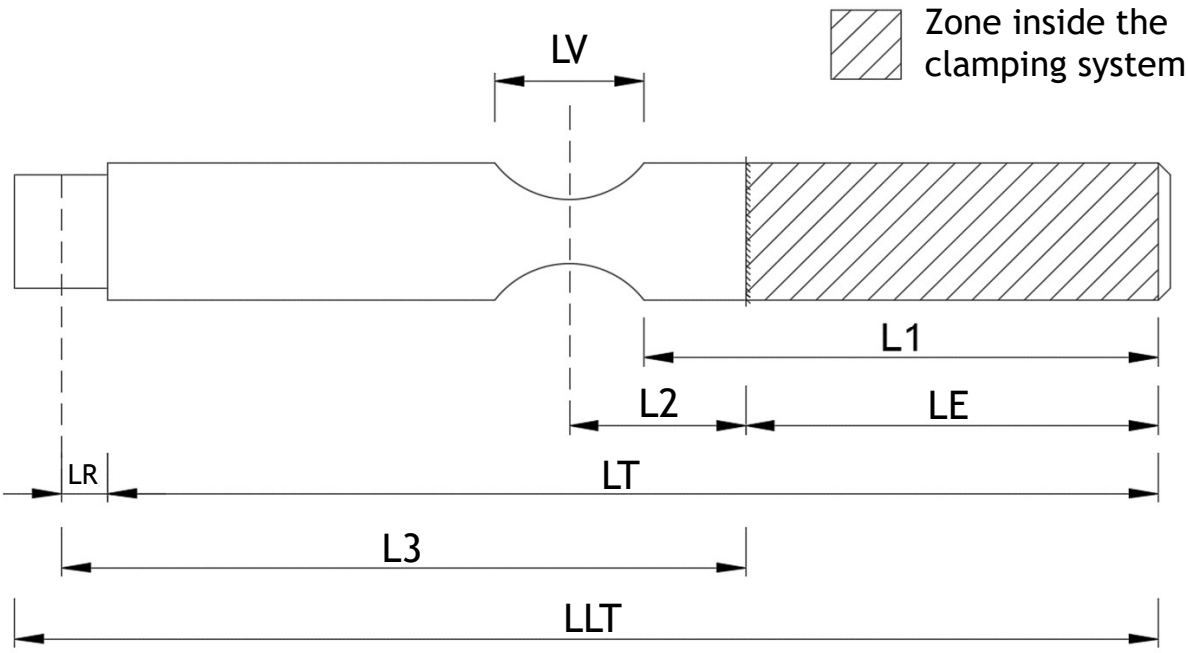


Figure 14: Dimensions to carry on in the fatigue test.

The highest bending moment was at the origin (fixed support), but it was not the region with the highest stresses; instead, the highest stresses occurred in the region with the smallest diameter. The maximum bending stress (σ) on the specimen surface is given by Equation 8, as well as the circular moment of inertia of a circular cross-section in Equation 9.

$$\sigma = \frac{M}{I} \times \frac{d_0}{2} \tag{8}$$

$$I = \frac{\pi d^4}{64} \tag{9}$$

In this equation, M is the bending moment applied in the region with the smallest diameter where the maximum stress is located. It can be calculated by multiplying the force F by the distance from the smallest cross-section to the point of load application. In addition, I is the circular moment of inertia and d_0 is the diameter of the smallest region. Statistical planning and analysis of the data obtained from each test were performed according to ISO 12107:2003 [53]. The Wöhler's curve was plotted based on Basquin´s theory, given by Equation 3. A model based on the geometric modeling of the Basquin S-N curve with smoothing in the high and low-cycle fatigue areas was proposed by other authors, including Strohmeyer, Kohout, and Vechet [54, 55]. The fatigue endurance limit was set at 10^7 cycles, in accordance with ISO 12107:2003 [53]; therefore, any specimen that reached this value was considered as a run-out and was excluded from the statistical data.

To simplify the importance of the measurements and the following calculations used for each specimen, Table 4 shows an example of the dimensions measured for specimen 3-A-E, where the target stress level was 540 MPa. From these dimensions, together with the previous equations of bending stress and inertia, a value for the force (F) can be obtained. In this instance, the test should be subjected to a force of 154.709 N, which will be translated into the weight placed into the bucket system. In a shortened notch rounded section, the notch radius is typically much smaller than the specimen width. This results in a large stress concentration at the rounded notch tip, which can lead to premature failure of the specimen. The stress concentration factor (SCF) can be estimated by dividing the stress at the notch tip by the nominal stress. In this case, the SCF was relatively low.

Mesh convergence is achieved by decreasing the element size until the minimum mesh size is reached, at which point the acceptable level of accuracy is achieved. The mesh convergence study was performed to optimize the finite element model (FEM) by refining the mesh element size.

Furthermore, by simulating the stress field with the Fusion 360 software (Figure 15), it is possible to see not only that the maximum stress will occur on the thinnest section of the specimen, but also that the experimental procedure used is correct, as the maximum value is close to the target stress level, proving the presence of a stress concentration factor.

Table 4: Dimensions for the 3-E-A specimen.

Specimen	Dimensions (mm)							Target Stress (Mpa)
3-A-E	LLT	LT	L1	L2	L3	LR	LE	540
	99.04	91.68	42.16	15.22	58.07	3.46	36.57	

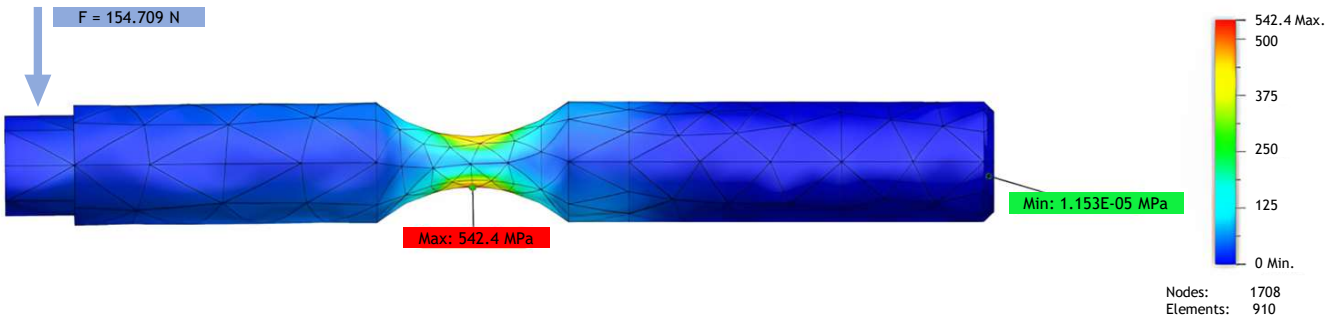


Figure 15: Numerical analysis model for the 3-E-A specimen.

3.2.2 Hardness test

Hardness tests were performed on two plates at two different stages of the welding process. For the M30 and M60 plates, one stage considered only the root steps of the process, while the other considered all welding steps. The main objective of this test plan was to study and compare the influence of the last steps on the heat input coefficient of the process. This will allow us to observe when the heat treatment of temper derived from the process drastically changes the mechanical properties of the heat-affected zone. This analysis will also allow for a better understanding of each type of microstructure and correlate it with the fatigue performance of the various zones.

The tests were performed at a macro level according to ISO 9015:2011, parts 1 and 2 [56, 57]. In order to differentiate the HAZ from the weld and base material, all the samples were chemically etched with Nital 2% before each test. Two affiliations, A and B, were performed with 10 procedures in each one. The equipment utilized for this purpose was the *EMCO M4U* hardness tester. The Vickers test used was the HV10, with an applied force of 10 kgf, corresponding to 98.07 N, with a pressing time of 15 seconds. Considering the scientific standard, the minimum distance of each measurement to the end was considered, as well as the distance between indentations. The geometry of the evaluated samples and the measures distributed for each affiliation are illustrated in Figure 16.

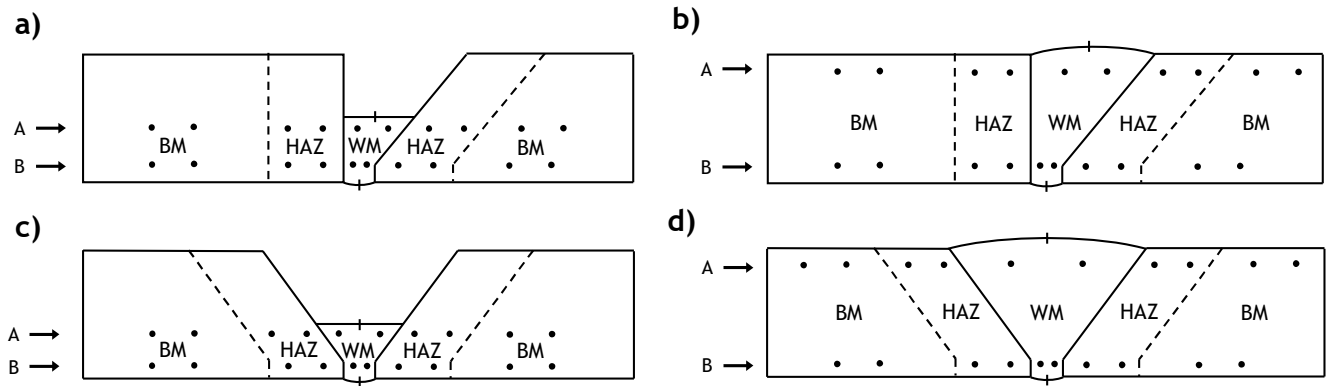


Figure 16: Geometry of the evaluated samples: a) M30 plate with root steps; b) M30 plate fully welded; c) M60 plate with root steps; d) M60 plate fully welded.

Microhardness tests were also performed to evaluate various microstructure constituents. With this analysis, it will be possible to acquire a better understanding of each type of microstructure and correlate it with the fatigue performance of the various zones. Using the *INNOVATEST Falcon 400* equipment, this test was carried out with an HV0.1 Vickers indenter, corresponding to a 0.1 kgf (0.9807 N) force applied for 15 seconds.

3.2.3 Optical and scanning electron microscopy

Optical Microscopy (OM) and Scanning Electron Microscopy (SEM) were employed to characterize the microstructure and fracture surface of the samples extracted from the M30 and M60 plates used in the hardness tests.

These samples were obtained from the welded joints by abrasive disk cutting using a *Mecatome T260* from PRESI. The OM analysis required the standard metallographic preparation, followed by the chemical etching with a Nital 4% solution to reveal the microstructure of the base and weld materials, as well as the heat-affected zone. The SEM analysis involved also a metallographic preparation with a P320–1000 grit silicon carbide sandpaper sequence, followed by a polishing step with 6 and 1 μm cloths and their respective diamond suspensions. The equipment used for OM analysis was the *LEICA DM4000M*, using *LAS X* as the predefined software. The Scanning Electron Microscopy/Energy-Dispersive X-ray Spectroscopy (SEM/EDS) analysis was performed in the CEMUP installations to obtain the chemical profiles and evaluate the variation in the chemical composition in different regions. The equipment used for this purpose was the *FEI Quanta 400FEG ESEM/EDAX Genesis X4M* of high resolution.

The main elements of interest were C, Mn, and Ni. For fractographical characterization, several fractured samples from the fatigue test were also examined using SEM/EDS. The main objective of this microscopy analysis was to understand the fracture mechanics of fatigue failure, relating the fracture surface morphology to the test conditions and different stages of crack propagation.

4 Results and Discussion

4.1 Optical microscopy analysis

The microstructure of S690QL steel after the welding process consists of three main zones: the weld material zone (WM), the heat-affected zone (HAZ), and the base material (BM). The fusion zone or weld material zone, which undergoes a liquid-to-solid transformation, is the area that has been melted by the welding arc. The HAZ is the area that has not been melted by the welding arc but has undergone changes in properties as a result of being exposed to relatively high temperatures. The base material is the area that has not been affected by the welding process heat input. Figure 17 depicts an overview of the microstructure that comprises the three main zones of the S690QL steel after the welding process.

As it is shown in Figure 18, the solidifying grains form a columnar morphology as they expand primarily along the maximum heat gradient towards the weld center. The molten metal cools from the outside in, and the grains nucleate and grow at the cooler edges of the molten pool. As the molten pool cools, the grains grow and merge, forming a columnar structure. The width of the columnar grains in the weld material zone is proportional to the size of the grains in the HAZ near the melted zone [58].

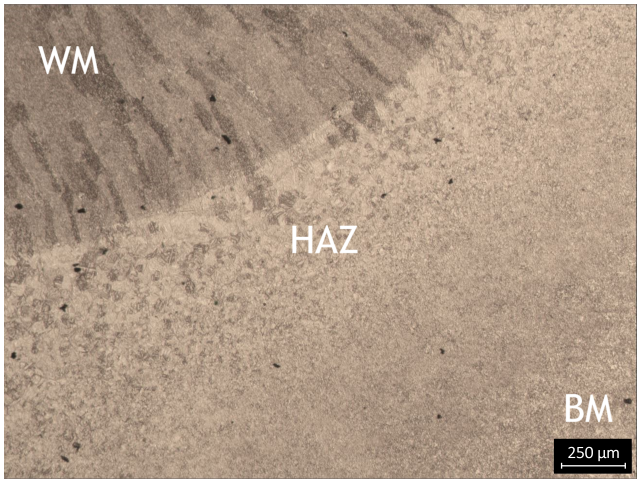


Figure 17: Overview of the microstructure highlighting the three different regions.

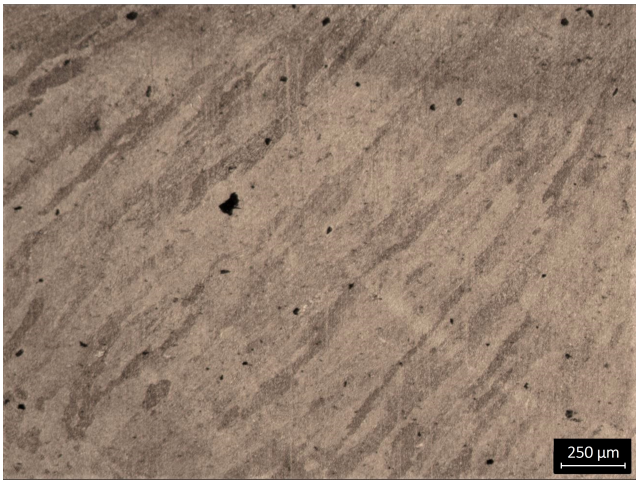


Figure 18: Columnar growth of WM grains in the fusion zone.

Sections of base metal next to the fusion zone will be subjected to one or more severe temperature cycles during welding, leading to changes in morphology and mechanical properties. The thermally affected zone is governed not only by the gradual increase of grain size towards the transition zone, but also by various subzones with somewhat varying morphologies and sizes, as illustrated in Figure 19. It is worth noting that there is no clearly defined boundary between these various microstructures, rather, there is a smooth transition of them [58].

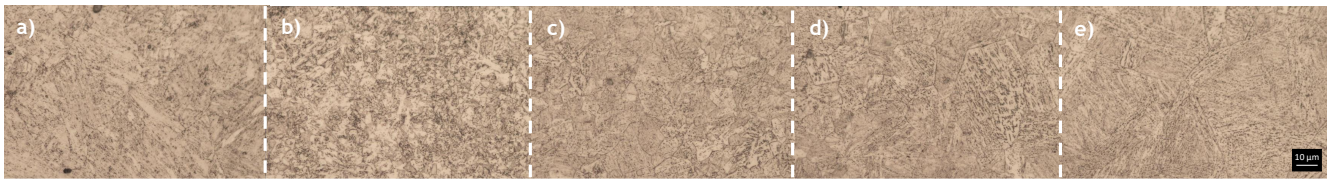


Figure 19: Microstructure of a MAG welded joint of S690QL steel with its characteristics areas: a) base material; b-e) heat-affected zone with respectively grain coarsening.

As previously mentioned, the ultimate microstructure presented in each section of the HAZ is dependent on the temperature to which it is subjected and the rate at which that area is cooled. In this regard, phase and Continuous Cooling Transformation diagrams (CCT) can be used to improve the understanding of these microstructures, as shown in Figure 20.

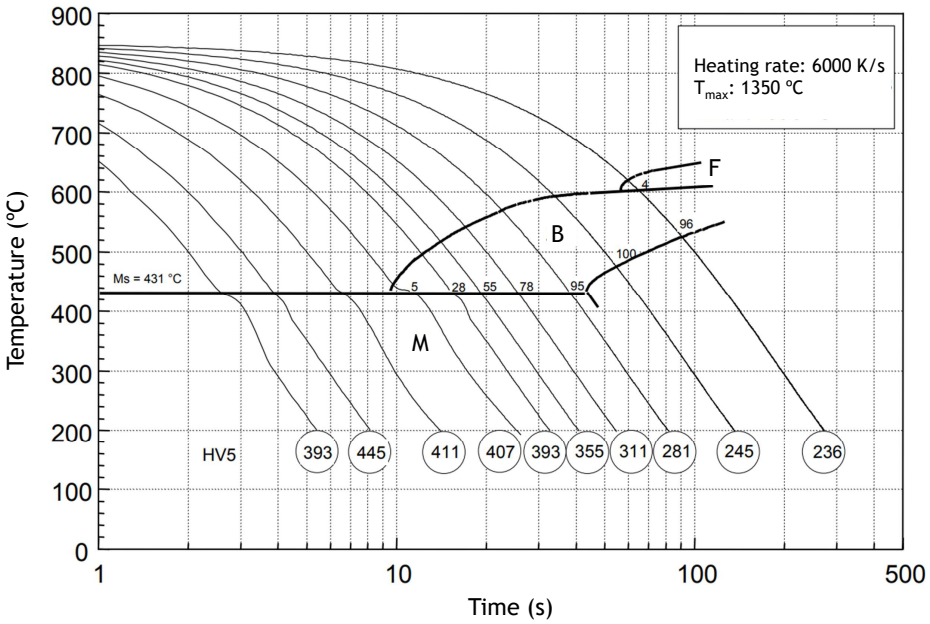


Figure 20: CCT diagram for S690QL steel, adapted from [59].

It is important to note that the following figures correspond to the CCT diagram. The thermal input from the welding process has the capacity to drastically increase the grain size of the area adjacent to the melted zone [60]. The microstructure from this area (Figure 21) corresponds to a coarse-grain tempered martensite. The larger size of this microstructure is due to the high temperatures that this area reached, and the presence of martensite is related to the rapid cooling of this zone. In addition, the thermal cycles from the subsequent multipass process can temper the pre-formed martensite, increasing toughness and substantially decreasing hardness values, as it will be seen further.

Figure 22 depicts a HAZ area that reached lower temperatures and slower cooling rates than the previous one due to the greater distance from the weld material. Regarding these param-

eters, the type of microstructure may be the same, but with significantly smaller grain size, improving mechanical characteristics, as shown in the CCT diagram. It is important to note that these areas may contain trace amounts of bainite [60].

As the zone moves away from the fusion area, a different microstructure emerges, with small constituents beginning to appear in the grain boundaries, as presented in Figure 23. The correct interpretation of the CCT diagram reveals a possible tempered martensitic-bainitic structure, with the new constituent correlated to the ferrite phase, as a result of even lower cooling rates imposed. However, in order to draw more comprehensive conclusions, it is imperative to conduct supplementary microhardness tests, as shown in Section 4.3.2.

The microstructure of the S690QL steel in the base metal area (Figure 24) is composed of tempered martensite and bainite, which is the reason why this material is used in large-scale structures, due to its excellent combined mechanical properties.

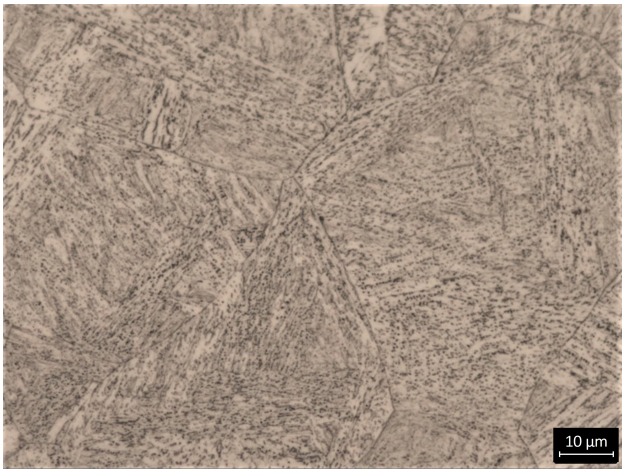


Figure 21: HAZ close to the fusion zone.

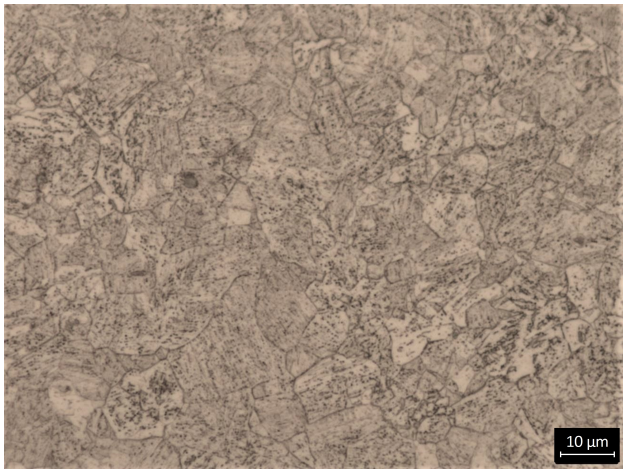


Figure 22: Intermediate HAZ.

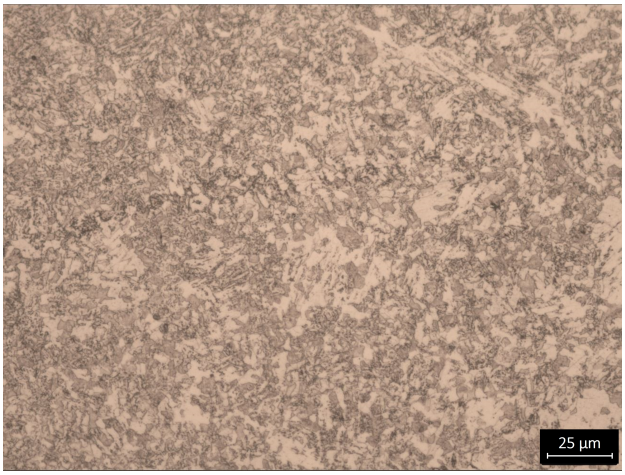


Figure 23: HAZ farther of the FZ.

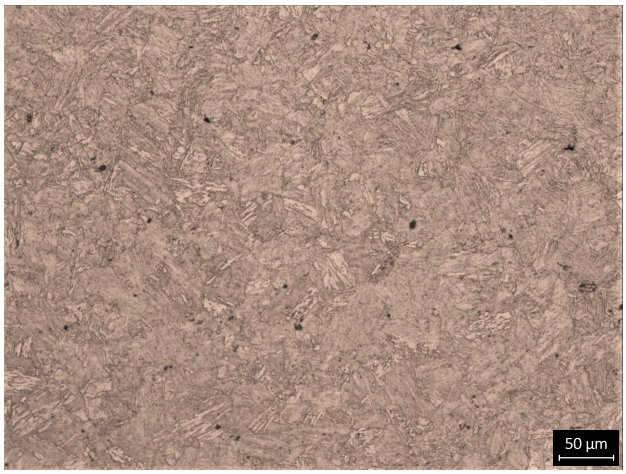


Figure 24: Base material.

The difference in grain morphology and size across the heat-affected zone will have a direct impact on the fatigue performance of this steel section. The heat-affected zone benefits greatly from a fine-grained morphology. The material becomes harder, increasing its resistance to wear and deformation in the first place. Additionally, a fine-grained structure with more grain boundaries is essential for enhancing the fatigue performance of the steel. These grain boundaries act as barriers or thresholds that prevent cracks from spreading, thereby reducing the likelihood of failure. On the other hand, the fatigue performance of the steel might be adversely affected by larger grain sizes and coarser morphologies in the heat-affected zone. Cracks can spread more readily when there are fewer grain boundaries to prevent it, which reduces fatigue life and raises failure susceptibility.

Since the weld material will also be submitted to fatigue testing and has different mechanical properties and chemical composition as-received than the base material, it is critical to analyse the final microstructure after the welding process. Figures 25 and 26 depict a microstructural analyses of this distinctive area.

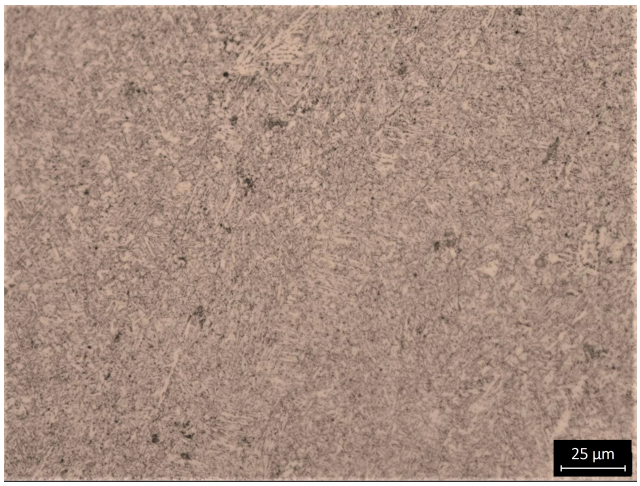


Figure 25: Microstructure of the weld material at 50x magnification.



Figure 26: Microstructure of the weld material at 100x magnification.

The weld material underwent a liquid-to-solid transition due to the high temperatures reached in the arc weld, while the rest of the material registered solid-state transformations. The cooling rates in this section are the fastest of all, resulting in a fine-grain martensitic structure, as it is possible to observe in Figure 26. It is anticipated that the weld material zone will exhibit slightly superior resistance and hardness characteristics when compared to the base material due to the fine-grain microstructure. However, as will be noticeable from the hardness results, the microstructure undergoes a tempering heat treatment as a result of the subsequent heat input from the posterior processes, which lowers its hardness values.

4.2 SEM/EDS analysis

Welding involves the fusion of two distinct materials with dissimilar compositions. This can lead to the diffusion and redistribution of chemical elements across the interface, which in turn can influence the final microstructure and mechanical properties. To understand this process, it is important to conduct a chemical profile analysis. For this experimental campaign, Scanning Electron Microscopy (SEM) with Energy-Dispersive X-ray Spectroscopy (EDS) was used to generate chemical profiles for C, Mn, and Ni. These were chosen because they are the main elements that differentiate between the base and weld material, as shown in Table 1.

Figure 27 depicts the chemical composition profile for these elements along a 2660 µm straight line, which encompasses both materials. In addition, spot EDS analysis was performed in two different and distant zones, Z1 and Z2, as shown in Figure 27. This will also confirm the composition evolution for each material and compare it with the chemical composition provided of both metals.

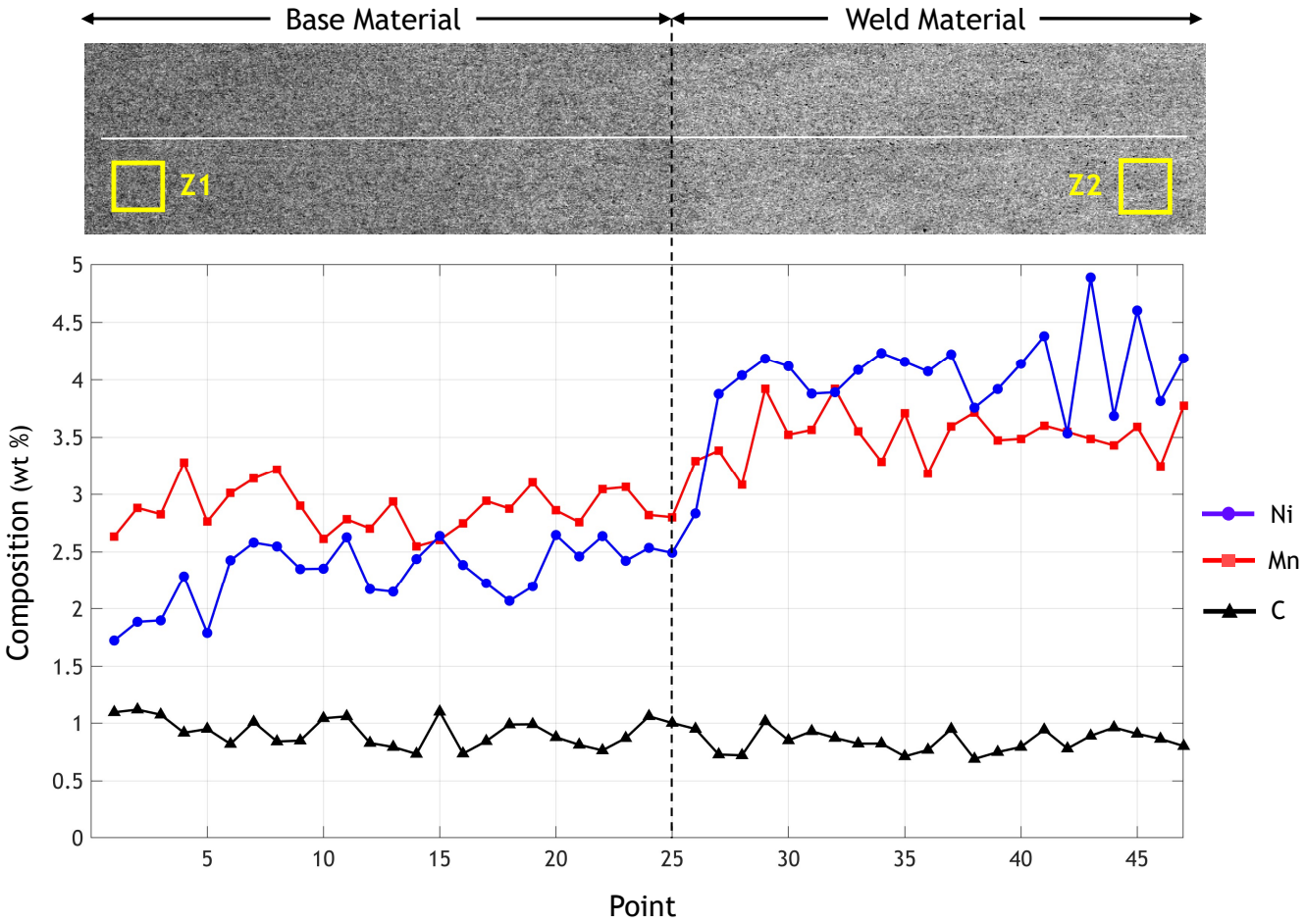


Figure 27: Chemical profile of transition between base and weld material.

Analysing the composition graph reveals that the percentages of manganese (Mn) and nickel (Ni) have the greatest increase in the weld material portion, as expected. This is justified by the greater amount of these elements in the composition of the filler material used. However, according to the chemical composition table (Table 1), the percentage of Ni in the base material is almost non-existent and significantly different from these results, as it is for the Mn content. It is possible to conclude that the results of this analysis are significantly higher than the values presented in the chemical composition table. This can be attributed to some form of EDS equipment inaccuracy during the profile analysis, as there is usually some type of error associated with surface contamination, sensitivity, and calibration [61]. These elements analysed will improve the steel's mechanical properties, since nickel is responsible for ductility improvement, while also increasing its hardenability. This is one of the reasons why martensite dominates the microstructure morphology. Manganese tends to increase strength and decrease ductility, while nickel increases ductility and the notch toughness of this material [62].

The carbon content, on the other hand, begins to decrease slightly during the transition to the fusion zone. This is also to be expected given that Coreweld 69 LT contains a lower percentage of this element in its chemical composition. It is important to note that scanning electron microscopy analysis of carbon is challenging, as carbon can easily contaminate the sample surface. This makes it difficult to distinguish between carbon that is present in the sample and carbon that has been introduced as a contaminant. As a result, SEM-based measurements of carbon content should be interpreted with caution [63, 64].

To address the previous chemical composition profile, two distinct zones for each material section were subjected to EDS analysis, as shown in Table 5.

Table 5: Chemical composition of each zone by EDS analysis.

	Chemical Composition (% wt)				
Zone	C	Cr	Mn	Ni	Fe
Z1	0.76	0.63	1.61	0.25	96.79
Z2	0.62	0.25	2.03	2.18	94.92

A comparison of the chemical composition in this study to that in Table 1 shows that the percentages of nickel and manganese have increased significantly, while the concentration of carbon has decreased markedly. This remarkable transformation is in accordance with and is clearly evident in the meticulous examination of the chemical profile.

4.3 Hardness test analysis

4.3.1 High force Vickers hardness test

The goal of this experiment is to determine how the heat input of the final steps affects the first ones in terms of tempering heat treatment. Tempering typically reduces hardness values, so macrohardness tests will provide a better understanding of this mechanical property evolution. This is also a crucial stage in process quality control, as heat input can influence the microstructure and mechanical properties to the point where the weld becomes unusable for industrial applications. ISO 15608:2017 is a standard that provides guidelines for the selection and qualification of welding procedures for metallic materials [65]. According to this standard, S690QL steel belongs to the 3.2 group, which means that it requires a high level of testing and inspection to ensure its quality and safety. It has a maximum hardness value of 450 HV10 according to ISO 15614-1:2017 [66], which means that it is resistant to wear and tear and can withstand high levels of stress and pressure. However, it is important to note that proper welding procedures must be followed to ensure the integrity of the material and prevent any potential defects or failures.

As previously indicated, two affiliations, A and B, were respectively carried out near the top and root portions of the M30 and M60 welded plates with and without a complete operation. Affiliation B is expected to have the greatest disparity of results between the complete and incomplete procedures. The M30 plate Vickers hardness tests performed for the root procedure and the fully welded one are respectively depicted in Figures 28 and 29.

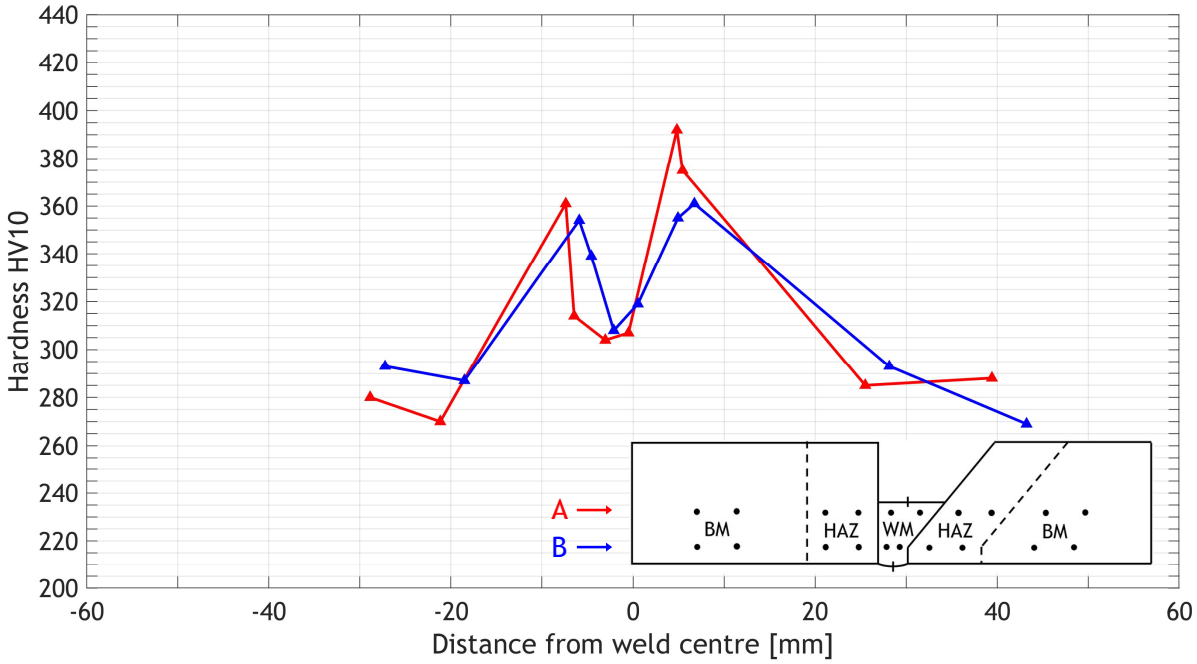


Figure 28: Vickers hardness profile for M30 plate with root steps.

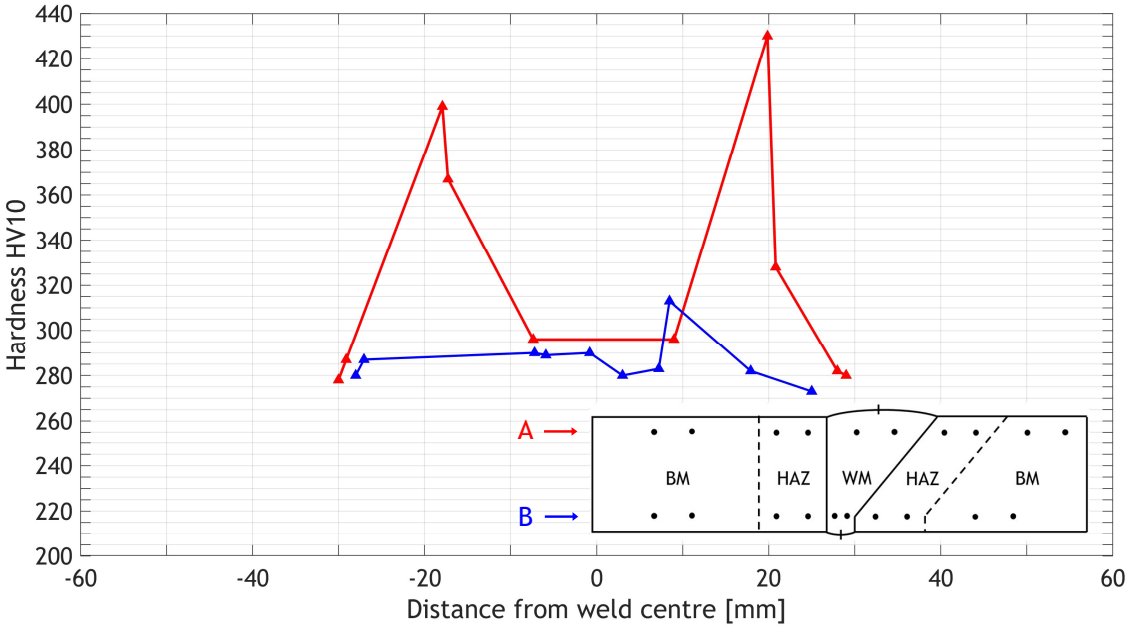


Figure 29: Vickers hardness profile for M30 plate fully welded.

Both graphs, which display the hardness profile for each procedure, make clear that there are significant differences between them, meaning that multipass welding technologies directly impact the mechanical properties.

The evolution of the hardness profile for the method that only considers the initial steps is nearly identical for affiliations A and B, indicating that the heat input of the steps from section A was insufficient to temper and gradually lower the hardness values of section B. For these parameters, the HAZ had the most significant values, but it also had the biggest data discrepancy, indicating an irregular cooling coefficient along the HAZ. This discrepancy is also supported by the previous microstructural characterization, which reveals a wide variety of morphologies and constituents in the HAZ. In both affiliations, the hardness is higher in the WM zone than in the base material, as expected. Despite the fact that the chemical composition of both materials is identical, the cooling rate is faster in the melted zone, resulting in a fine-grained microstructure, which implies that hardness values may be higher.

The changes that have occurred can be confirmed by performing the final steps in the complete procedure of the M30 plate, as shown in Figure 29. The values in the Affiliation B range show less variation and a straight-line behaviour, indicating that the heat input from the last steps directly influenced the mechanical properties of the root ones. The thermal exposure from the top steps is sufficient to provide a tempering heat treatment for the B steps, significantly lowering the hardness values. The process parameters for the last steps are slightly different from the previous ones (Table 2) in order to reduce the likelihood of the development of high-hardness martensite, as there was no post-heat treatment.

As previously mentioned, Vickers hardness tests were also performed for the M60 plate to confirm the tempering effect, as illustrated in the graphs presented in Figures 30 and 31.

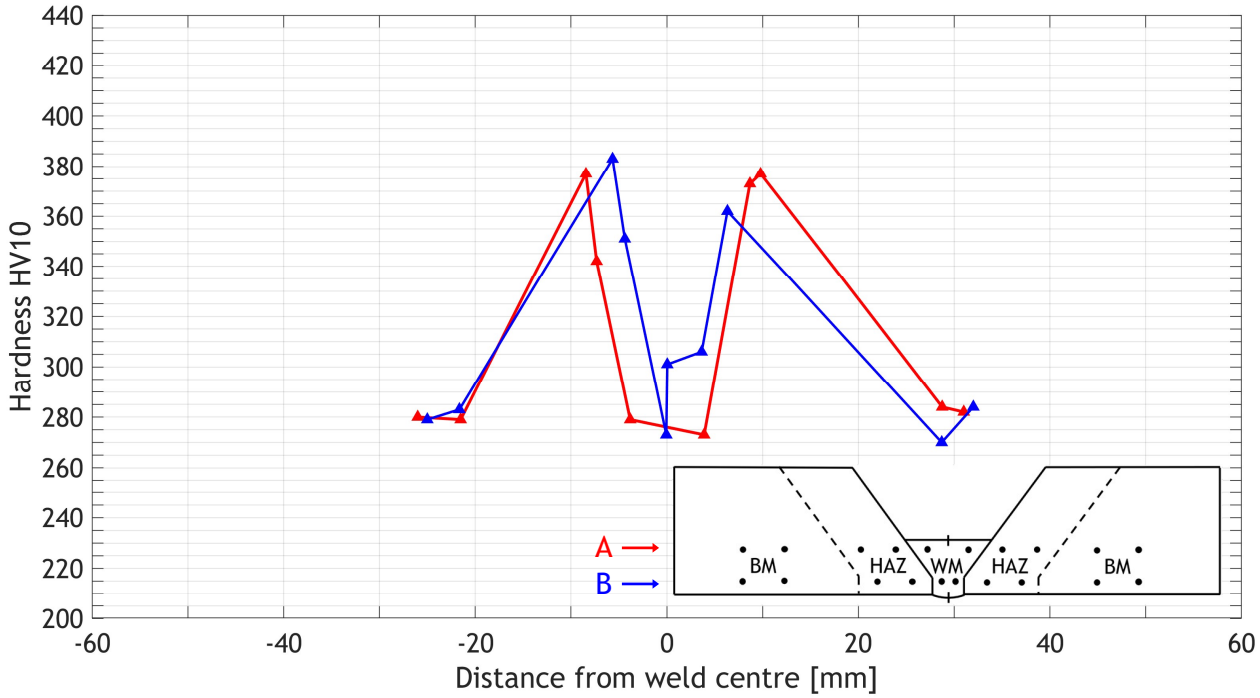


Figure 30: Vickers hardness profile for M60 plate with root steps.

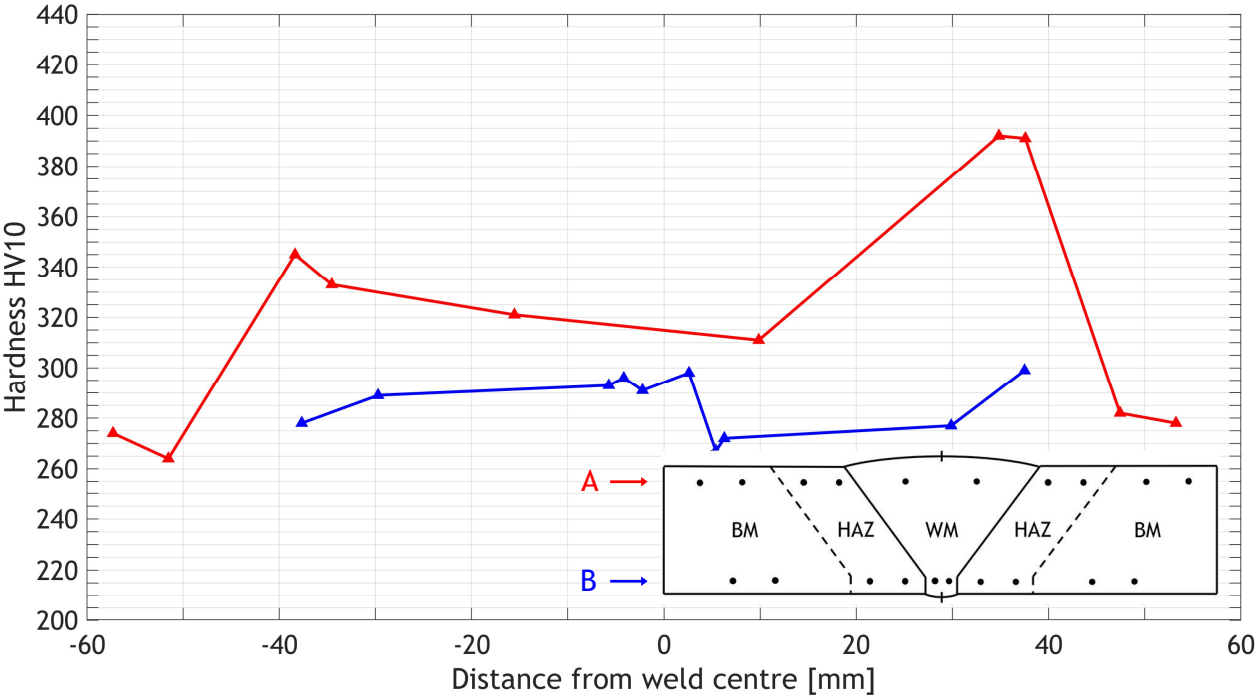


Figure 31: Vickers hardness profile for M60 plate fully welded.

Based on the analysis of these graphs, it is possible to confirm that the same effect occurred, indicating that the temperature reached and the cooling rate are sufficient to gradually decrease the hardness values of the first steps. In the incomplete procedure, M60's affiliation A and B describe the same evolution along a straight line through the welded joint cross-section as the root steps procedure for the M30 plate (Figure 28).

The hardness profiles showed distinct differences between the root and fully welded steps. The fully welded steps showed higher hardness values than the root steps, suggesting that the additional heat input during the final steps may have had the same previous tempering effect. This finding suggests that the microstructure and mechanical characteristics of the root region are influenced by the heat input during the later steps. The final steps can produce a tempering effect that can significantly affect how the welded joint behaves mechanically. For the fully welded M60 plate, it is possible that the root area underwent a localized heat treatment to increase the toughness and lessen susceptibility to cracking, as evidenced by the increased hardness in the fully welded steps. Figures 32 and 33 give a better understanding of how the heat input decreases the hardness between the two procedures for affiliation B.

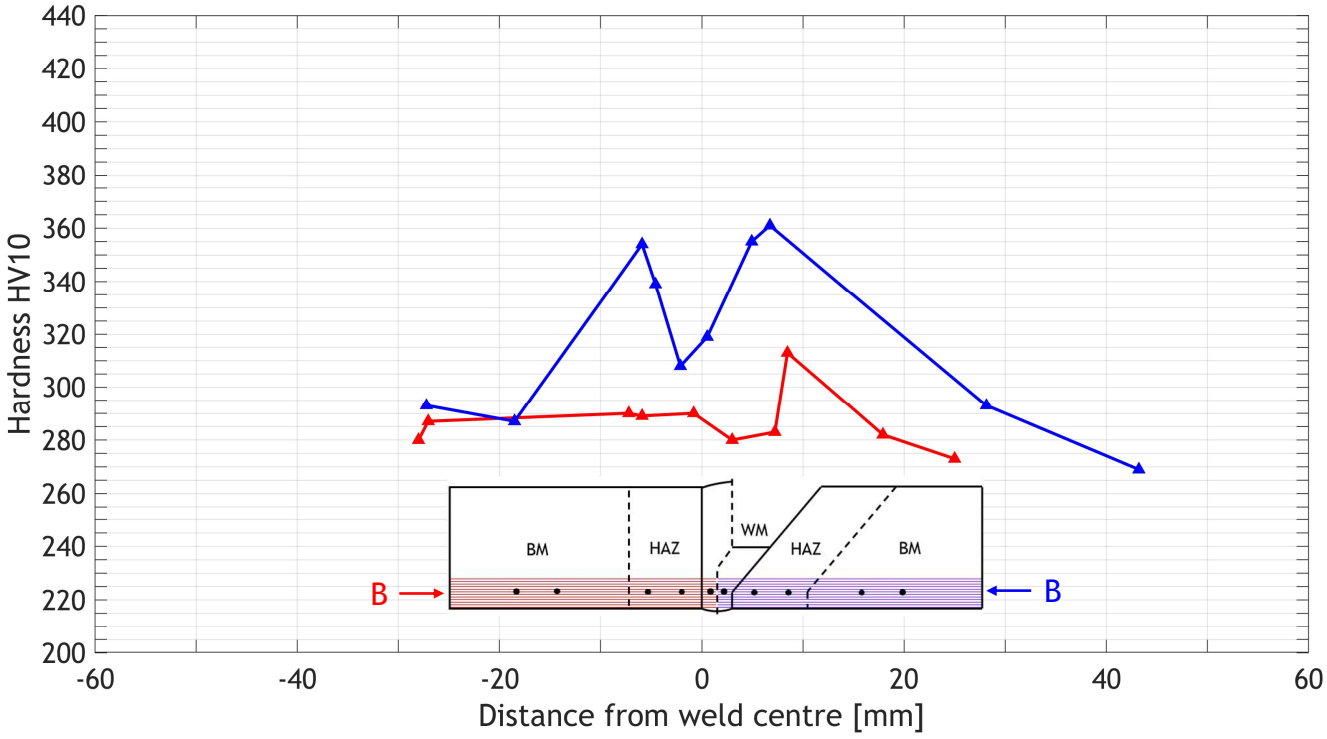


Figure 32: Affiliation B comparison between the two procedures for the M30 plate.

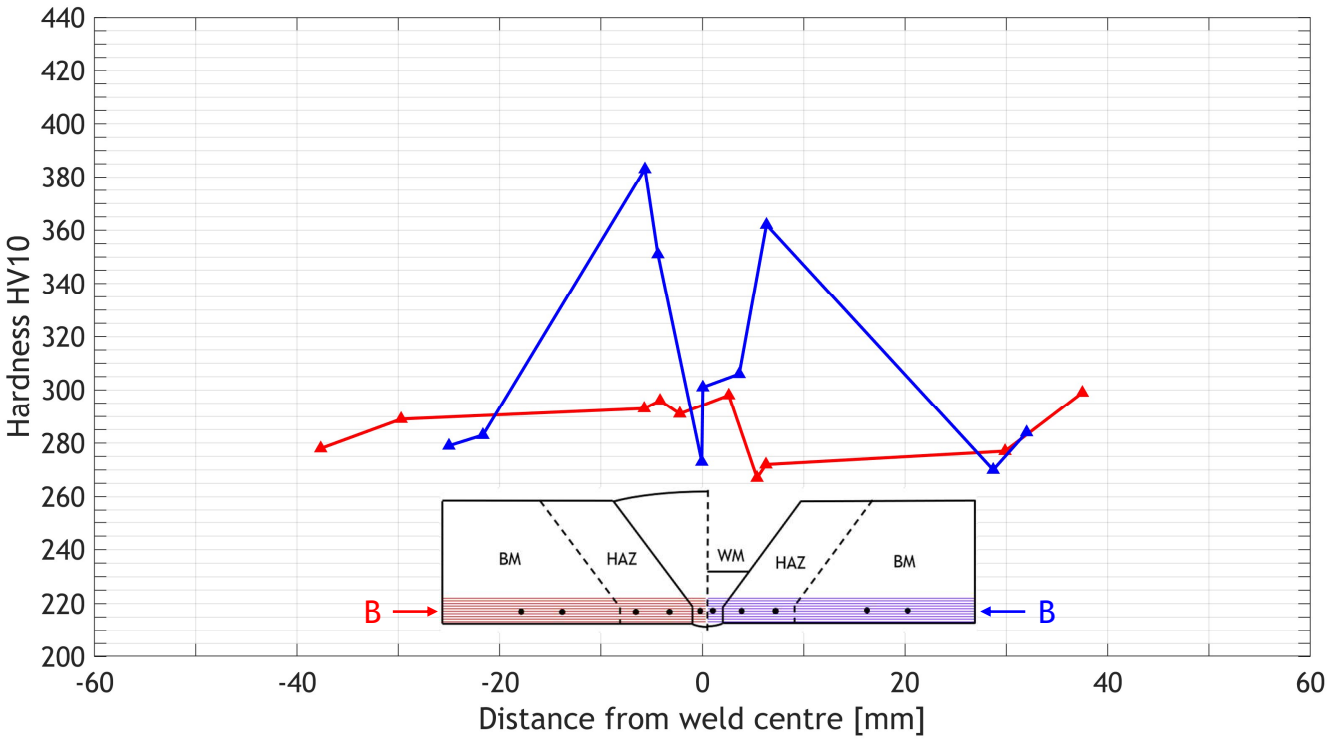


Figure 33: Affiliation B comparison between the two procedures for the M60 plate.

As expected, the hardness values varied widely throughout the welded joint however, not a single value exceeded the 450 HV10 threshold set by ISO 15614-1:2017. This confirms the accuracy of the parameters and the quality of each welded connection, making it suitable for industrial applications. The highest value obtained was 430 HV10 for the HAZ, indicating that this region may be more prone to brittle fracture. The base material (BM) region's average hardness value, 282 ± 8 HV10, was more consistent throughout all measurements because it was unaffected by temperature fluctuations.

Furthermore, due to the greater thickness of the M60 plate, some HAZ hardness values are lower than those of the M30 plate. Thicker materials typically cool more slowly than thinner ones due to their higher thermal dissipation. Slower cooling rates can lead to larger grain sizes and possibly lower hardness values. On the other hand, thinner materials cool more rapidly, resulting in finer grain structures and perhaps higher hardness values.

4.3.2 Low force Vickers hardness test

A complementary low-force hardness test was carried out on a micro-scale to more precisely identify the constituents and each sub-zone of the HAZ. This section of the welded joint has a high degree of irregularity in morphologies and subsequent mechanical properties since the temperatures reached and cooling rates decrease as one moves away from the transition section of the fusion zone. Figure 34 is a schematic representation of these sub-zones, which corroborates with the Optical Microscopy previously performed.

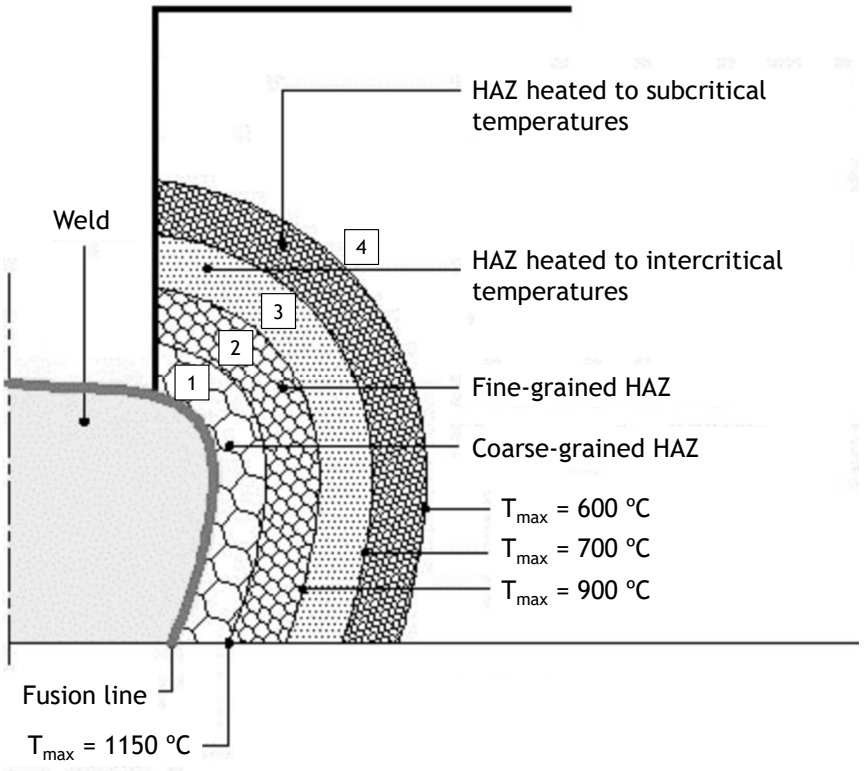


Figure 34: Schematic representation of welding process HAZ regions of an HSLA steel, adapted from [67].

The previous macrohardness profile was unable to identify the individual sub-zones of the HAZ, so a micro-scale hardness evaluation was performed.

This allowed for more precise indentation in each sub-zone, which will reveal if the small fraction of the previously unknown constituent present in the HAZ heated to intercritical temperatures (between Ac_1 and Ac_3) is whether or not actually made up of a ferritic phase, as depicted in the CCT diagram (Figure 20). Also, the difference between coarse and fine-grained martensite will be mechanically studied, as this morphology will directly impact the hardness values. It is expected that the hardness increases with more refined grain size. The microhardness tests performed across the sub-zones are presented in Figure 35.

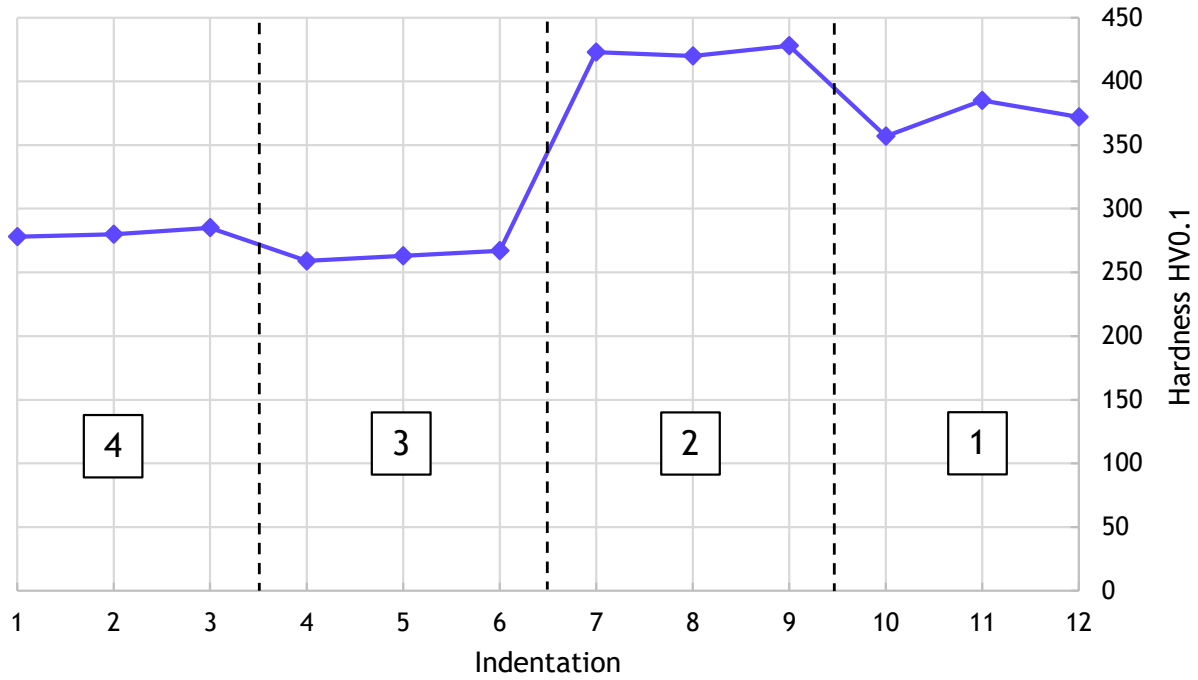


Figure 35: Hardness distribution across each HAZ sub-zone.

The morphology and grain size have a significant impact on hardness, as shown in the previous graph. The hardness values of martensite with a coarser grain size (Zone 1) are clearly decreased when compared to the same type of constituent but with a slightly finer grain size (Zone 2). As we move away from the fusion line, a different type of morphology appears as indicated in Figure 23 in the Optical Microscopy (OM) analyses. This test allows us to finally conclude that the new constituent that emerges in the grain boundaries is composed of a ferritic phase, as its hardness values are much lower than those of the base material.

Ferrite in the grain boundaries can act as a weak region within the microstructure. In comparison to martensite and bainite, ferrite is softer. As a result of this softness, localized stress concentrations can arise at grain boundaries, making them more prone to crack initiation. Furthermore, the mechanical properties difference between the ferritic phase and the surrounding martensitic/bainitic matrix can cause stress concentration and crack propagation along grain boundaries. Under cyclic loading conditions, this can significantly reduce fatigue life and increase the likelihood of failure of the S690QL steel component [68].

The base material values are consistent with the macrohardness test results previously conducted. This is still another indication that this region of the welded joint is composed of a tempered martensite-bainite matrix, as its hardness is significantly lower than that of the HAZ.

4.4 Rotating bending fatigue results

4.4.1 S690QL M30 welded plate

The major goal of this research was to examine the fatigue performance of S690QL welded plates with 30 mm (M30) and 60 mm (M60) in thickness, with a particular emphasis on the base material, heat-affected zone, and weld material. The process includes rotational bending fatigue testing specimens from each zone. To represent the Wöhler's curve, a table was produced for each section containing data on the stress range and cycle count leading to failure for each specimen. These tables are presented in Appendix C for the M30 plate sections and in Appendix D for the specimens tested from the M60 plate. Due to practical constraints, the number of specimens tested varied. For the base material, in the case of the M30 plate, a greater number of specimens were practically available, allowing the creation of an S-N curve. However, the HAZ and weld material's stress amplitudes and failure cycles were measured without creating S-N curves, being only introduced as single points and directly compared with the base material´s curve.

Figure 36 represents the S-N curve plotted with experimental data obtained just from the base material specimens of sections A and B of the M30 plate.

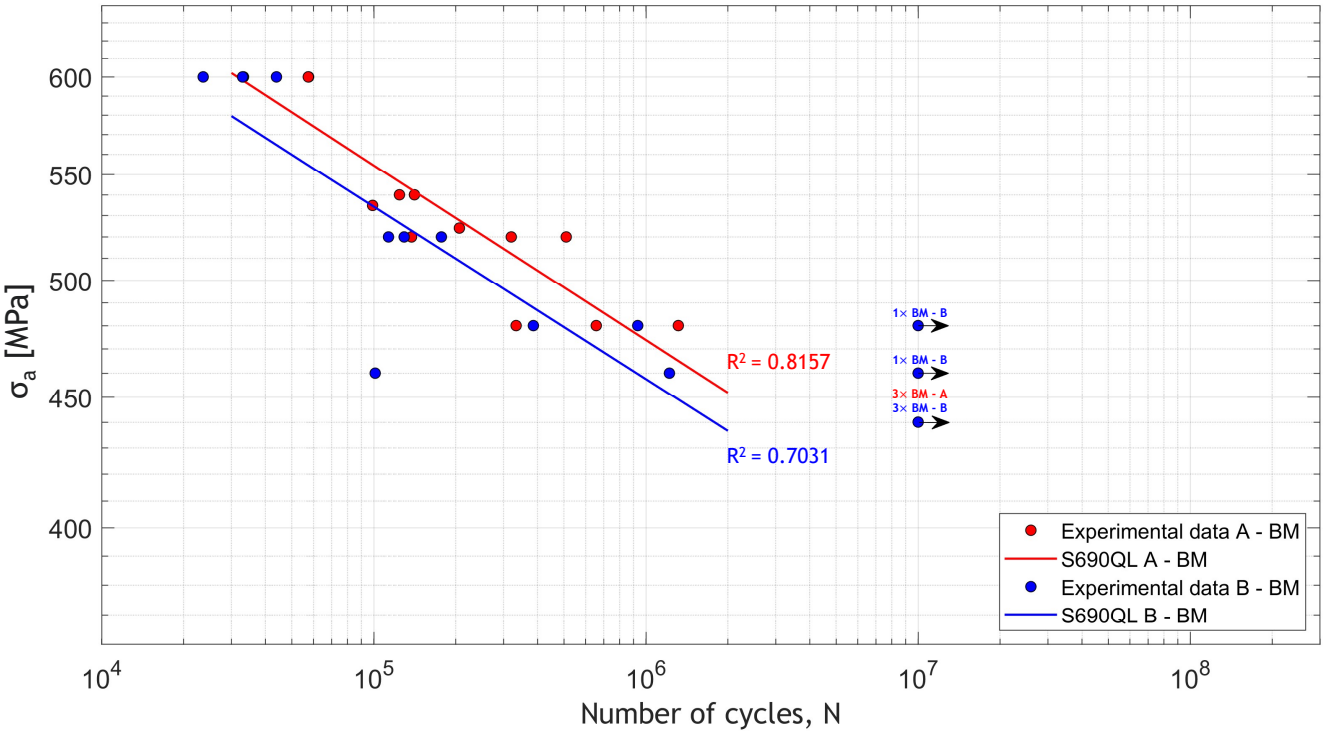


Figure 36: S-N curves of S690QL steel base material for sections A and B of the M30 plate.

The results are quite accurate and consistent when testing the specimens in a low-cycle fatigue regime (LCF) for both sections however, due to the nature of the test, the results are

more variable when testing the specimens in a high-cycle fatigue regime (HCF). This is because, in HCF, the failure mechanism is progressive, where the accumulation of damage is slow and happens over a large number of cycles. This behaviour can cause a significant discrepancy in results compared to LCF regime results, where failure is often controlled by processes such as plastic deformation, yielding, or fracture propagation that take place over a relatively small number of cycles. Additionally, because of how sensitive to imperfections in the material this type of test is, fatigue scatter is more pronounced when there are more cycles involved. As already mentioned, the HCF mechanism happens as an elastic event on a macro scale, and any imperfections in the material can have an adverse amplified effect on the fatigue life. In LCF, however, macroscopic plastic deformation occurs in every cycle, which tends to mask the effects of imperfections. For example, for a stress of 460 MPa (HCF), two specimens fractured upon two distinct numbers of cycles, while one reached the fatigue endurance limit of 1×10^7 cycles. This was for a section of the welded joint that was not subjected to any thermal treatment during the welding process.

The S-N curves of the base material specimens for sections A and B are represented in Figures 37 and 38, along with the respective experimental data of each HAZ and WM specimens. For section A, some heat-affected zone and weld material specimens that exceeded the fatigue endurance limit were subjected to a second fatigue test at higher stress amplitudes, as shown in Table 8, due to the restricted quantity of specimens at the time. Also, due to the limited number of specimens, no S-N curves were plotted for the WM and HAZ specimens.

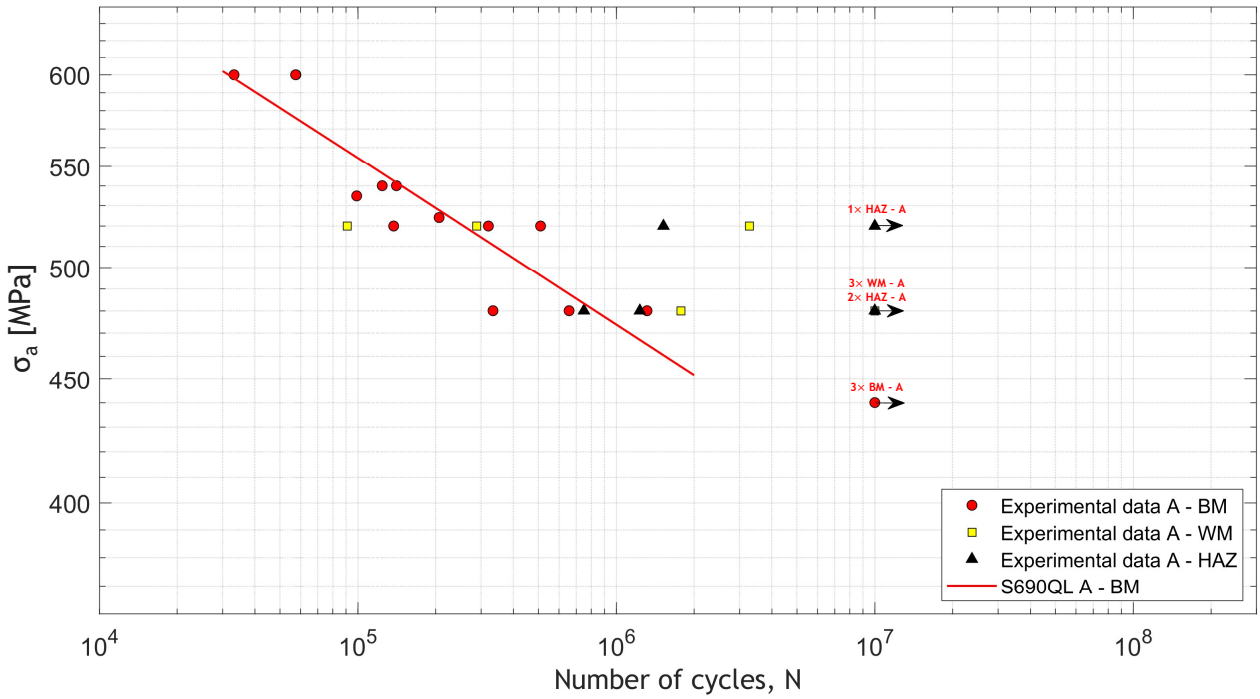


Figure 37: S-N curves of S690QL steel welded joint for section A of the M30 plate.

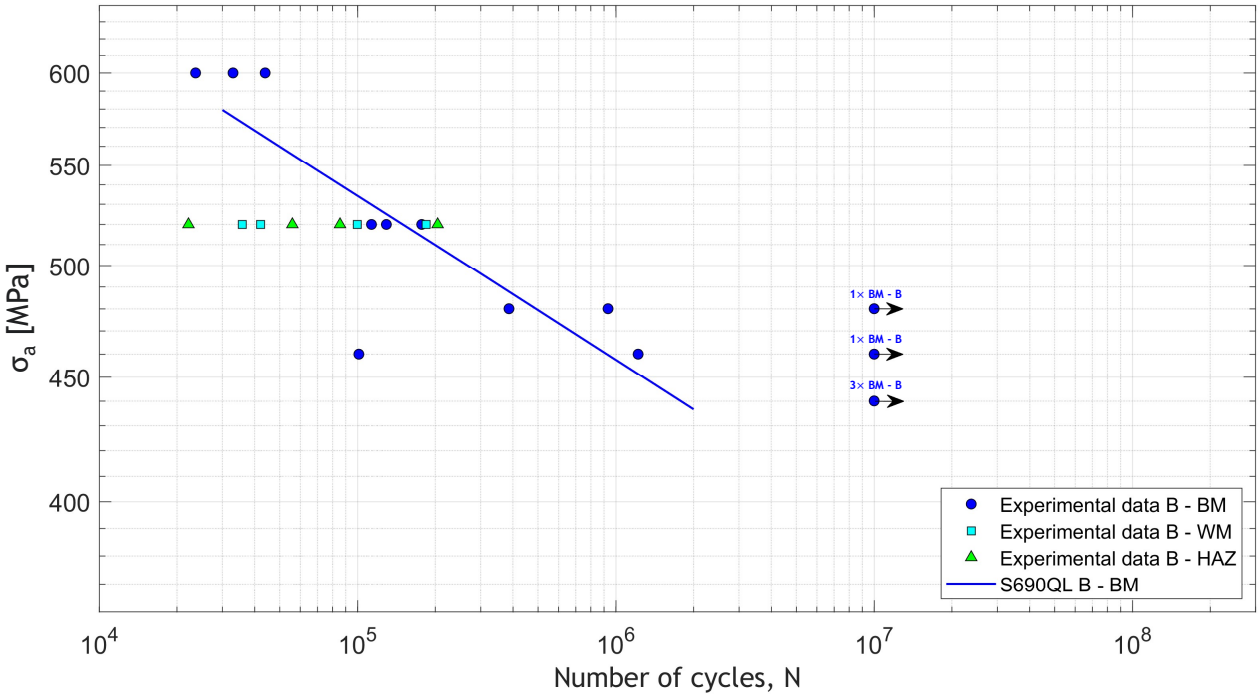


Figure 38: S-N curves of S690QL steel welded joint for section B of the M30 plate.

The study of these curves reveals that the heat-affected zone and weld material specimens exhibit markedly different behaviour than the base material (BM). This behaviour also changes between the specimens in the top section A and the bottom section B, as previously determined for the other mechanical properties. It is important to note that, since the stress of 480 MPa was near the fatigue limit in section A, for section B all specimens of WM and HAZ were tested for 520 MPa.

For the section A fatigue results, the HAZ and WM exhibit greater fatigue resistance. This is supported by the mechanical properties inherent to the material and welding technique previously evaluated. Both of these subzones exhibit significantly higher hardness values than the base material (Figure 29), reflected in an increase in fatigue resistance. For example, for the 520 MPa stress level, two HAZ and three WM specimens demonstrated higher fatigue resistance behaviours, with some even reaching the fatigue endurance limit, whereas BM specimens failed after a lower number of cycles. This means that the increase in hardness actually retarded the fatigue crack initiation stage at some point. There are a few explanations why the WM specimens proved to be more fatigue resistant than the BM. According to Table 1, the filler material used in the welding process exhibits a lower carbon content and a greater nickel percentage than the BM, implying that ductility is improved. Ductility refers to a material's ability to undergo plastic deformation and absorb more energy before fracture, allowing it to more effectively disperse stress and resist crack propagation. Furthermore, the WM section exhibits slightly higher hardness values than the BM, as shown in Figure 29 for

affiliation A, since it is being discussed the WM fatigue specimens from the top section. This will be reflected in higher resistance in fatigue crack initiation.

On the other hand, the heat input from section A has caused the lowering in hardness values for the WM and HAZ of section B, as presented in Figure 29. This might explain why section B's values indicated lower fatigue resistance than those in the top section. For example, at 520 MPa, three HAZ and two WM specimens failed after fewer cycles than the BM specimens.

Scatter in the results for these welded joint subzones is also visible, attributed to reasons similar to the scatter in the BM. In addition, the microstructural heterogeneity in the HAZ, characterized by different grain sizes and morphologies, contributes to this scatter. Smaller grain sizes improve fatigue resistance by providing more grain boundaries as barriers to crack initiation, while coarser grain sizes facilitate crack initiation through the grain [11].

4.4.2 S690QL M60 welded plate

Three distinct sections — C, D, and E — were evaluated for the M60 plate due to the weld's greater thickness. However, for sections D and E, only specimens for the HAZ and WM were evaluated and the results were directly compared with the experimental data of section C. Figure 39 depicts the BM data C and the results for WM and HAZ for section C.

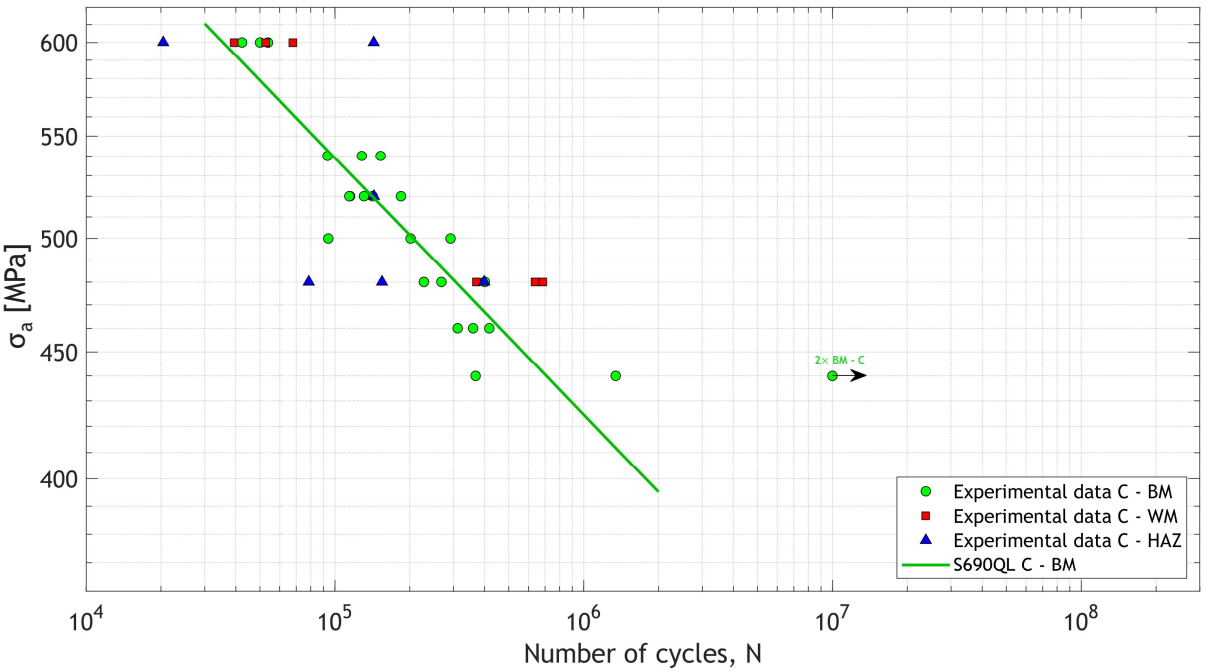


Figure 39: S-N curves of the S690QL steel welded joint for section C of the M60 plate.

The analysis of this graph confirms that the BM specimens exhibit less scatter when compared with the M30 specimens results. This is true for both the high-cycle fatigue regime and the

low-cycle fatigue regime. However, the scatter is less pronounced in the LCF regime, where the specimens fracture after only a few cycles of difference.

As previously observed, the HAZ and WM have different fatigue performances than the BM. This is true for both the HCF and LCF regimes. The HAZ has significantly reduced fatigue resistance, with many specimens fracturing after fewer cycles than the BM zone for the same stress amplitudes, even for the LCF regime. However, some HAZ specimens had higher fatigue resistance. This is likely due to the different mechanical properties and microstructure morphologies in the HAZ. Overall, the WM specimens fractured after a higher number of cycles than the BM and HAZ specimens. This corroborates the conclusions made for the M30 plate in the previous discussion.

Figure 40 shows a graphical representation of the BM curve of section C as well as the WM and HAZ curves generated from experimental data of all sections (C, D, and E). This allows for a direct comparison of the fatigue performance of the BM, HAZ, and WM zones. This information can be used to understand the cyclic loading and failure capacities of the welded joint. Comparing the three zones can also help to improve welded joint integrity by identifying areas where fatigue resistance can be improved through design and material manufacturing adjustments.

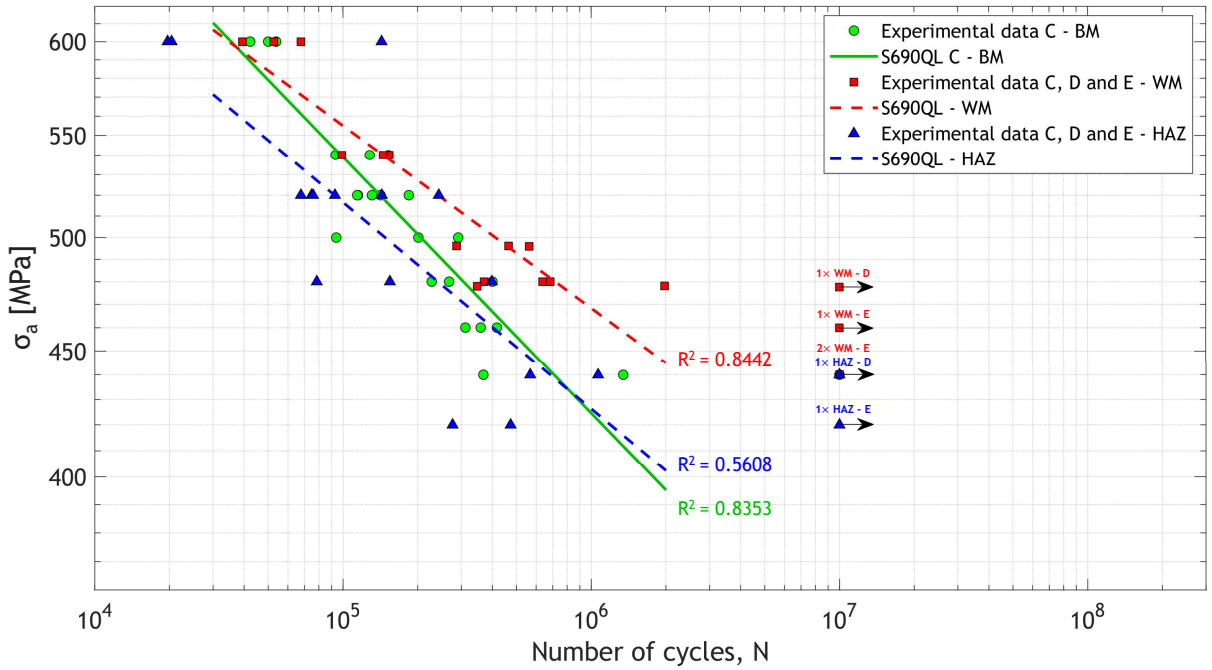


Figure 40: S-N curves of the M60 welded joint for sections C, D, and E from all zones.

The fatigue resistance of the welded joint can be understood by comparing the curves from the experimental data of all three distinct regions. In the low-cycle fatigue regime, the WM curve is not very different from the BM curve, since the specimens of these two regions fractured

for a similar number of cycles at 600 MPa. However, as the stress range decreases, the two curves evolve in quite different ways, with the WM curve describing greater fatigue resistance until the considered run-out results. The higher fatigue resistance of the WM in the LCF and intermediate-cycle regimes is attributable to ductility, which is the most essential factor because this regime is governed by plastic deformation. The Coreweld 69 LT H4 filler material has a 20% elongation before fracture, compared to 14% for the S690QL base material. These parameters provided by the material supplier confirm that ductility does indeed influence the fatigue performance of this region for these regimes. For HCF, hardness becomes the predominant variable and, from the previous test assessment (Figure 31), the WM presents higher hardness values compared to the BM area, justifying the greater fatigue behaviour of the WM for lower stress amplitudes. Overall, the HAZ curve describes the lowest fatigue performance due to the heterogeneous nature of this region, as previously stated. From the three subzones studied from the HAZ, two of them are most likely to reduce the fatigue life of this material´s welded joint. The HAZ microstructure near the fusion zone revealed coarser grain sizes that drastically decrease fatigue life due to the reduced density of grain boundaries. On the other hand, a region of the HAZ near the BM is composed of ferrite in a bainitic-martensitic matrix, leading to variations in the localized mechanical properties such as hardness and deformation. The variations in these variables can have an effect on the localized stress distribution and the proclivity for crack initiation.

Figure 41 shows all the S-N curves obtained from both the M30 and M60 plates, as well as a bibliographic S690QL curve corroborating the results obtained for the base material [21].

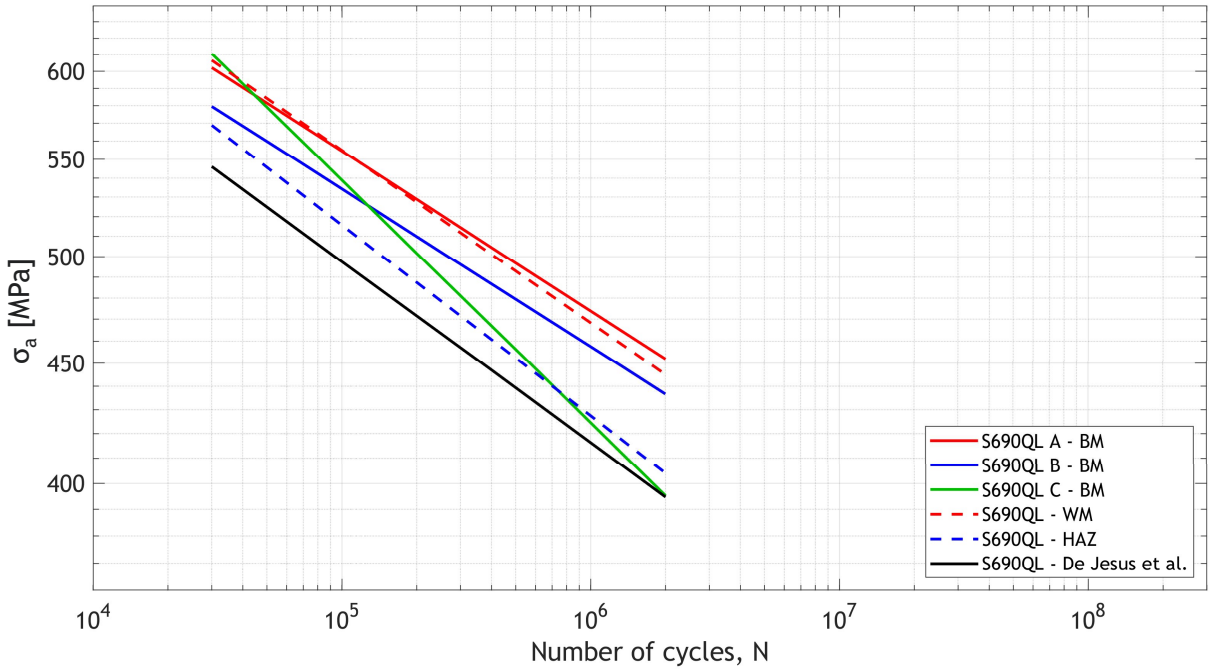


Figure 41: S-N curves of M30 and M60 S690QL steel welded joint for all sections.

As expected, the fatigue resistance for the base material's curves of the M30 plate (sections A and B) shows a very similar evolution due to the reduced plate thickness. Sections A and B have approximate fatigue limits of 450 and 440 MPa, respectively, with section B describing a slightly lower fatigue lifespan throughout the low and high cycle regimes.

On the other hand, the BM from section C of the M60 plate described a very different performance compared to the others, especially in the high cycle fatigue regime, where its resistance abruptly decreased to approximately 400 MPa. Table 3 depicts that the yield and tensile strength, as well as elongation, are lower for the M60 plate, indicating that it has an absolute lower toughness, despite being made of the same class of material. A tougher material, under cyclic loading, not only has a higher potential for energy absorption and plastic deformation prior to crack initiation, which lowers stress concentrations and increases resistance to crack initiation and subsequent propagation but also prevents brittle fracture, which can result in an abrupt and catastrophic failure without significant deformation or warning signs [69].

The fatigue properties for ref. [21] were used to plot the mean curve with equation 3. These properties were extrapolated using the fatigue data presented in the literature, in accordance with ISO 12107 [53]. It should be noted that a strain-controlled fatigue test was used to gather these fatigue results. In a strain-controlled fatigue test, the applied strain is held constant while the material is subjected to cyclic loading, causing the stress to change. In contrast, rotating bending fatigue tests subject the material specimen to cyclic loading while maintaining constant stress on it. Due to differences in the loading conditions and specimen geometries employed in the two tests, the fatigue strength coefficient obtained from a strain-controlled fatigue test may differ from that obtained from a rotating bending test. In a tensile fatigue test, the stress distribution is typically uniform and primarily tensile, which increases the likelihood of crack initiation and propagation in the direction of the tensile stress. In a bending fatigue test, the stress distribution in the shortened region of the specimen is typically characterized by a combination of compressive and tensile stresses, as shown in Figure 42. When compared to a bending fatigue test, where the stress distribution combines two types of stresses, the monotonic test can lead to a decrease in fatigue life. However, it is safe to claim that the outcomes of this experimental work are consistent with those in the bibliography.

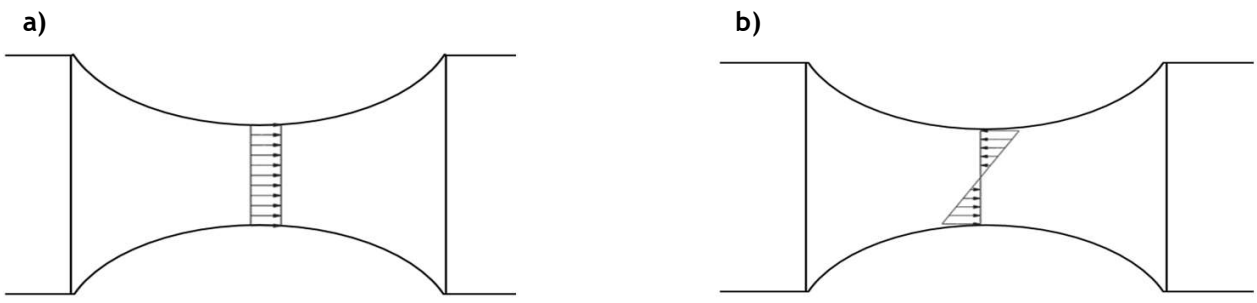


Figure 42: Stress distribution for (a) tensile and (b) rotating bending fatigue test.

For a deeper understanding of the specimens for the heat-affected zone and welding material of both plates, a statistical analysis was performed to understand the fatigue behaviour differences between welding procedures, as presented in Table 6. The mean of the number of cycles for each stress range was directly compared for both procedures, M30 and M60.

Table 6: Variation between the M30 and the M60 plate specimens of the fatigue test.

	M30		M60		M60 x M30
	Stress	Number of cycles	Stress	Number of cycles	Variation
WM	< 460	1.00E+07	< 460	1.00E+07	0%
	480-520	7.94E+06	480-520	1.70E+06	366%
	520-540	5.74E+05	520-540	1.33E+05	332%
	> 540	-	> 540	5.33E+04	-
HAZ	< 460	1.00E+07	< 460	3.77E+06	168%
	480-520	5.50E+06	480-520	2.11E+05	2509%
	520-540	1.98E+06	520-540	1.16E+05	1062%
	> 540	-	> 540	6.11E+04	-

Overall, the M60 plate presents a lower fatigue resistance and behaviour for both HAZ and WM specimens compared to the M30. However, the variation in the fusion zone can be attributed to the scatter inherent to the test itself, since it is very sensitive to any type of defects.

On the other hand, the heat-affected zone reported a much larger decrease from the M30 to the M60 welded connection, reaching a variation of -2509 % and -1062 %. This decrease can be justified by several factors. First, as mentioned before, the general toughness of the M60 plate is lower than the M30 one, which is reflected in a deterioration of the fatigue resistance in both BM and HAZ specimens. Additionally, by directly comparing the hardness values from both fully welded plates (Figures 29 and 31), the M60 shows significantly lower values for the HAZ than the M30. This makes the HAZ of the M60 plate more susceptible to fatigue crack initiation. For example, for a stress level of 460 MPa, the HAZ specimens of the M30 plate reached the fatigue endurance limit, while the M60 ones reached failure for a much lower number of cycles.

Based on this extensive investigation, it is possible to infer with confidence that the thickness of the plate and the number of steps involved in the welding procedure have a substantial impact on the fatigue resistance of critical regions in the plate. The change in the number of steps directly impacts the heat input and thermal dissipation during the procedure. These insights are extremely valuable in the thorough planning of materials and techniques to be used.

4.5 Fractographic analysis

After the fatigue tests, a number of fractured specimens were examined using SEM/EDS analysis to understand and analyse the fatigue fracture formation mechanism. This analysis allowed the identification of nucleation sites, the fatigue region, where fatigue fractures gradually expand cycle by cycle, and the overload area, where the final fracture occurred at the last cycle. Figure 43 shows the fracture surface for the base material, heat-affected zone, and weld material, as well as a close-up image of a typical nucleation site.

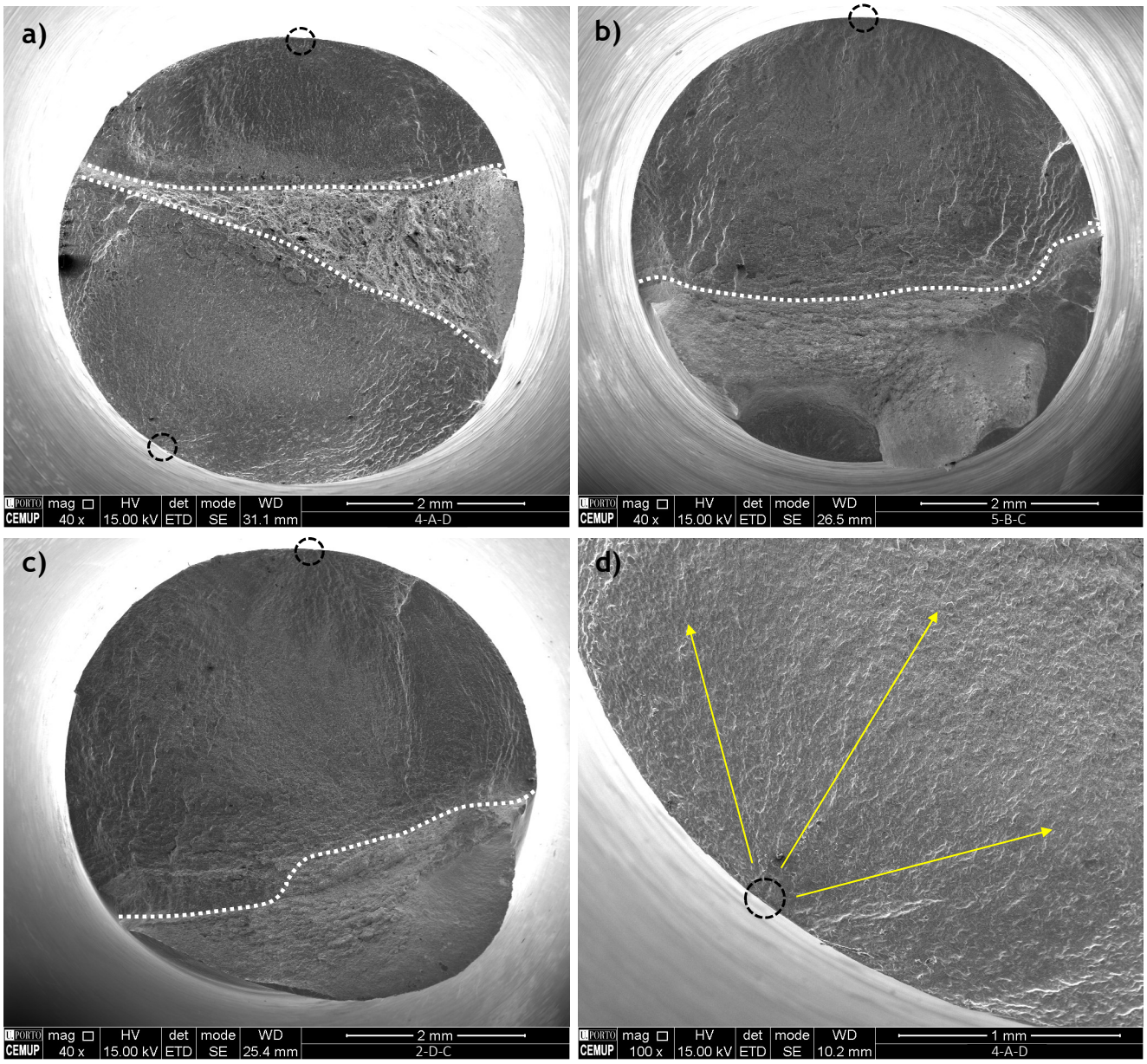


Figure 43: Specimens' fracture surface analysis by SEM: a) base material; b) heat-affected zone; c) weld material; d) close-up of crack nucleation site of a).

The specimens' fracture surfaces obtained by SEM were analysed and it was possible to observe the three main stages of fatigue failure: crack initiation (circle marks); propagation (yellow arrows); and final fracture (white limits). As expected, all the crack initiation sites occurred on the material's surface. This is because nucleation sites tend to be located on the free surfaces of materials, where there is less constraint from surrounding grains, resulting in lower stresses required to initiate crack nucleation. In addition, the alternating tension-compression loading used in this type of test causes microslip bands originating from dislocation movement, which are ideal locations for microcracks to develop.

The number of nucleation sites can vary, and it is possible to correlate the number of sites with the stress employed. Figure 44 shows two fracture surfaces of weld material specimens with very different morphologies, with a significant difference in the number of fatigue crack nucleation sites. According to some authors [70], multiple initiation sites are more common under LCF regimes, in other words, at high-stress levels. For instance, the specimen with a crack initiated by a single site was subjected to a stress of 480 MPa, while the sample with multiple fracture sites was submitted to 540 MPa.

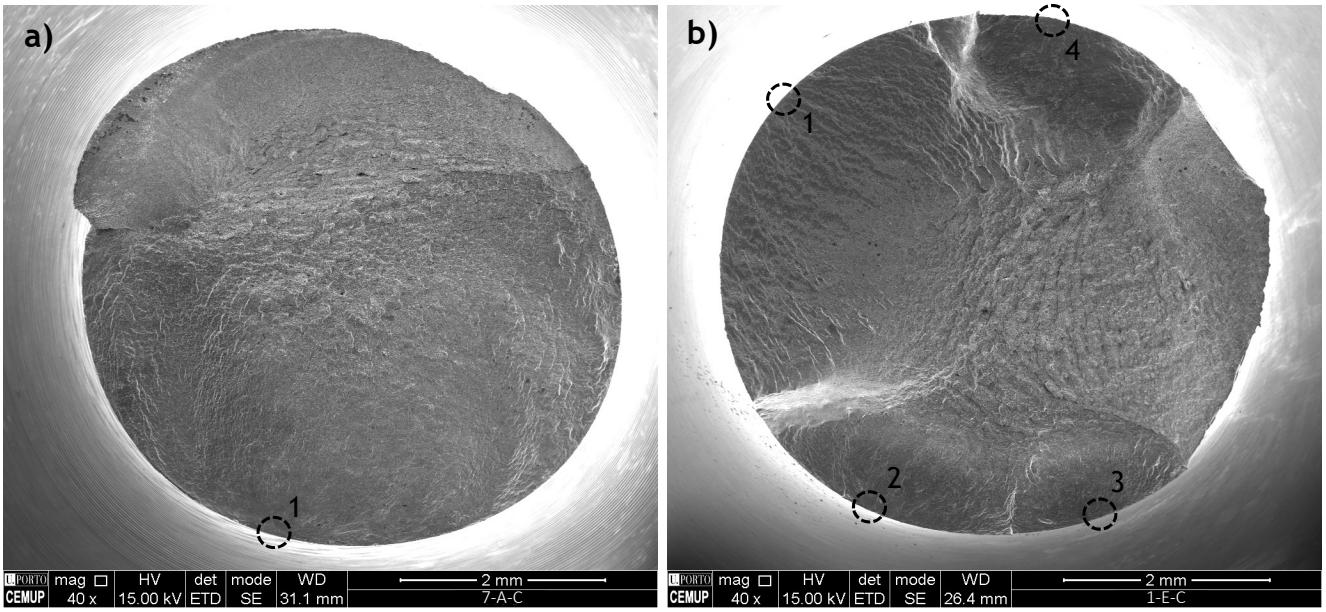


Figure 44: Fracture surface analysis of WM specimens with a) single and b) multiple crack initiation sites.

The crack propagation mechanism can be seen as a radial pattern that diverges from the nucleation site towards the final fracture region, perpendicular to the tension-compression axis. However, the fatigue region can be divided into two separate sections according to its morphology and features. Figure 45 illustrates these two distinct areas of the fatigue region at higher magnifications.

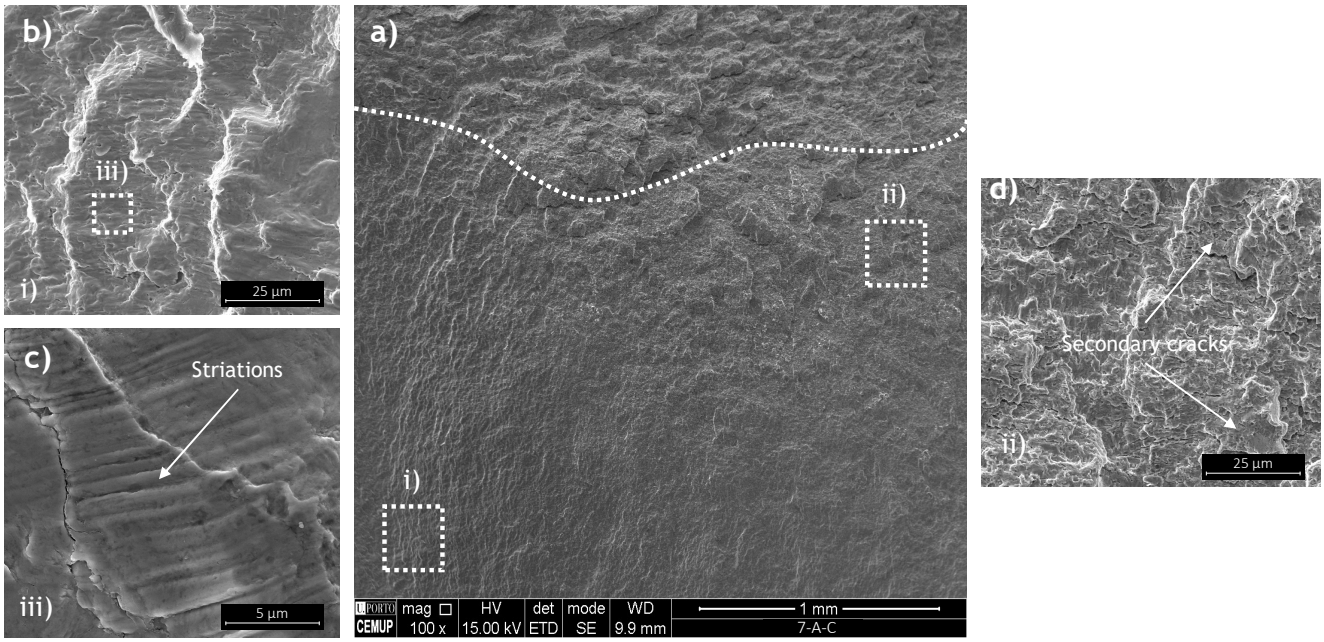


Figure 45: Fracture surface analysis a) WM specimen b) initial propagation fracture surface c) striations d) region immediately prior to the overloaded area.

Under planar deformation, the initial propagation fracture surface (i.) is characterized by a flat and smooth area, typical of stable crack growth, where the crack reaches a macroscopic dimension. At higher magnifications (iii.), this region is covered with striations, perpendicular to the direction of the crack propagation. The striations are evidence of the fracture mechanics responsible for crack propagation, suggesting the occurrence of local microplastic deformation [11]. This feature is important for understanding the crack growth rate since each striation corresponds to a single cycle, and the distance between these markings is correlated to the fracture's advancement through the material per cycle. The striation spacing is directly proportional to the fracture growth as well as the level of plastic deformation under the Paris' regime [20]. The region immediately prior to the overloaded area (ii.) exhibits unstable fracture growth characteristics, indicating that the fatigue life is approaching failure. This area is no longer smooth and flat, but rather uneven and prone to the development of microscopic secondary cracks.

The overload area is considered the specimen's sudden and final failure location. This section has a significantly different morphology and texture compared to the propagation region, and it is characterized by being covered by a population of microscopic voids and shallow dimples. These attributes indicate that the material exhibited a ductile behaviour prior to fracture and local ductile failure mechanism. However, the morphology, size, and density of dimples on the surface differ from weld material to base material, as does the presence of inclusions within each one.

Figure 46 not only depicts the overload area of specimens from different zones of the welded joint but also the EDS results from an assessment of the inclusions inside the dimples, which vary in morphology and nature.

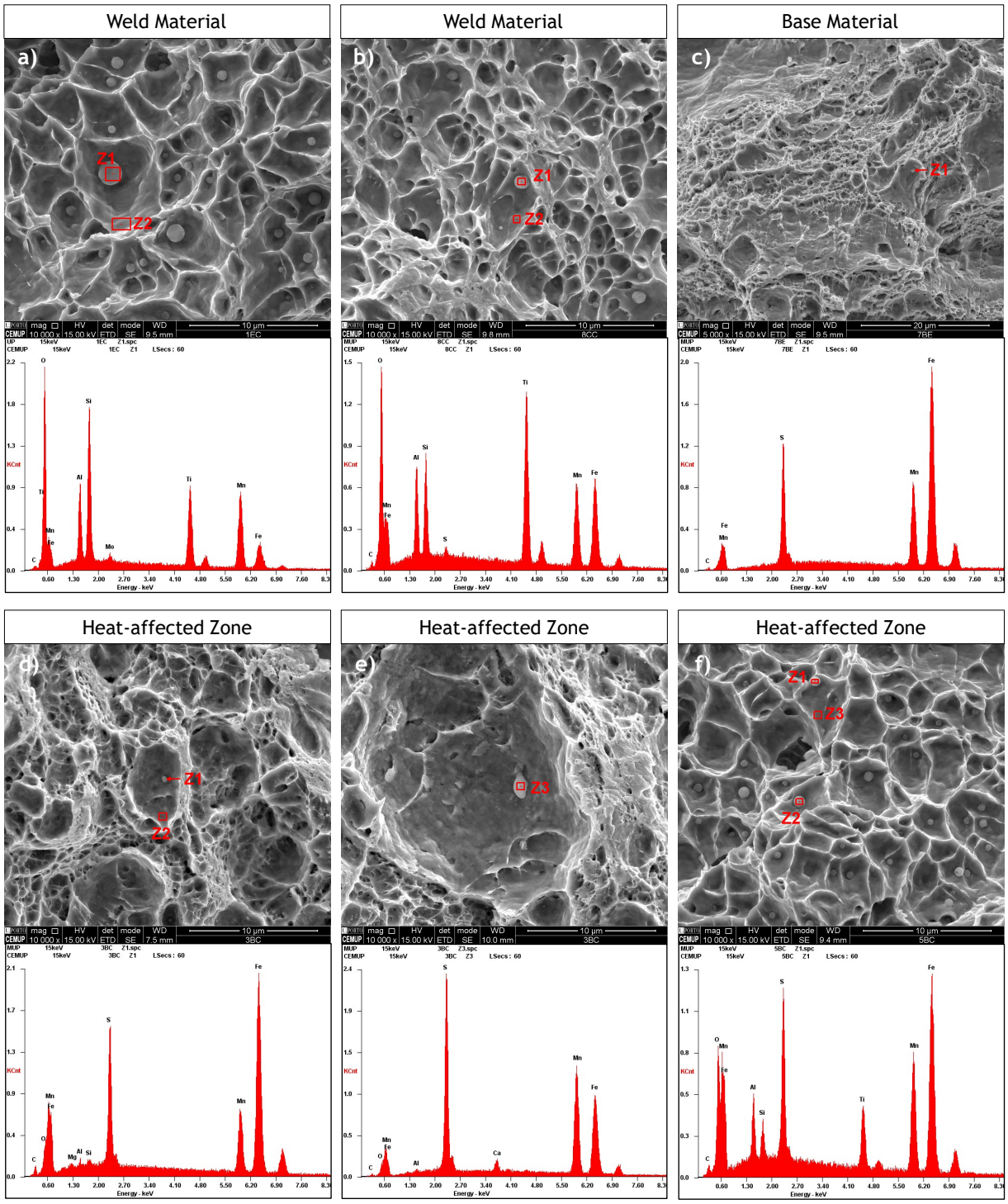


Figure 46: Dimples EDS analysis and corresponding inclusions' spectrum for a,b) weld material; c) base material; and d,e,f) heat-affected zone.

This research reveals that the nature and composition of the inclusions differ from zone to zone, suggesting that both chemical composition and the heat input influence their existence. The EDS spectrum can be used to qualitatively evaluate several zones that are representative of inclusions for better understanding. Table 7 represents the chemical composition (At %) of the inclusions' EDS zones.

Table 7: Chemical composition of the inclusions using EDS analysis.

		Chemical Composition (At. %)									
Region	Zone	O	Al	Si	Mo	Ti	Mn	S	Mg	Ca	Fe
WM	Zone 1 (a.)	52.39	6.33	11.53	0.40	9.17	15.00	-	-	-	5.18
	Zone 1 (b.)	45.71	5.93	5.48	-	14.44	12.46	0.54	-	-	15.43
HAZ	Zone 1 (d.)	3.23	0.57	0.66	-	-	17.17	14.17	0.79	-	63.41
	Zone 3 (e.)	0.40	0.13	-	-	-	41.06	11.41	-	1.15	45.86
	Zone 1 (f.)	18.82	4.87	2.41	-	5.93	19.08	10.31	-	-	38.58
	Zone 2 (f.)	40.09	10.82	4.35	-	10.05	9.73	0.41	-	-	24.54

The base material fracture surface is usually free of inclusions, with only a few small ones that were produced during the steel production process. The EDS spectrum of one of these inclusions (Figure 46.c.), shows that it is a manganese sulphide (MnS) inclusion. This type of inclusion is common in steels and can affect the mechanical properties of the material, especially if it is subjected to hot working processes such as rolling and forging. MnS inclusions are soft and deformable, so these processes can elongate and plastically deform them, leading to anisotropic microstructures and properties. In this case, the hot rolling process that was used to produce the plate is likely responsible for the elongated shape of the MnS inclusion.

The weld material fracture surface has a different appearance than the base material fracture surface. The weld material contains numerous more inclusions, which are spherical in shape. According to the EDS analysis, the inclusions are a result of intricate reactions during weld cooling and consist of non-metallic complex oxides of aluminum, titanium, silicon, and manganese. These inclusions formed during the weld cooling process when the welding metal was in the liquid state and oxidation mechanisms predominated. The reason why these specific elements (Al, Ti, Si, Mn) reacted with oxygen can be justified using the Ellingham diagram present in Appendix E. According to this diagram, these elements have a strong affinity for oxygen and are therefore more likely to form oxides.

The inclusions in the heat-affected zone fracture surface have a tendency to have a variety of compositions, shapes, and nature, depending on their distance from the fusion zone. For example, the samples in Figures 46.d and e. may have come from a region far from the fusion zone as the inclusions examined consist mainly of MnS, similar to those found in the base material, implying that this region got less thermal input. The fracture surface in Figure 46.f, on the other hand, may have been near the transition from the HAZ to the fusion zone, as it

contains complex oxides with compositions similar to those found in weld material specimens. This zone may have experienced extremely high temperatures during the welding procedure, allowing complex reactions between oxygen and the existing elements to occur due to the close proximity to the fusion zone.

Another finding of this study is that the size, morphology, and distribution of dimples over the fracture surface vary between the weld material and base material. This is illustrated in Figure 47, which shows samples fractured at a stress of 480 MPa. Compared to the base material dimples, which are smaller and more elongated, the weld material dimples are larger and more spherical. The difference in compositions and microstructures of the base material and the weld material are most likely the reason for this variation in dimple morphology.

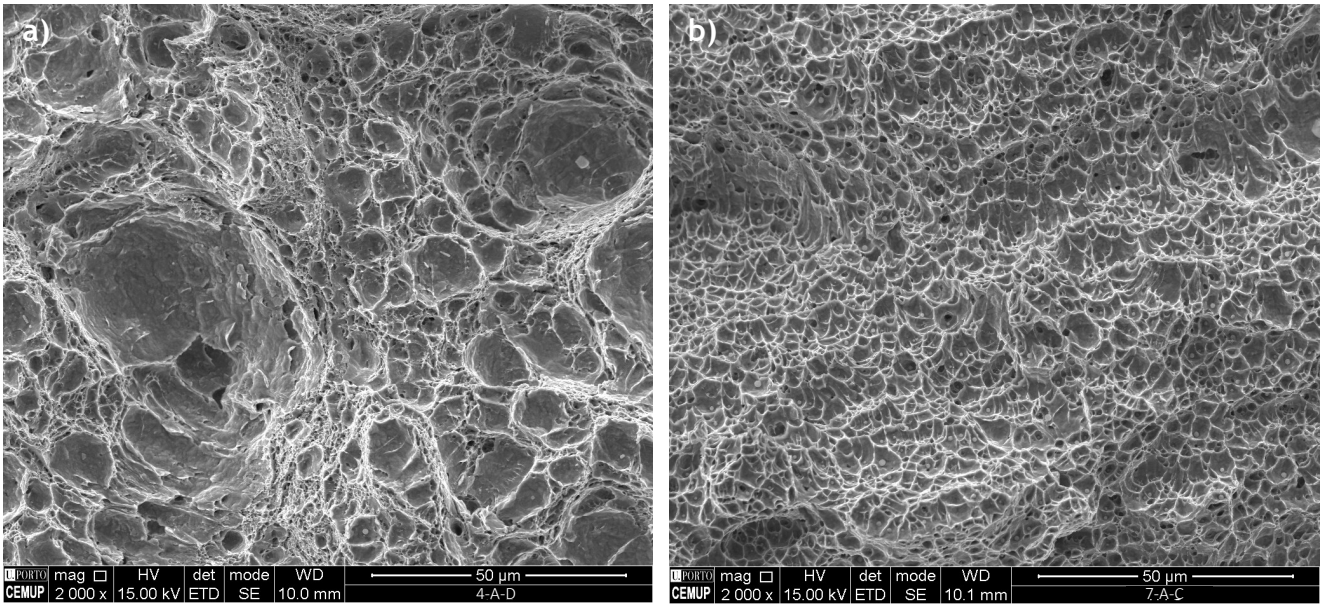


Figure 47: Dimples size and distribution in a) base material and b) weld material.

As referred before, the overload area of all fracture surfaces consists of dimples, indicating that a ductile fracture took place. However, for the base material, the overload area exhibits larger and deeper voids and dimples with a more heterogeneous size variation, while the weld material consists of more packed and smaller size dimples. This size difference can be justified by the cooling rates and thermal cycles that each region was submitted. The fusion zone described the faster cooling rate, transcribing in finer-grain size microstructures when compared to the base material that had slower cooling rates. Another factor is the hardness values of these distinct sections, where the WM registered the highest values. All of this leads to smaller and more packed dimples in the WM specimens, while the BM have deeper voids with irregular sizes.

5 Conclusions

The fatigue resistance of two S690QL welded joints with different thicknesses, M30 and M60, was characterized in this study. The microstructural, chemical composition, hardness, and fractographic analyses revealed several significant findings that correlated with the fatigue behaviour of the welded plates. The fatigue behaviour was evaluated in three different regions of the welded joints and the following conclusions can be drawn out:

- The HAZ is made up of several subzones with varying grain morphologies and sizes. The WM has columnar grains with a fine martensitic structure, while the BM is made up of tempered martensite and bainite. The HAZ near the fusion line corresponds to coarse-grained tempered martensite, while a fine-grained one appears farther to the melted zone. According to the CCT diagram and microhardness evaluation of this specific zone, the heat-affected subzone near the BM is constituted of tempered martensite-bainite with ferrite in grain boundaries.
- The macrohardness analyses showed that the last welding steps tend to reduce the root hardness values (affiliation B) through a tempering heat treatment that results from the thermal input of the last steps. For both M30 and M60 plates, affiliation B indicated a nearly straight-line behaviour throughout a fully welded operation, whereas in affiliation A, the HAZ and WM showed higher values than the BM, with the HAZ reaching the highest values. According to ISO 15614-1:2017, these procedures were suitable for industrial applications, since not a single hardness value exceeded the limit of 450 HV10.
- According to the fatigue data, all of the curves from both plates had a similar slope, with the exception of the base material from section C from M60, due to the lower ductility and toughness of this plate. The fatigue data showed that the WM specimens had the strongest fatigue resistance, followed by the BM specimens and the HAZ specimens. The HAZ presents a fatigue life below the BM due to the heterogeneous nature of this region. For the M30 plate, the results varied within the top and bottom sections, where the BM specimens' resistance, as well as the WM and HAZ specimens' resistance in that region, were higher. The M60 plate had a significantly lower fatigue resistance than the M30 plate, especially in the HAZ, reaching a variation of -2059% for HAZ in terms of number of cycles, for a stress range of 480-520 MPa.
- The fractographic study showed that the initiation, propagation, and final fracture stages of fatigue failure could be characterized. More nucleation sites typically develop and congregate in the overload region as the stress rises. An unstable crack growth near the overload area is identified by its unevenness and is more likely to form secondary cracks than a stable crack growth, which is characterized by a flat, smooth area covered with striations. The final fracture zone also has distinct morphologies as well as

diverse inclusions. The BM has wider and deeper voids with varying sizes of dimples, and small MnS inclusions form as a result of the plate manufacturing process. The WM has smaller and more packed dimple because of the fine-grained structure of this location. Every dimple, in this case, is associated with a non-metallic inclusion of complex oxide generated during the cooling of the fusion zone.

The results of this study provide valuable insights into the fatigue behaviour of S690QL welded joints. The findings suggest that the HAZ is the most critical region in terms of fatigue resistance, and that the fatigue life of the welded plate can be significantly improved by optimizing the welding procedures. To avoid the formation of brittle phases, which can reduce fatigue performance, preheating can be employed to slow down the cooling rate. Martensite is a hard and brittle phase that can occur when high-strength steel is heated to a high temperature and then rapidly cooled. Cold cracking can be reduced by making preheating necessary throughout the welding process.

6 Future Works

The results of this study provide valuable insights into the fatigue behaviour of S690QL welded plates. However, there are still some areas that could be further investigated.

- The effects of pre-heating and residual stresses: The effects of pre-heating and residual stresses from the welding process on the fatigue resistance of S690QL welded plates could be investigated to improve the technical method of these welded joints. A numerical study simulating this process could give valuable insights to understand these effects.
- Other welding procedures: The fatigue behaviour of S690QL welded plates produced with other welding procedures, such as SAW, FCAW-S, and FCAW-G, could be investigated to determine which technique is the best suited for this type of application.
- Corrosion-related fatigue studies: Corrosion-related fatigue studies would be necessary, considering that these structures are situated in hazard environments.

References

[1] LetsBuild, "Offshore construction: The main benefits and struggles." https://www.letsbuild.com/blog/offshore-construction-benefits-and-struggles, 2017. Accessed: 2023-06-21.

[2] M. Jimenez-Martinez, "Fatigue of offshore structures: A review of statistical fatigue damage assessment for stochastic loadings," *International Journal of Fatigue*, vol. 132, p. 105327, 2020.

[3] Martifer, "Grupo Martifer." https://www.martifer.com/en. Accessed: 2023-01-24.

[4] E. Cadoni and D. Forni, "Strain-rate effects on s690ql high strength steel under tensile loading," *Journal of Constructional Steel Research*, vol. 175, p. 106348, 2020.

[5] Z. Duan and X. Pei, "Effect of quenching processes on microstructure and mechanical properties of a high strength steel," in *IOP Conference Series: Materials Science and Engineering*, vol. 562, p. 012006, IOP Publishing, 2019.

[6] C. Maraveas, Z. C. Fasoulakis, and K. D. Tsavdaridis, "Mechanical properties of high and very high steel at elevated temperatures and after cooling down," *Fire Science Reviews*, vol. 6, 12 2017.

[7] P. Dirisu, S. Ganguly, A. Mehmanparast, F. Martina, and S. Williams, "Analysis of fracture toughness properties of wire + arc additive manufactured high strength low alloy structural steel components," *Materials Science and Engineering: A*, vol. 765, p. 138285, 2019.

[8] S. Kou, *Welding Metallurgy*. Nashville, TN: John Wiley & Sons, 2 ed., Oct. 2002.

[9] Q. Xin, "Durability and reliability in diesel engine system design," in *Diesel Engine System Design* (Q. Xin, ed.), pp. 113–202, Woodhead Publishing, 2013.

[10] L. Li, C.-Q. Li, and M. Mahmoodian, "Prediction of fatigue failure of steel beams subjected to simultaneous corrosion and cyclic loading," *Structures*, vol. 19, pp. 386–393, 2019.

[11] J. Schijve, *Fatigue of Structures and Materials*. New York, NY: Springer, 2 ed., Aug. 2008.

[12] H. Andersson, *Metal Fatigue Principles and Analyses A Compendium*. 2021.

[13] A. Nissan and K. Findley, "Microstructures and mechanical performance of induction-hardened medium-carbon steels," in *Comprehensive Materials Processing* (S. Hashmi, G. F. Batalha, C. J. Van Tyne, and B. Yilbas, eds.), pp. 581–604, Oxford: Elsevier, 2014.

[14] C. M. Branco, A. A. Fernandes, and P. M. T. d. Castro, *Fadiga de estruturas soldadas*. Fundação Calouste Gulbenkian, 1999.

[15] P. M. S. T. D. Castro, R. Manuel, C. Miranda, and M. A. V. D. Figueiredo, "Study of fatigue crack propagation master in mechanical engineering study of fatigue crack propagation in metallic structures," 2010.

[16] P. C. Paris and F. Erdogan, "A critical analysis of crack propagation laws," *Journal of Basic Engineering*, vol. 85, pp. 528–533, 1963.

[17] V. Doquet, G. Hénaff, T. Palin-Luc, and M. Risbet, "4 - fatigue crack initiation and propagation," in *Mechanics - Microstructure - Corrosion Coupling* (C. Blanc and I. Aubert, eds.), pp. 65–90, Elsevier, 2019.

[18] U. Zerbst, M. Madia, M. Vormwald, and H. Beier, "Fatigue strength and fracture mechanics – a general perspective," *Engineering Fracture Mechanics*, vol. 198, pp. 2–23, 2018. Fracture mechanics-based determination of the fatigue strength of weldments.

[19] G. E. Totten, "Fatigue crack propagation," *Advanced Materials & Processes*, vol. 166, pp. 39–41, 2008.

[20] C. propagationias and A. Pineau, eds., *Fatigue of materials and structures*. London, England: ISTE Ltd and John Wiley & Sons, June 2010.

[21] A. M. de Jesus, R. Matos, B. F. Fontoura, C. Rebelo, L. Simões da Silva, and M. Veljkovic, "A comparison of the fatigue behavior between s355 and s690 steel grades," *Journal of Constructional Steel Research*, vol. 79, pp. 140–150, 2012.

[22] O. Basquin, "The exponential law of endurance tests," in *Proc Am Soc Test Mater*, vol. 10, pp. 625–630, 1910.

[23] L. F. Coffin Jr, "A study of the effects of cyclic thermal stresses on a ductile metal," *Transactions of the American Society of Mechanical engineers*, vol. 76, no. 6, pp. 931–949, 1954.

[24] S. S. Manson, *Behavior of materials under conditions of thermal stress*, vol. 2933. National Advisory Committee for Aeronautics, 1953.

[25] J. Morrow, "Cyclic plastic strain energy and fatigue of metals," in *Internal friction, damping, and cyclic plasticity*, pp. 45–87, ASTM International, 1965.

[26] A. Srivastava and A. Sharma, "Advances in joining and welding technologies for automotive and electronic applications," *American Journal of Materials Engineering and Technology*, vol. 5, 08 2017.

[27] Y. Ma, S. Zhang, T. Wang, Y. He, W. Chen, L. Liu, and F. Liu, "Atomic diffusion behavior near the bond interface during the explosive welding process based on molecular dynamics simulations," *Materials Today Communications*, vol. 31, 2022.

[28] K. Weman, "Arc welding: an overview," in *Welding Processes Handbook (Second Edition)* (K. Weman, ed.), Woodhead Publishing Series in Welding and Other Joining Technologies, pp. 31–50, Woodhead Publishing, second edition ed., 2012.

[29] H. Liu and Y. Hu, "Welding," in *Encyclopedia of Materials: Metals and Alloys* (F. G. Caballero, ed.), pp. 39–65, Oxford: Elsevier, 2022.

[30] M. Saini, "Gas metal arc welding working principle advantages and applications," 2022.

[31] O. Aderinola, P. Kah, and J. Martikainen, "Efficient welding technologies applicable to hss arctic offshore structures," 06 2014.

[32] J. Grill, "What is gmaw (mig welding) & how does it work? - weld guru," 2022.

[33] S. Lathabai, "20 - joining of aluminium and its alloys," in *Fundamentals of Aluminium Metallurgy* (R. Lumley, ed.), Woodhead Publishing Series in Metals and Surface Engineering, pp. 607–654, Woodhead Publishing, 2011.

[34] M. Weglowski, H. Y, and Z. Y.M, "Effect of welding current on metal transfer in gmaw," *Archives of Materials Science and Engineering*, vol. 33, 09 2008.

[35] R. Singh, "3 - welding and joining processes," in *Applied Welding Engineering (Third Edition)* (R. Singh, ed.), pp. 157–186, Butterworth-Heinemann, third edition ed., 2020.

[36] J. Nadzam, "Gas metal arc welding product and procedure selection."

[37] D. S. Naidu, S. Ozcelik, and K. L. Moore, "Chapter 2 - gas metal arc welding: Modeling," in *Modeling, Sensing and Control of Gas Metal Arc Welding* (D. S. Naidu, S. Ozcelik, and K. L. Moore, eds.), pp. 9–93, Oxford: Elsevier Science Ltd, 2003.

[38] M. Wahab, "6.03 - manual metal arc welding and gas metal arc welding," in *Comprehensive Materials Processing* (S. Hashmi, G. F. Batalha, C. J. Van Tyne, and B. Yilbas, eds.), pp. 49–76, Oxford: Elsevier, 2014.

[39] R. Singh, "3 - welding and joining processes," in *Applied Welding Engineering (Third Edition)* (R. Singh, ed.), pp. 157–186, Butterworth-Heinemann, third edition ed., 2020.

[40] Dinbandhua, V. Prajapati, J. J. Vora, and K. Abhishek, *Advances in gas metal arc welding process: Modifications in short-circuiting transfer mode*. 2021. Cited by: 4.

[41] R. Singh, "6 - stresses, shrinkage, and distortion in weldments," in *Applied Welding Engineering (Third Edition)* (R. Singh, ed.), pp. 207–249, Butterworth-Heinemann, third edition ed., 2020.

[42] N. Bailey, "Introduction," in *Weldability of Ferritic Steels* (N. Bailey, ed.), Woodhead Publishing Series in Welding and Other Joining Technologies, pp. viii–x, Woodhead Publishing, 1994.

[43] "Reference number iso/tr 581:2005(e) iso/tr 581 first edition weldability-metallic materials-general principles," 2005.

[44] Fabricating and Metalworking, "Welding high strength steels." https://www.fabricatingandmetalworking.com/2008/06/welding-high-strength-steels/. Accessed: 2023-04-13.

[45] K. Weman, *Welding processes handbook*. Woodhead Publishing Series in Welding and Other Joining Technologies, Cambridge, England: Woodhead Publishing, 2 ed., 2011.

[46] "Hot rolled products of structural steels - Part 6: Technical delivery conditions for flat products of high yield strength structural steels in the quenched and tempered condition," standard, British Standards Institution, United Kingdom, Aug. 2019.

[47] "S690ql High Yield Structural Steel - Properties and Applications." https://www.azom.com/article.aspx?ArticleID=5266, jun 1 2010.

[48] "Specification and qualification of welding procedures for metallic materials — welding procedure specification — part 1: Arc welding," standard, International Organization for Standardization, Switzerland, Aug. 2019.

[49] "Welding consumables - Tubular cored electrodes for gasshielded and non-gas-shielded metal arc welding of high strength steels - Classification," standard, International Organization for Standardization, Switzerland, Apr. 2017.

[50] ESAB, "Coreweld 69 lt h4." https://esab.com/ba/eur_en/products-solutions/filler-metals-pdf/?filename=mdm-productfamily-39324&siteid=eur_en&countryname=SEE&countrylocale=en-zz.

[51] "Welding consumables — Gases and gas mixtures for fusion welding and allied processes," standard, International Organization for Standardization, Switzerland, Oct. 2008.

[52] "Metallic materials — Rotating bar bending fatigue testing," standard, British Standards Institution, United Kingdom, July 2010.

[53] "Metallic materials — fatigue testing — statistical planning and analysis of data," standard, British Standards Institution, United Kingdom, Mar. 2003.

[54] C. Stromeyer, "The determination of fatigue limits under alternating stress conditions," *Proceedings of the Royal Society of London. Series A, Containing Papers of a Mathematical and Physical Character*, vol. 90, no. 513, pp. 411–425, 1914.

[55] J. Kohout and S. Vechet, "A new function for fatigue curves characterization and its multiple merits," *International Journal of Fatigue*, vol. 23, no. 2, pp. 175–183, 2001.

[56] "Destructive tests on welds in metallic materials - hardness testing - part 1: Hardness test on arc welded joints," standard, International Organization for Standardization, Switzerland, Mar. 2011.

[57] "Destructive tests on welds in metallic materials - hardness testing - part 2: Microhardness testing of welded joints," standard, International Organization for Standardization, Switzerland, Mar. 2011.

[58] S. Lars-Erik, *Control of Microstructures and Properties in Steel Arc Welds*. CRC Press, Sept. 2017.

[59] P. Seyffarth, R. Schmidt, and U. Jasnau, "Simulation of microstructure-transformation-kinetics of unalloyed constructional steel in case of fast thermal cycles," in *Proceedings of the 3rd LANE - Laser Assisted Net shape Engineering*, 2001.

[60] S. Błacha, M. Weglowski, S. Dymek, and M. Kopyscianski, "Microstructural characterization and mechanical properties of electron beam welded joint of high strength steel grade s690ql," *Archives of Metallurgy and Materials*, vol. 61, pp. 1193–1200, 07 2016.

[61] J. I. Goldstein, D. E. Newbury, J. R. Michael, N. Ritchie, J. H. J. Scott, and D. C. Joy, *Scanning electron microscopy and X-ray microanalysis*. New York, NY: Springer, 4 ed., Nov. 2017.

[62] Yena Engineering, "Effect of Alloying Elements on Steel." Website, Accessed 2023-05-22. [Online]. Available: https://yenaengineering.nl/effect-of-alloying-elements-on-steel/.

[63] M. Hugenschmidt, K. Adrion, A. Marx, E. Müller, and D. Gerthsen, "Quantification and Mitigation of Electron-Beam-Induced Carbon Contamination," *Microscopy and Microanalysis*, vol. 27, pp. 2022–2024, 08 2021.

[64] A. J. V. Griffiths and T. Walther, "Quantification of carbon contamination under electron beam irradiation in a scanning transmission electron microscope and its suppression by plasma cleaning," *Journal of Physics: Conference Series*, vol. 241, p. 012017, jul 2010.

[65] "Welding — guidelines for a metallic materials grouping system," standard, International Organization for Standardization, Switzerland, Feb. 2017.

[66] "Specification and qualification of welding procedures for metallic materials — welding procedure test — part 1: Arc and gas welding of steels and arc welding of nickel and nickel alloys," standard, International Organization for Standardization, Switzerland, June 2017.

[67] D. M. Ferreira, A. d. Silva Alves, R. Cruz Neto, T. Ferreira Martins, and S. D. Brandi, "A new approach to simulate hsla steel multipass welding through distributed point heat sources model," *Metals - Open Access Metallurgy Journal*, vol. 8, p. 18, 11 2018.

[68] H. Bhadeshia and R. Honeycombe, *Steels: Microstructure and properties*. Oxford, England: Butterworth-Heinemann, Jan. 2017.

[69] H.-F. Li, X.-P. Wang, Y.-M. Liu, Y.-Q. Liu, P.-F. Liu, and S.-P. Yang, "Crack growth path of high-strength steel with different toughness under monotonic and cyclic loadings," *International Journal of Fatigue*, vol. 169, p. 107503, 2023.

[70] B. Guennec, A. Ueno, T. Sakai, M. Takanashi, and Y. Itabashi, "Effect of the loading frequency on fatigue properties of jis s15c low carbon steel and some discussions based on micro-plasticity behavior," *International Journal of Fatigue*, vol. 66, pp. 29–38, 2014.

[71] Wikiwand, "Ellingham diagram - thermodynamic principle of metallurgy," 2023. Accessed on June 19, 2023.

Appendixes

A M30 Technical Plan

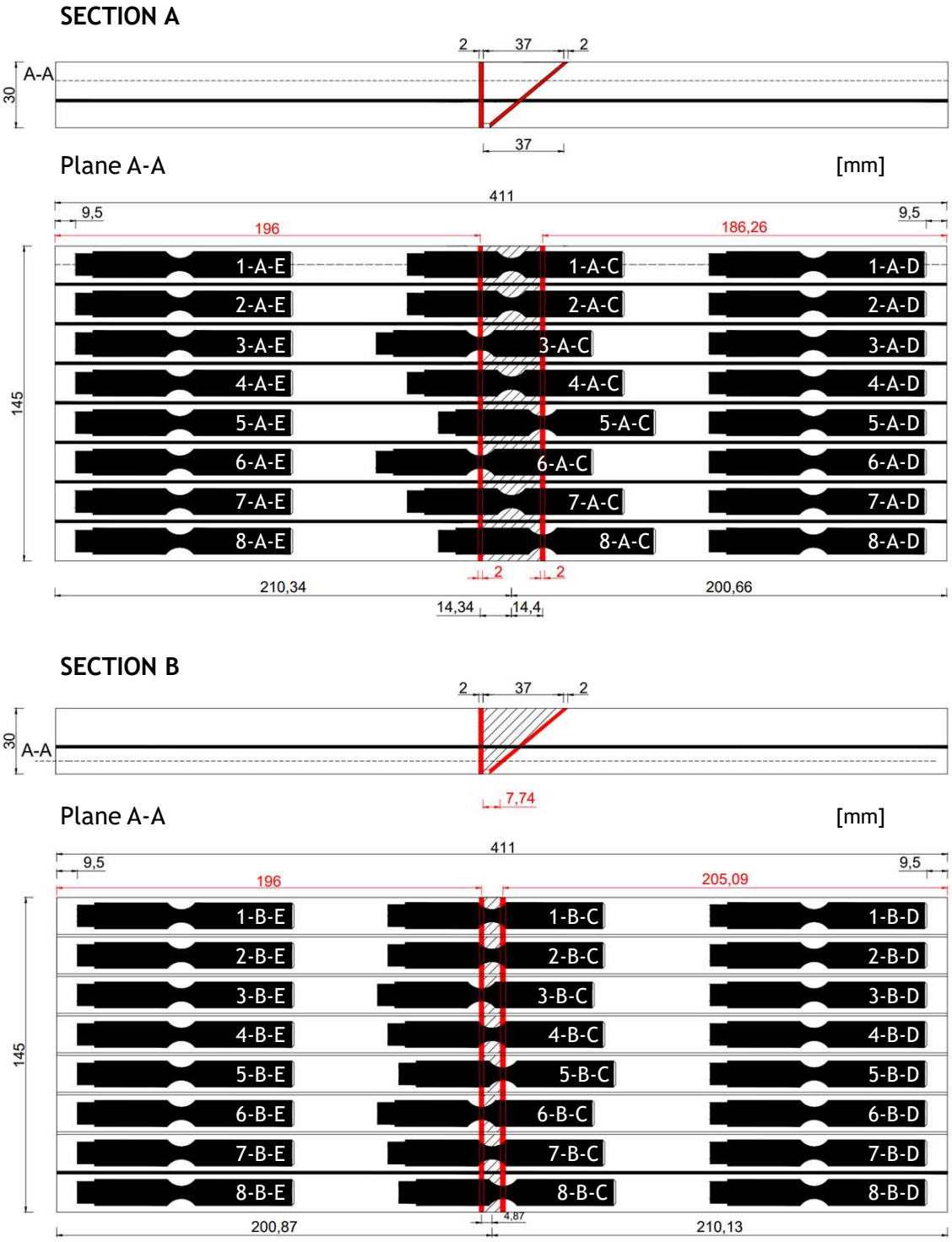


Figure 48: Technical plan of Section A and B for the 30 mm thickness plate.

B M60 Technical Plan

B.1 M60 Technical Plan - Section C

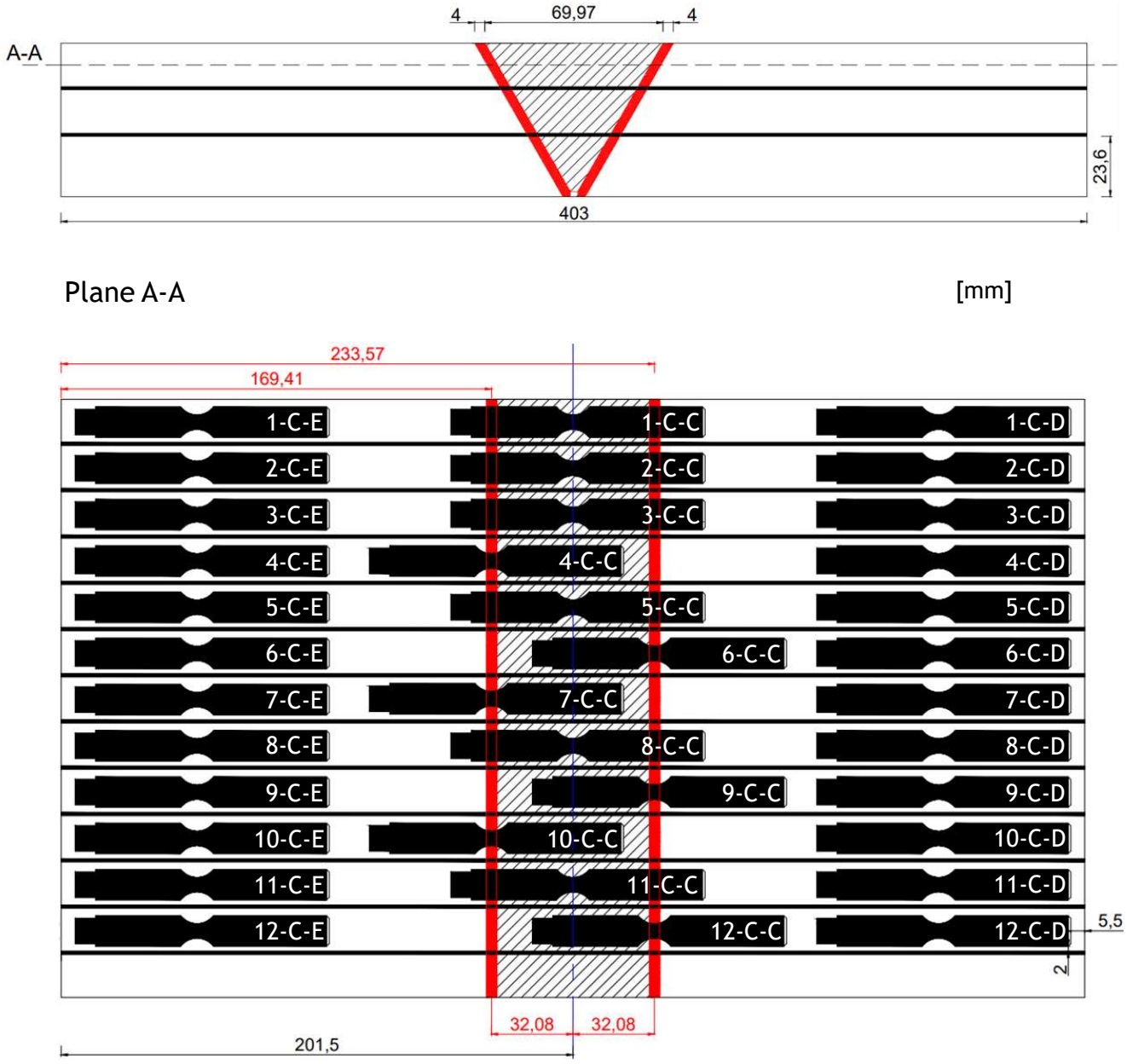
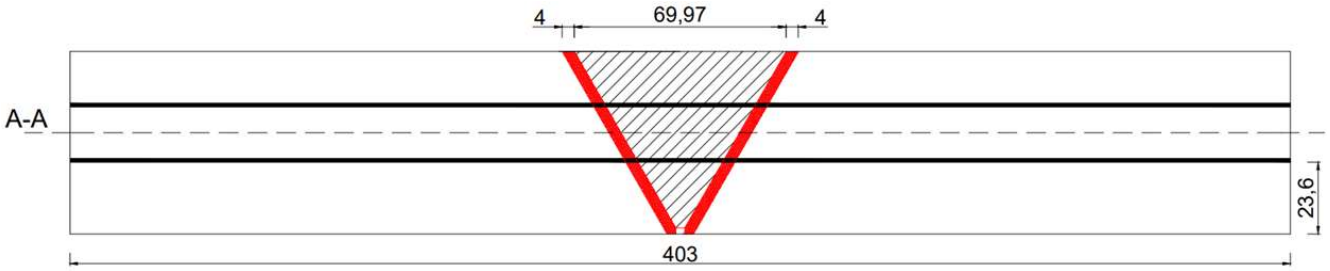


Figure 49: Technical plan of Section C for the 60 mm thickness plate.

B.2 M60 Technical Plan - Section D

SECTION D



Plane A-A [mm]

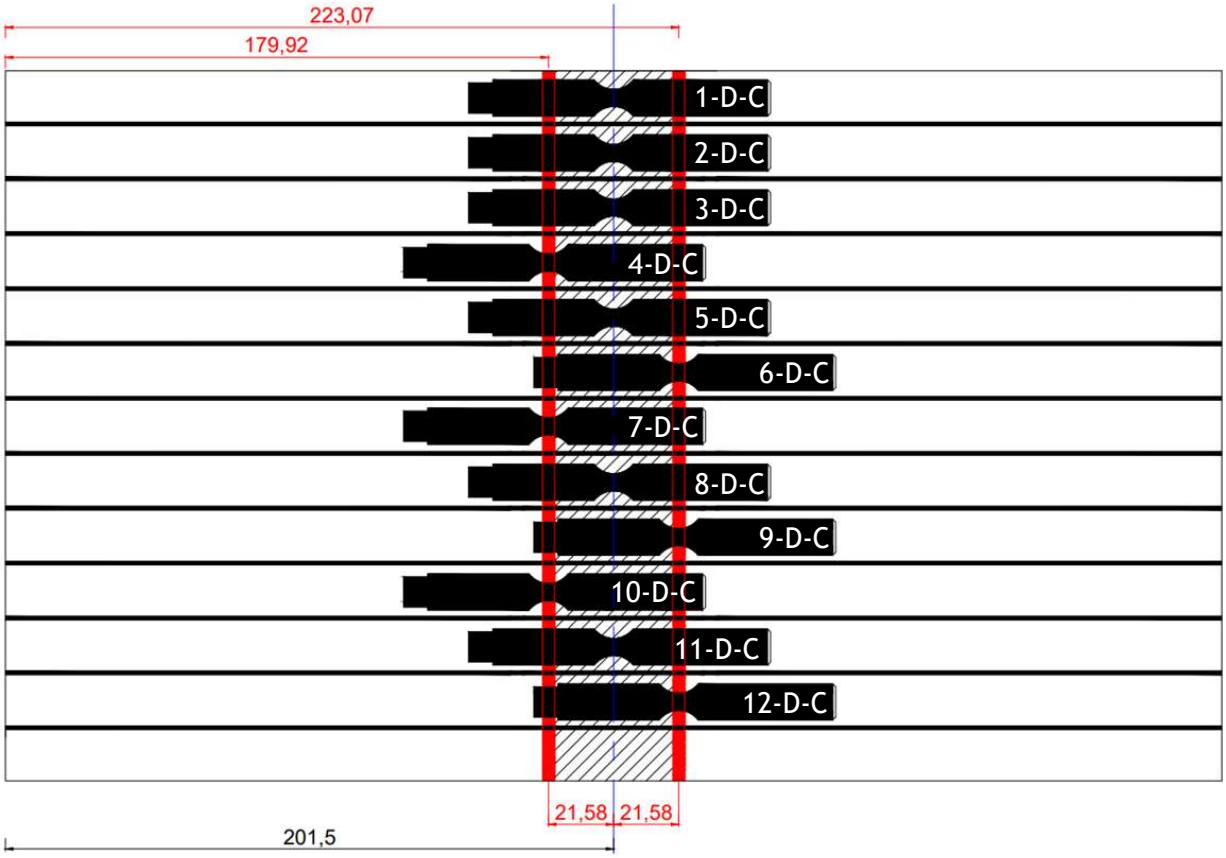


Figure 50: Technical plan of Section D for the 60 mm thickness plate.

B.3 M60 Technical Plan - Section E

SECTION E

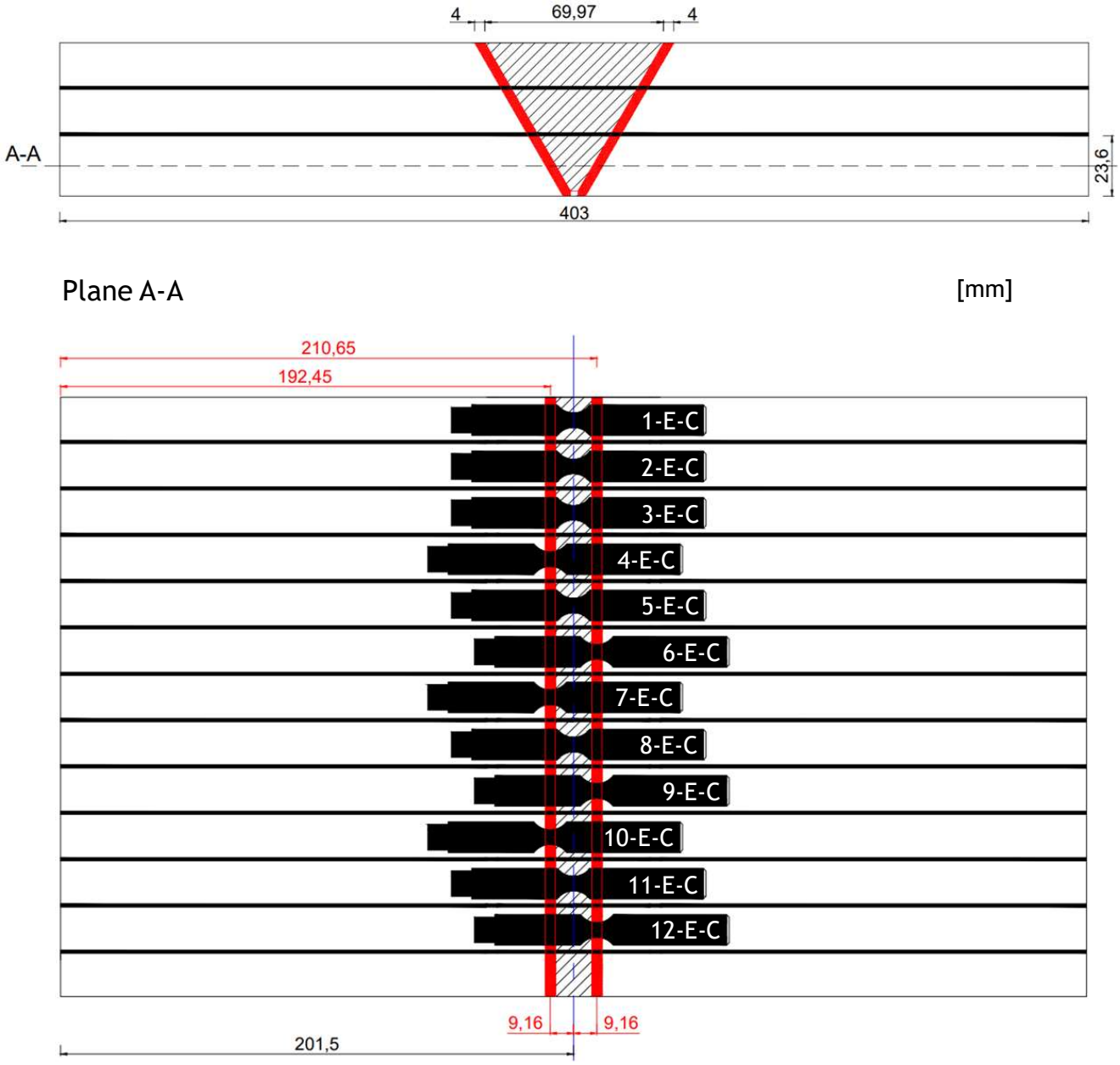


Figure 51: Technical plan of Section E for the 60 mm thickness plate.

C Rotating bending fatigue results for M30 plate

C.1 M30 - Section A fatigue results

Table 8: Rotating bending fatigue results for M30 section A.

Section	Region	Specimen	Stress amplitude, σ_a [MPa]	Number of cycles, N
A	Base material (BM)	1-A-E	535	98990
A	Base material (BM)	2-A-E	524	206290
A	Base material (BM)	3-A-E	540	141050
A	Base material (BM)	4-A-E	520	137600
A	Base material (BM)	5-A-E	520	509290
A	Base material (BM)	6-A-E	520	319960
A	Base material (BM)	7-A-E	600	57600
A	Base material (BM)	8-A-E	600	33200
A	Base material (BM)	1-A-D	600	57450
A	Base material (BM)	2-A-D	480	656680
A	Base material (BM)	3-A-D	480	1314880
A	Base material (BM)	4-A-D	480	333370
A	Base material (BM)	5-A-D	440	10000000 (RO)
A	Base material (BM)	6-A-D	440	10000000 (RO)
A	Base material (BM)	7-A-D	440	10000000 (RO)
A	Base material (BM)	8-A-D	540	124260
A	Weld Material (WM)	1-A-C	480	10000000 (RO)
			520*	288240
A	Weld Material (WM)	2-A-C	480	10000000 (RO)
			520*	3276360
A	Weld Material (WM)	4-A-C	480	10000000 (RO)
			520*	90990
A	Weld Material (WM)	7-A-C	480	1779490
A	Heat-affected zone (HAZ)	3-A-C	480	10000000 (RO)
			520*	1521850
A	Heat-affected zone (HAZ)	5-A-C	480	1233340
A	Heat-affected zone (HAZ)	6-A-C	480	10000000 (RO)
			520*	10000000 (RO)
A	Heat-affected zone (HAZ)	8-A-C	480	749270

C.2 M30 - Section B fatigue results

Table 9: Rotating bending fatigue results for M30 section B.

Section	Region	Specimen	Stress amplitude, σ_a [MPa]	Number of cycles, N
B	Base material (BM)	1-B-E	520	113250
B	Base material (BM)	2-B-E	520	24910
B	Base material (BM)	3-B-E	520	129310
B	Base material (BM)	4-B-E	520	177180
B	Base material (BM)	5-B-E	480	385790
B	Base material (BM)	6-B-E	480	10000000 (RO)
B	Base material (BM)	7-B-E	480	932900
B	Base material (BM)	8-B-E	600	43890
B	Base material (BM)	1-B-D	600	23610
B	Base material (BM)	2-B-D	600	32960
B	Base material (BM)	3-B-D	460	10000000 (RO)
B	Base material (BM)	4-B-D	460	1219620
B	Base material (BM)	5-B-D	460	101186
B	Base material (BM)	6-B-D	440	10000000 (RO)
B	Base material (BM)	7-B-D	440	10000000 (RO)
B	Base material (BM)	8-B-D	440	10000000 (RO)
B	Weld Material (WM)	1-B-C	520	184240
B	Weld Material (WM)	2-B-C	520	99820
B	Weld Material (WM)	4-B-C	520	35820
B	Weld Material (WM)	7-B-C	520	42130
B	Heat-affected zone (HAZ)	3-B-C	520	204230
B	Heat-affected zone (HAZ)	5-B-C	520	85550
B	Heat-affected zone (HAZ)	6-B-C	520	22160
B	Heat-affected zone (HAZ)	8-B-C	520	55940

D Rotating bending fatigue results for M60 plate

D.1 M60 - Section C fatigue results

Table 10: Rotating bending fatigue results for M60 section C.

Section	Region	Specimen	Stress amplitude, σ_a [MPa]	Number of cycles, N
C	Base material (BM)	1-C-E	520	115120
C	Base material (BM)	2-C-E	520	184470
C	Base material (BM)	3-C-E	520	141950
C	Base material (BM)	4-C-E	500	291660
C	Base material (BM)	5-C-E	520	114330
C	Base material (BM)	6-C-E	500	94100
C	Base material (BM)	7-C-E	440	10000000 (RO)
C	Base material (BM)	8-C-E	460	417690
C	Base material (BM)	9-C-E	440	10000000 (RO)
C	Base material (BM)	10-C-E	440	1345370
C	Base material (BM)	11-C-E	460	311700
C	Base material (BM)	12-C-E	440	367940
C	Base material (BM)	1-C-D	600	42360
C	Base material (BM)	2-C-D	520	130990
C	Base material (BM)	3-C-D	600	50040
C	Base material (BM)	4-C-D	540	93450
C	Base material (BM)	5-C-D	600	53850
C	Base material (BM)	6-C-D	540	152710
C	Base material (BM)	7-C-D	540	128320
C	Base material (BM)	8-C-D	480	400780
C	Base material (BM)	9-C-D	460	359460
C	Base material (BM)	10-C-D	480	228050
C	Base material (BM)	11-C-D	480	268130
C	Base material (BM)	12-C-D	500	201620
C	Weld Material (WM)	1-C-C	480	370250
C	Weld Material (WM)	2-C-C	600	39420
C	Weld Material (WM)	3-C-C	480	637840
C	Heat-affected zone (HAZ)	4-C-C	600	20430
C	Weld Material (WM)	5-C-C	600	52680
C	Heat-affected zone (HAZ)	6-C-C	600	143280
C	Heat-affected zone (HAZ)	7-C-C	480	78560
C	Weld Material (WM)	8-C-C	480	684690
C	Heat-affected zone (HAZ)	9-C-C	480	398560
C	Heat-affected zone (HAZ)	10-C-C	480	154780
C	Weld Material (WM)	11-C-C	600	67800
C	Heat-affected zone (HAZ)	12-C-C	520	143620

D.2 M60 - Section D fatigue results

Table 11: Rotating bending fatigue results for M60 section D.

Section	Region	Specimen	Stress amplitude, σ_a [MPa]	Number of cycles, N
D	Weld Material (WM)	1-D-C	478	10000000 (RO)
D	Weld Material (WM)	2-D-C	478	347650
D	Weld Material (WM)	3-D-C	478	1976650
D	Heat-affected zone (HAZ)	4-D-C	520	74830
D	Weld Material (WM)	5-D-C	496	562650
D	Heat-affected zone (HAZ)	6-D-C	520	243550
D	Heat-affected zone (HAZ)	7-D-C	440	1066300
D	Weld Material (WM)	8-D-C	496	287710
D	Heat-affected zone (HAZ)	9-D-C	440	568050
D	Heat-affected zone (HAZ)	10-D-C	420	276480
D	Weld Material (WM)	11-D-C	496	464840
D	Heat-affected zone (HAZ)	12-D-C	440	10000000 (RO)

D.3 M60 - Section E fatigue results

Table 12: Rotating bending fatigue results for M60 section E.

Section	Region	Specimen	Stress amplitude, σ_a [MPa]	Number of cycles, N
E	Weld Material (WM)	1-E-C	540	153680
E	Weld Material (WM)	2-E-C	540	145220
E	Weld Material (WM)	3-E-C	540	99120
E	Heat-affected zone (HAZ)	4-E-C	420	473750
E	Weld Material (WM)	5-E-C	440	10000000 (RO)
E	Heat-affected zone (HAZ)	6-E-C	520	92970
E	Heat-affected zone (HAZ)	7-E-C	520	67800
E	Weld Material (WM)	8-E-C	440	10000000 (RO)
E	Heat-affected zone (HAZ)	9-E-C	520	75890
E	Heat-affected zone (HAZ)	10-E-C	600	19680
E	Weld Material (WM)	11-E-C	460	10000000 (RO)
E	Heat-affected zone (HAZ)	12-E-C	420	10000000 (RO)

E Compounds' Stability - Ellingham Diagram

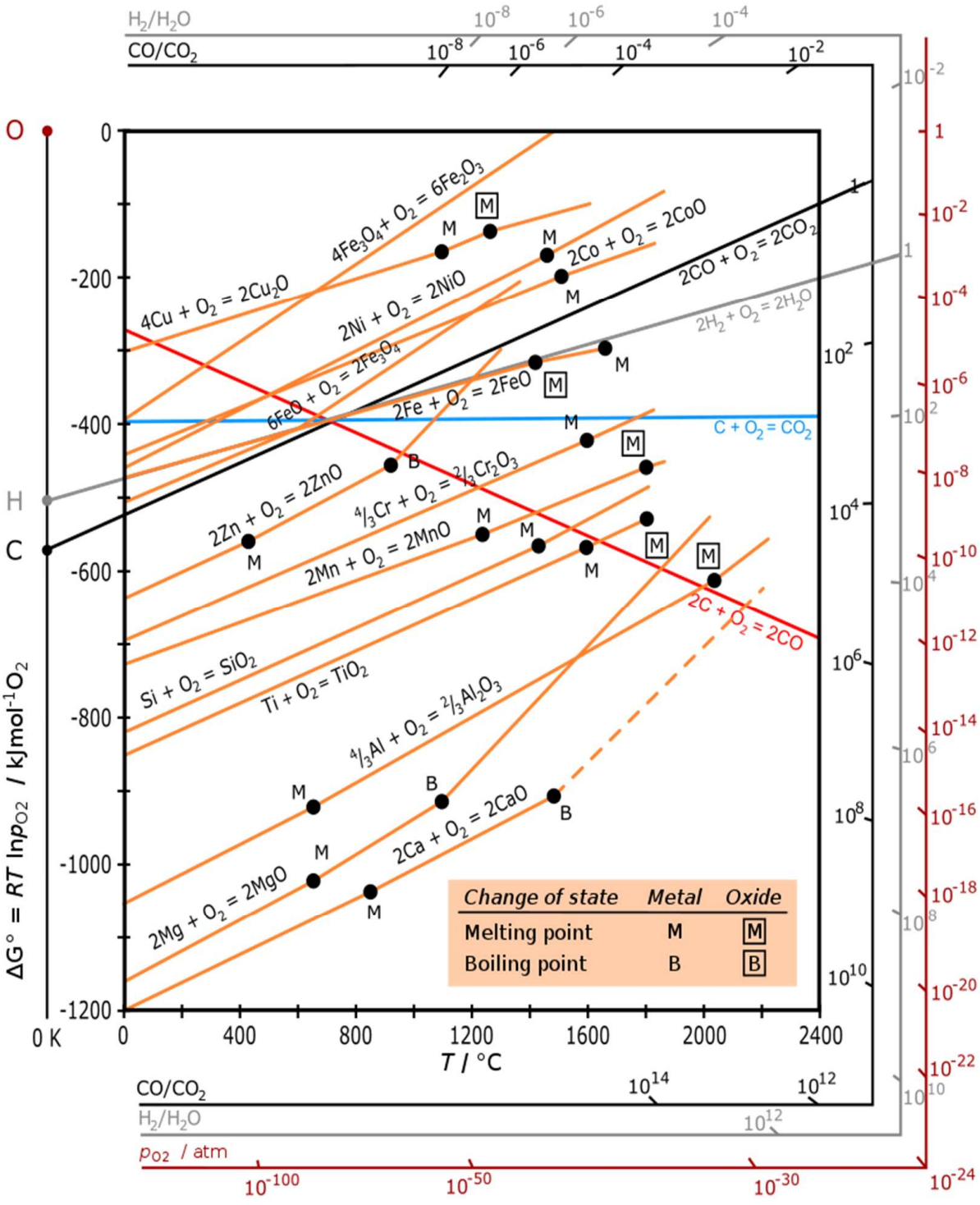


Figure 52: Compounds' stability according to the Ellingham Diagram, adapted from [71].